Crystal Plasticity Based Modelling of Surface Roughness and Localized Deformation During Bending in Aluminum Polycrystals

by

Jonathan Rossiter

A thesis

presented to the University of Waterloo

in fulfillment of the

thesis requirement for the degree of

Doctor of Philosophy

in

Mechanical Engineering

Waterloo, Ontario, Canada, 2015

Author's Declaration

I hereby declare that I am the sole author of this thesis. This is a true copy of the thesis, including any required final revisions, as accepted by my examiners.

I understand that my thesis may be made electronically available to the public.

Abstract

This research focuses on numerical modeling of formability and instabilities in aluminum with a focus on the bending loading condition. A three-dimensional (3D) finite element analysis based on rate-dependent crystal plasticity theory has been employed to investigate non-uniform deformation in aluminum alloys during bending. The model can incorporate electron backscatter diffraction (EBSD) maps into finite element analyses. The numerical analysis not only accounts for crystallographic texture (and its evolution) but also accounts for 3D grain morphologies, because a 3D microstructure (constructed from two-dimensional EBSD data) can be employed in the simulations. The first part of the research concentrates on the effect of individual aluminum grain orientations on the developed surface roughness during bending. The standard orientations found within aluminum are combined in a systematic way to investigate their interactions and sensitivity to loading direction. The end objective of the study is to identify orientations that promote more pronounced surface roughness so that future material processes can be developed to reduce the occurrence of these orientations and improve the bending response of the material. It was identified that Goss and Brass textures have the largest negative impact on bendability of the aluminum, with Goss being the most dependent on loading direction and Brass being detrimental in all loading directions. The second part of the research focuses on the representation of grain boundaries within the models. A new modeling approach of adding 20 μm wide grain boundary zones in conjunction with using single crystal material properties was developed and validated. Large columnar grain samples of aluminum were produced at McMaster University and analysed with Electron Back Scatter Diffraction to identify the grain structure prior to destructive testing. In-situ Digital Image Correlation strain measurements were

taken during a mechanical strength test. The combination of initial microstructure information as well as in-situ strain distributions allowed for a study analysing the effect of adding grain boundary zones into the models. The results showed that the error in predicted strain distribution could be reduced by 60% by the addition of hard grain boundary zones. During bending simulations using the grain boundary zone modelling approach, it was found that the network of hard grain boundary zones worked to distribute the applied bending load over more of the sample as opposed to the historic approach of representing grain boundaries as neighbouring regions with different orientations. The addition of grain boundary zones into the models can improve the accuracy of future studies.

Acknowledgements

This work was supported by the Natural Sciences and Engineering Research Council of Canada (NSERC) as well as the Ontario Graduate Scholorship (OGS). I also gratefully acknowledge the high performance computing center at the University of Sherbrooke, and Dr. HuiZhong Lu the Reseau Quebecois de Calcul de Haute Performance (RQCHP) for his technical support. I would also like to acknowledge the help of Dr. Abhijit Brahme for his help teaching me how to properly analyse microscture orientation data and Dr. Jidong Kang for providing the raw data required to process the large grained aluminum data. Finally I would like to thank my supervisor Prof. Kaan Inal for his constant help throughout the entire process.

Table of Contents

List of Figures

List of Tables

Nomenclature

α Index representing slip system α

β Index representing slip system β

$\dot{\gamma}_{(\alpha)}$ Rate of shear on slip system α

$\tau_{(\alpha)}$ Resolved shear stress on slip system α

$\tau_{y(\alpha)}$ Yield stress on slip system α

$\dot{\tau}_{(\alpha)}$ Rate of resolved shear stress on slip system α

$h_{\alpha\beta}$ Elements of flow stress on system α due to an increment of shear on system β

Φ_1 First Bunge angle for orientation specification

Φ Second Bunge angle for orientation specification

Φ_2 Third Bunge angle for orientation specification

$\boldsymbol{m}$ Slip plane normal

$\boldsymbol{s}$ Slip vectors

$\boldsymbol{F}$ Deformation gradient tensor

$\boldsymbol{F}^*$ Elastic portion of the deformation gradient

$\boldsymbol{F}^p$ Plastic portion of the deformation gradient

$\boldsymbol{L}$ Velocity gradient tensor

$\dot{\boldsymbol{F}}$ Rate of deformation gradient

$\boldsymbol{L}^{*}$ Elastic portion of the velocity gradient

$\boldsymbol{L}^{p}$ Plastic portion of the velocity gradient

$\boldsymbol{D}$ Strain rate tensor

$\boldsymbol{D}^{*}$ Elastic portion of strain rate

$\boldsymbol{D}^{p}$ Plastic portion of strain rate

$\boldsymbol{W}$ Spin tensor

$\boldsymbol{W}^{p}$ Plastic portion of spin

$\boldsymbol{W}^{*}$ Elastic portion of spin

$\boldsymbol{s}^{*}_{(\alpha)}$ Elastically distorted slip vector α

$\boldsymbol{m}^{*}_{(\alpha)}$ Elastically distorted slip plane normal α

$\boldsymbol{P}_{(\alpha)}$ Symmetric tensor of the elastically distorted slip system α

$\boldsymbol{W}_{(\alpha)}$ Skew-symmetric tensor of the elastically distorted slip system α

$\boldsymbol{\tau}$ Kirchhoff stress tensor

$\overset{\nabla}{\boldsymbol{\tau}}^{*}$ Jaumann rate of Kirchhoff stress

$\mathbf{L}$ Tensor of the elastic moduli

$\boldsymbol{\sigma}$ Cauchy stress tensor

$\overset{\nabla}{\boldsymbol{\sigma}}$ Jaumann rate of Cauchy stress

$\dot{\boldsymbol{\sigma}}^{0}$ Viscoplastic type stress-rate

$\boldsymbol{R}_{(\alpha)}$ Tensor representing (when combined with rate of shear) each slip system's component of viscoplastic type stress-rate

$\dot{\gamma}_{(0)}$ Reference shear rate

$\boldsymbol{g}_{(\alpha)}$ Hardness of slip system α

m strain rate sensitivity index

$\dot{\boldsymbol{g}}_{(\alpha)}$ Rate of hardness of slip system α

$\boldsymbol{h}_{(\beta)}$ Single slip hardening rate on system β

$\boldsymbol{q}_{(\alpha\beta)}$ Latent hardening matrix on system α due to hardening on system β

$\boldsymbol{A}$ 3 x 3 unity matrix

n Hardening exponent

$\boldsymbol{h}_{0}$ Hardening constant

$\boldsymbol{\tau}_0$ Critical resolved shear stress

$\boldsymbol{\gamma}_a$ Accumulated slip on all slip systems

$\boldsymbol{Q}$ Orientation matrix

h_s Asymptotic hardening rate

τ_s Saturation value of the shear stress

1. Introduction

With an estimated 260 million cars (US Bureau of Transportation Statistics [2014]) on the road today and roughly 18 million new vehicles purchased in 2013 in North America alone, the automotive industry is one of the largest industries in the world. It is a competitive industry that requires continuous product development in order for the individual companies to survive. The needs and desires of the consumers as well as governmental regulations dictate the goals of these product developments, which include, among other things, light weight, crash worthiness, and low-cost manufacturing. One approach the auto industry has taken to move towards these goals is improvement through material research. By identifying more corrosion resistant, light-weight, and formable materials, cars can be built more economically and lighter, and can last longer. Aluminum has proven to be a very attractive material for these purposes: It is far more corrosion resistant than steel, and it has a much higher strength to weight ratio. The drawback to aluminum is its formability; the formability of aluminum is inferior to that of steel, but is higher than that of magnesium, which is another light metal under consideration in the auto industry.

Material research does not end simply with material alloy selection but also includes aspects of the manufacturing process. Material processing to achieve a desired microstructure, such as work hardening, and tailoring of the forming process, such as using knowledge of a material's anisotropy to orient applied strain paths in a favourable direction, are two examples of areas where material research can also play a role. The work described in this thesis falls into these areas of material research.

Historically, process development and tailoring of microstructures has been done experimentally. Material can be cast, hot rolled, cold rolled, heat treated, pressed, or subjected to

other potential microstructure-influencing processes, or any combination of the above, in order to create new microstructures. These new microstructures are then tested and examined to identify any correlations between microstructural features and testing response trends. This is a time consuming endeavour and requires extremely large equipment resources. A more recent approach has been to use numerical modelling to study microstructural effects. The increasing prevalence of numerical modelling is due to advancements in computer technology that allow for highly efficient and powerful computing systems to be available at low cost. Aside from the cost side of equipment and other essentials, the main advantage of numerical modelling for microstructure research is its ability to isolate individual features of the microstructure and vary these features while holding other things constant, and thereby provide an in-depth understanding of the influence of the isolated feature on the results. This capability is extremely useful, given the complexity of microstructures and the large number of influencing factors. It is not possible to gain similar knowledge experimentally since most response tests are destructive, which forces each test to be on a slightly different microstructure.

There are still many unknowns in the field of numerical modelling of microstructures. Numerical models exist on all scales, from the atomic level up to the macroscopic, complete-part level. This research focuses on the microscopic level, where grain shape, size, and orientation are studied by representing each grain with multiple finite elements. Each element represents a certain portion of a grain and uses a single crystal constitutive law to represent its behaviour. The largest entity that needs to be established for this level of numerical modelling is the accurate representation of the microstructure. The elements themselves use validated single crystal formulations, which have been shown to accurately represent the behaviour of the material inside the grains. The method does not, however, have any way of dealing with grain boundaries or

change in material properties close to a grain boundary. This work also explores some of the options available for including some grain boundary phenomena, in an attempt to improve the accuracy of the numerical models while still maintaining a reasonable amount of computational efficiency. There are many other features that can be found within microstructures that have an impact on the material response, such as precipitates, inclusions, pre-strain and so on, but these will not be considered in this work. By introducing a method of capturing the influence of grain boundaries, relationships such as the Hall-Petch (Singh et al. [2002]), in which grain surface area fraction is considered, can be predicted. This will allow the effect of grain refinement on microstructures under study to be considered in the product development.

When customizing a material's microstructure for the purpose of enhanced formability, the type of deformation that the material is expected to withstand needs to be established. A common deformation mode seen during the construction of an automobile is bending. Body panels are subjected to hemming operations along their edges. These hems can be used to join multiple panels, or simply to remove any sharp edges. Either way, the hems are often visible on the end product, and therefore the performance of the material during the hemming operation is crucial. A common occurrence during a hemming operation is the development of surface roughness. This roughness is detrimental in many ways: Added surface roughness can lead to failure due to cracking during the forming process; it can render the final product more susceptible to fatigue failure; and it can cause undesirable visual imperfections on the final product.

One objective of this thesis work is to identify what microstructural orientations that commonly exist in aluminum lead to the development of large surface roughness. By identifying the troublesome orientations, the automotive companies can develop their material processes in ways that will allow for the suppression of the formation of these undesirable orientations. This

advancement would mean being one step closer to the overall goal of optimum product development.

This research will (i) develop new modelling frameworks that can accurately represent the microstructure in FCC polycrystals, (ii) employ the so-called crystal plasticity finite element method (CPFEM) to study the role of grain orientation on non-uniform strain partitioning during bending, and (iii) employ the CPFEM to study the role of grain boundaries on non-uniform strain partitioning during bending. This work will investigate the methods of representing grain boundaries within the FE mesh and evaluate their impact on the numerical results obtained during bending simulations. The scope of this research is outlined as follows.

The work will include a study of the impact of grain orientation on the developed surface roughness during bending. Polycrystals containing two orientations will be studied to investigate the effects of grain interaction. For the purpose of this thesis, these polycrystals will be referred to as bi-crystals. The objectives of this study are to analyse the effects of each texture component on the developed surface roughness, and the effects of bend axis orientation. The motivation for studying the effects of bend axis orientation is that some textures' ideal orientation, such as Goss and Cube, appear identical when viewed along the rolling direction, but very different when viewed along the transverse direction. The results of this study will allow manufacturing designers to tailor forming processes to orient bends in such a way as to maximise the formability of the material. The results from this study will be linked with experimental results found in the literature.

This research work will also include a study of grain boundary characterization within crystal plasticity simulations. Single crystal studies have resulted in crystal plasticity material

parameters that fit with single crystal data, but do not accurately predict polycrystal response. Relationships such as the Hall-Petch give reason to believe that grain boundary characterization is a very likely cause of the discrepancy between single crystal-fitted crystal plasticity material parameters and polycrystal-fitted material parameters. By creating simulations using the single crystal material parameters and varying the grain boundary material properties to fit the polycrystal material response, a greater understanding of grain boundary effects can be obtained. The objectives of this study are, (i) numerically reproduce single crystal experimental results found in the literature in order to identify the crystal plasticity material properties needed for single crystal response, (ii) use the polycrystal experimental response observed for the large grain AA5754 sample created at McMaster University by Zhu et al. [2011] to identify the grain boundary zone properties required to allow the use of the single crystal material properties for the grains, and (iii) perform bending simulations, and analyze the resulting surface roughness.

The two proposed bending studies will together provide a deeper understanding of the influence of microstructure and microstructure modelling on the performance of FCC polycrystals during bending.

2. Background

Many technical fields interact in this research. In the following sections, the current understandings that underpin the studies are discussed. First, the general considerations for building the numerical model are discussed. Next, current knowledge of certain microstructural phenomena is reviewed, such as grain boundary characterization and crystal orientation dependent response. Finally, the bending loading condition and its relationship to aluminum are explored.

2.1. Numerical Modelling

The push towards computer based numerical simulations of material behaviour is driven not only by an interest in speeding up product development, but also by a desire to gain a greater understanding of the physical mechanisms occurring during material deformation. Crystal plasticity theory dates back to a time long before the idea of modern parallel computing was conceived. Its early development was done using time-consuming hand calculations for the purpose of understanding the role of dislocations and atomic crystal structure in the plastic flow of metals. With the introduction of the Finite Element Method and large computational resources, crystal plasticity theory became a new and impressive application of numerical modelling. In the following subsections, the development of crystal plasticity theory will be discussed (the full derivation will be provided later), and the requirements that need to be met in order to conduct a numerical model will be reviewed.

2.1.1. Crystal Plasticity Theory

Crystal plasticity theory entails the study of material yielding due to the motion of dislocations. Dislocations are crystal lattice imperfections which will glide along specific

directions when sufficient stress is applied (Schmid's law, Schmid [1924]). The result of a dislocation motion is a slight shift of the crystal lattice. When large numbers of dislocations move under an applied load, the material is considered to have undergone plastic strain. The specific directions along which the dislocations can move depend on the crystal lattice structure of the material. For FCC metals, there exists a set of 12 slip directions (slip vectors) on 4 slip planes known as the close packed planes (Figure 1 shows an example of a slip plane). Since there are only 12 possible slip directions, the overall dislocation motion will be divided amongst these 12 directions based on the resolved shear stress applied in each slip direction. The final plastic strain is a function of the division of the dislocations amongst the 12 slip directions. By considering the orientation of the crystal lattice with respect to the orientation of the applied stress, the final deformation of a material consisting of one uniform crystal (single crystal) can be determined. The underlying assumption here is that translational glide is the principal contributing factor to material deformation, and neglects other phenomena such as twinning or dislocation climb.

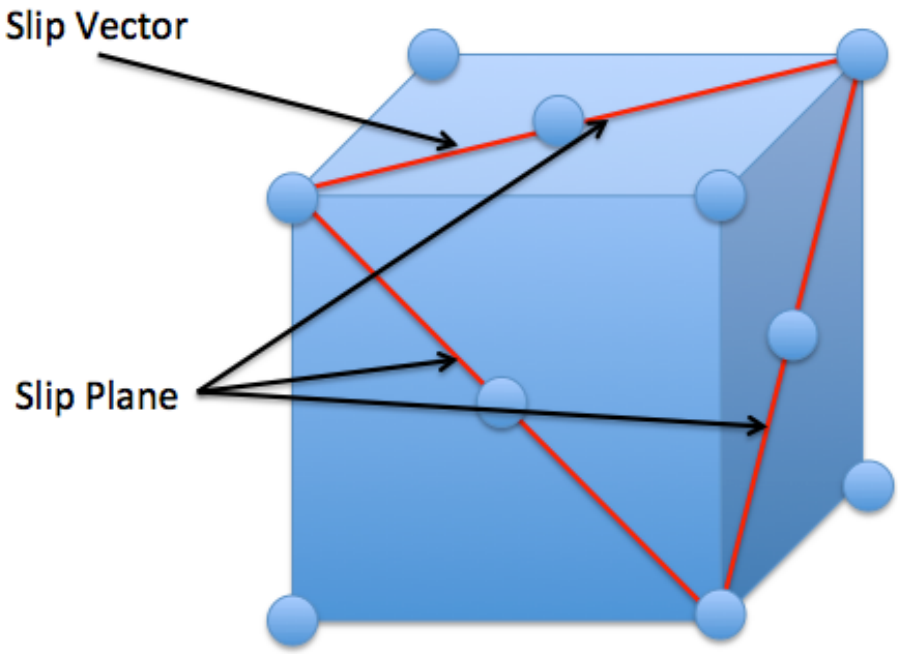

Figure 1: Example of FCC Slip Plane and Slip Vector.

2.1.1.1. Schmid's Law

The Schmid law is the foundation on which crystal plasticity theory was developed. The law relates the glide of dislocations with an applied stress on any given system. The stress needs to be represented as the resolved shear stress on the dislocation slip system in question, and the existence of plastic slip can be established as follows for rate-insensitive plasticity:

$$\dot{\gamma}_{(\alpha)} = 0 \qquad \text{for } \tau_{(\alpha)} < \tau_{y(\alpha)}, \tag{1}$$

$$\dot{\gamma}_{(\alpha)} = 0 \qquad \text{for } \tau_{(\alpha)} = \tau_{y(\alpha)} \text{ and } \dot{\tau}_{(\alpha)} < h_{\alpha\beta}\dot{\gamma}_{(\beta)}, \tag{2}$$

$$\dot{\gamma}_{(\alpha)} \geq 0 \qquad \text{for } \tau_{(\alpha)} = \tau_{y(\alpha)} \text{ and } \dot{\tau}_{(\alpha)} = h_{\alpha\beta}\dot{\gamma}_{(\beta)}, \tag{3}$$

where $\dot{\gamma}_{(\alpha)}$ is the shear rate on slip system α, $\dot{\tau}_{(\alpha)}$ is the rate of resolved shear stress, and $h_{\alpha\beta}$ are the elements of flow stress on system α due to an increment of shear on system β.

Equation 1 represents the inactive system, Equation 2 represents a potentially active system, and Equation 3 represents an active system.

2.1.1.2. Sachs Model

Using Schmid's law, Sachs [1928] began with the simplest assumption that only one slip system would be active at a given time. The macroscopic stress was applied, and the slip system with the largest resolved shear stress was used to begin plastic deformation. Downsides to this model include the fact that not all final deformations could be obtained and situations such as the double slip condition, when the resolved shear bisects two slip directions, could not be represented. Another issue with the Sachs model is the loss of strain compatibility across grain boundaries when one is dealing with polycrystal models, a point discussed in greater detail shortly.

2.1.1.3. Taylor's Plastic Slip

Taylor [1938] postulated that five independent slip systems could be chosen to create a deformation state that matches an applied strain. This assumption is needed since the solution to an applied strain problem is not unique when more than five slip systems are considered. This conclusion of five independent slip systems came from Taylor's observation regarding the deformation of a cube of material. Taylor noted that the deformation could be fully characterized by measuring the stretch of six independent directions. An analogy can be made between the six independent stretches and the six independent components of a strain tensor. When a further detail is included in the characterization, such as the conservation of volume during plastic slip,

only five independent measurements need to be obtained and the sixth measurement required to preserve volume can be calculated. When dealing with slip systems within a microstructure, the same rule of five independent values holds true; therefore if one could identify the five independent slip systems most likely to be active, the problem can be fully solved. The selection of the five active slip systems requires analysing all possible combinations of five slip systems (there are 384 possible combinations in an FCC structure) and selecting the combination that minimizes total slip. Bishop and Hill [1951a; 1951b] later identified that the active stress states on a crystal occur at the corners of its yield surface, which narrows down the possible active slip systems and reduces the number of combinations to be checked. Bishop and Hill [1951a; 1951b] also changed the criterion for choosing the final combination of slip systems from Taylor's minimum slip to a maximum plastic work criterion.

2.1.1.4. Rate Dependent Formulation

Early crystal plasticity models were rate-insensitive and required that simplification assumptions be made. Budiansky and Wu [1962], Hutchinson [1970], and Hill and Rice [1972] created small strain formulations of Taylor's plastic slip theory. The amount of slip on each slip system was governed either by the strain increment or by comparing a stress increment with the strain-hardening modulus. There could be ambiguities with the rate-insensitive approach because the choice of five slip systems was not always unique.

Current crystal plasticity models are rate-sensitive, which allows the rate of dislocation slip to be considered on all slip systems. The rate of slip on a system depends on the current stress as well as the current hardness of the system. The amount of dislocation motion on all slip systems is determined by the rate of slip on the respective systems. The introduction of rate-sensitivity removes the problem of non-uniqueness encountered with the rate-insensitive models. It is the

rate-sensitive model developed by Asaro and Needleman [1985] that will be used for this research.

2.1.1.5. Polycrystal Averaging

Crystal plasticity theory deals with predicting anisotropic stress and strain distributions based on the orientation of a single crystal. Real metals, however, are polycrystalline. They are composed of a collection of grains (regions of space with the same crystal lattice orientation), each with its own orientation. These orientations are often not random, but instead are aligned with a set of preferred orientations called texture. For crystal plasticity models to be able to predict polycrystal behaviour, they need to account for multiple orientations.

Early polycrystal models require some assumptions to be made regarding the strain or stress distribution across the different grains. The Sachs model [1928] assumes that all grains within the polycrystal are subjected to the same stress state and that only one slip system is active in each grain. This results in a situation in which each grain may deform differently under the same stress state due to the variation in orientation. If one were to try and assemble all the grains together in their final configuration, there would be gaps in the model where the grain on one side of a boundary deformed differently than the grain on the other side. This would result in a loss of strain compatibility. Kochendorfer [1941] modified the model to assume each grain is subjected to the same stretch, solving the strain incompatibility issue. The overall stress and strain response could be achieved by averaging the results from all the grains. The consequence of this assumption is that the stress in one grain differs from that in the next, which does not maintain compatibility of stress across grain boundaries.

Taylor's polycrystal model is similar to Kochendorfer's version of the Sachs model where the strain applied to each grain is constant, and equal to the macroscopic strain. Taylor's model, however, considers five slip systems to be active as mentioned earlier. The final stress calculated is the average of stresses for all the grains within the polycrystal.

A polycrystal method based on Eshelby's [1957] model proposed by Kröner [1958], Budiansky and Wu [1962], and Hill [1965] as a Self-Consistent model treats the deformation of each grain within the polycrystal as the solution for an elastic elliptical inclusion within a homogeneous matrix whose moduli are an average of values for all the grains.

For the purposes of this thesis, finite element calculations in which the element size is so fine that each element contains only a single orientation will be used, which allows the use of single crystal calculations instead of using one of the polycrystal models mentioned here.

2.1.2. Finite Element Analysis

There are three requirements for numerical modeling using finite element analysis:

1. A finite element mesh of the material (assembly of small regular shapes combined to form the complete entity which includes any microstructure information).

2. The boundary and loading conditions subjected onto the entity.

3. The material behaviour (constitutive model) that dictates the relationship between the deformation of the elements and the stress incurred within the element.

Constitutive models have several forms; two common forms are phenomenological models and mechanism driven models. Phenomenological models predict material deformation based on a representative yield surface of the material. This yield surface can be isotropic or anisotropic

(independent of or dependent on rolling direction), and symmetric or asymmetric (independent or dependent on compressive vs. tensile loading). Phenomenological models generally are more efficient than mechanism driven models, and are needed to model full parts undergoing forming operations (even though a certain amount of accuracy is sacrificed) due to the large number of elements required to model a full part. While phenomenological models may be acceptable for large-scale modeling, they lack the capability to provide insight on the deformation mechanisms operating within the material. In order to gain understanding of these deformation mechanisms, a mechanism driven model is required. This is where the crystal plasticity theory discussed previously is applied. Crystal plasticity theory can account for the anisotropic behaviour of each grain to be predicted based on its orientation. This allows for prediction of non-uniform stress and strain distributions and provides insights on the influence of the deformation mechanisms on failure. There have been many cases of crystal plasticity being used to study a range of material instabilities. For example, Peirce et al. [1982] used crystal plasticity to predict shear bands in tensile single crystals; Wittridge and Knutsen [1999] investigated surface roughness in aluminum using a polycrystalline model; Dao and Li [2001] used crystal plasticity to predict crack initiation during bending of polycrystals; Potirniche et al. [2006] used crystal plasticity to investigate void growth and coalescence in single crystals; Inal et al. [2010] used crystal plasticity to accurately predict the yield surface of an aluminum polycrystal; and Lim et al. [2011] predicted the pile up of dislocations at grain boundaries. The work done in this thesis uses crystal plasticity theory to expand the knowledge of some of these instabilities by studying surface roughness phenomena during bending, and grain boundary effects.

In order to make use of finite element analysis, the model representing the microstructure and simulations representing the material deformation need to be created. In the following sections,

the issues to be considered for creating a model suitable for crystal plasticity theory based finite element modeling are discussed.

2.1.3. Representative Volume Element (RVE)

One issue to be considered when setting up the model is, exactly how much of the material should be included? There are large computational costs involved in using crystal plasticity theory based constitutive models; therefore the models tend to be limited to a few hundred grains. This limitation gives rise to the use of a representative volume element (RVE) to represent the material. A representative volume element is a small section of the material that should be large enough that all local anomalies average out to represent the macroscopic material response, but small enough that a fine mesh can be created using sub-grain sized elements, while still maintaining a reasonable computational cost. Examples of RVE studies can be found in Cherkaoui and Berveiller [2000], Watanabe et al. [2005], Nakamachi et al. [2007]. One can learn about grain interactions from these RVEs and develop understandings of the material that can be the basis to rule out specific microstructures and engineer other microstructures for given applications.

The accuracy of any formability simulation based on crystal plasticity theory depends on the quantity and quality of microstructural information that the numerical model contains. The grain structure and orientation of the material of interest is needed for the simulation. Previously, 2D RVEs were commonly used for these studies, which would use a 2D material data scan to create the model. Due to advancements in computer technology, numerical models are no longer limited to 2D studies, and now three-dimensional (3D) microstructure information as well as 3D finite element meshing techniques that can incorporate these microstructures are required. The

following section discusses various approaches to incorporate microstructure information into a finite element mesh.

In this thesis, the details on developing the RVE, from a microstructural standpoint, for use with crystal plasticity theory-based simulations will be investigated and tailored to best suit the study being done. The tools used to build these RVEs will be available for use in future RVE studies.

2.1.4. Representative Microstructure

Characterizing the 3D microstructure of real materials is a difficult task to undertake because the standard grain orientation analysis technique, Electron Backscatter Diffraction (EBSD), is two-dimensional (2D). A 2D scan can be done on a carefully prepared surface to get a picture of the grains and their orientation for a single plane of the material; however, this is not sufficient, because a 3D picture is needed. There are multiple methods for obtaining a 3D material data set from 2D scans – as will be discussed in the next few subsections. Serial sectioning of the material to reveal multiple 2D surfaces is the most common method used, but the major disadvantage is that the technique is very slow. In order to overcome the time-consuming serial sectioning process, microstructure generating techniques have been developed in which statistical approaches are used to approximate 3D microstructure features using only a couple 2D scans. Construction of 3D data will be discussed shortly, but first, the issue of the size of the microstructure is discussed.

2.1.4.1. Representative Sample Size

When 2D EBSD scans are collected during any given material study, there is always the question of how big an area should be collected. The larger the area, the more likely the scan will

be representative of the overall microstructure; but with a larger area the scan time is increased and the size of the data to be managed is also increased. Given the high computational demand of crystal plasticity theory-based constitutive relationships, reasonable models are limited in size. It is important to gain a clear understanding of the relationship between scan size and microstructure representation, in order to be fully aware of the influencing factors in the material research.

The main entities being extracted from an EBSD scan are grain size, morphology, size distribution, orientation distribution and misorientation distribution. Some researchers have concluded that a minimum area is needed, for example Davut and Zaefferer [2010] concluded that at least 0.275 mm^2 of data is needed; however, intuition quickly leads to the conclusion that the necessary scan size depends on the grain size of the material. A general consensus seems to be that ~1000 grains would yield a representative sample (Wright et al., [2007], Baudin and Penelle [1993]). Brahme et al. [2012] approached the problem of establishing a minimum representative scan size by casting it in terms of information theory, and were able to show that the optimum scan size is ~10 times the effective grain size.

2.1.4.2. Serial Sectioning

In order to get a real 3D image of the material, multiple 2D scans are required where layers of the material are removed between successive scans. The process of removing material in layers to obtain 3D information is called serial sectioning. The following subsections briefly describe two serial sectioning techniques.

2.1.4.2.1. Mechanical Polishing

Serial sectioning techniques, such as the one described in Li et al. [1998], consisted of making pyramidal indentations in the surface of the material being analysed, and then using mechanical polishing between scans to remove the layers of material. The change in size of the pyramidal indentation on each scan allows the material scientist to calculate the amount of material removed for each layer; however, this assumes the material is removed evenly over the whole surface being polished.

Since the amount of material removed during mechanical polishing depends on the applied pressure, polishing time, and polishing medium, the distance between the scans can vary. To reduce the variability of the amount of material being removed, polishing machines have been built to robotically control as many variables in the polishing process as possible. Some have even been integrated into EBSD data collection systems to remove the need for a technician to transfer the sample between scanning and sectioning operations.

2.1.4.2.2. Dual Beam Focused Ion Beam

Modern technological advancements have allowed the introduction of the Focused Ion Beam (FIB) to perform micron-level material machining; the use of a FIB requires a vacuum environment which is the same as EBSD. Dual Beam FIBs have been introduced to the material science world, combining the machining capabilities of a FIB with the orientation scanning ability of EBSD, all within the same environment. This eliminates the need for material transfer between operations. Another advantage of the Dual Beam FIB for serial sectioning is that the amount of material removed during the FIB machining is controllable and repeatable (Matteson et al., [2002]).

Because EBSD processes are highly sensitive, the surface preparation of the material will affect the quality of the results. For mechanical polishing, strict polishing procedures are required, consisting of specific polishing media and surface cleaners, as well as careful sample storage. Preparing these procedures for new materials is an art in itself, and it can be time-consuming since each variation to the procedure needs to be validated with a complete polishing operation followed by EBSD scan. The quality of the EBSD surface preparation done by the FIB is dependent on the beam parameters – voltage and current – used for the machining. Typically, the trade off is that low power increases machining time but also increases surface preparation quality. Since the beam can make small precise cuts, selection of optimum beam parameters requires making a series of different powered cuts on the same sample surface, then taking an EBSD scan of the entire cut region. The fastest machining parameters to produce good quality data can be identified from the single scan, and the serial sectioning procedure can be started.

Both mechanical polishing and FIB machining take a long time; to obtain a set of 60 to 100 scans, several days at least are needed to go from raw material to measured data.

Once the material scans have been obtained, the scans need to be aligned. No two scans will be perfectly aligned, with one on top of the other. To solve this issue, alignment marks can be used to shift the scans to rebuild the 3D image of the microstructure.

2.1.4.3. High Energy Diffraction Microscopy

In order to avoid destructive serial sectioning techniques, material scientists have started exploring the use of X-rays to investigate the grain structure of metals. X-rays penetrate a sample, and the diffracted patterns are measured. By analysing the diffracted pattern, the orientation of the region being probed can be identified. Current capabilities can allow for beam

sizes on the sub-micron scale, with penetration depths up to the cm scale, depending on the material being probed (Lienert et al., [2011]). By using multiple detectors, the exact location of the point of diffraction can be identified and the 3D structure can be characterized. Since this is a non-destructive method for measuring microstructures, it enables the tracking of microstructure evolution during in-situ tests, and allows initial microstructures to be measured for FE model input before loading and sample destruction occurs. A disadvantage is, the resources required to perform HEDM are extensive and beyond the capabilities of most researchers. A dedicated beam-line is required.

2.1.4.4. Synthetic Microstructures

Due to the difficulties faced by serial sectioning (high equipment cost, time consuming material removal, alignment of scans), microstructure generation techniques have been created to build 3D microstructures from 2D EBSD data. These techniques range from simple assumptions applied to 2D scan data to complicated statistical analyses. The following subsections describe the more common forms of synthetic microstructure generation.

2.1.4.4.1. Columnar Microstructures

The simplest method of creating 3D microstructure data is to extrude the grain structure from a 2D scan to create a 3D columnar structure (Figure 2). There are several problems with this method, including the fact that since grains are three-dimensional in reality, the 2D cross section of a grain may not be representative of the overall size and morphology of the grain. In other words, it may just be the "tip of the iceberg." Another problem with this approach is that all the grain boundaries within the structure are aligned with the scan extrusion direction. This approach can be useful if the material itself exhibis a columnar structure as shown in Bhattacharyya et al. [2000].

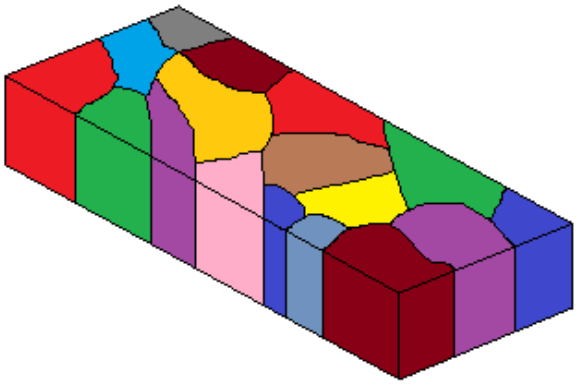

Figure 2: Example of columnar microstructure.

2.1.4.4.2. Structured Microstructures

An alternative method of creating 3D microstructures is to make a series of uniform volume filling shapes, such as bricks or octahedrons (Delannay et al., [2006]), that can be considered grains, and then assign to each of these shapes an orientation measured from the 2D scan (Figure 3). The downside of this approach is that each grain is considered to have the same size and morphology.

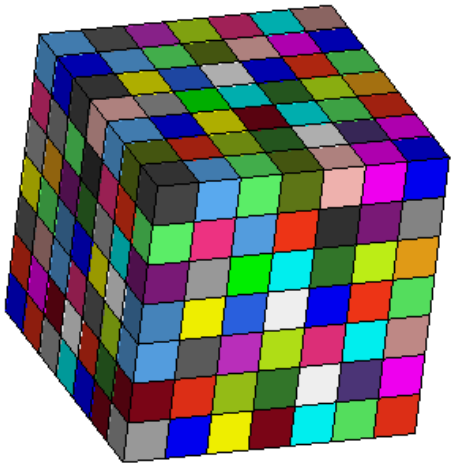

Figure 3: Example of random microstructure.

2.1.4.4.3. Statistically Equivalent Microstructures

The so-called M-Builder, developed by Rollet and co-workers (Saylor et al., [2004]), is one of the most advanced microstructure generation procedures, where two orthogonal 2D scans of the material are required. These scans are analysed to identify grain aspect ratio, orientation distribution, and misorientation distribution (difference in orientation between neighbouring grains). A volume of space is filled with ellipsoids of different sizes, with aspect ratios that match the measured grain aspect ratios. Points are then randomly introduced into the region, and a volume Voronoi tessellation is performed to make a non-interference, volume filled structure. All the Voronoi cells created from points that reside within the same ellipsoid are joined to become a single grain. The grains are then assigned orientations, and the orientation distribution and misorientation distribution are calculated. The values of these distributions are then compared with values from the original 2D scans. If any discrepancies are found, an iterative approach is used to adjust the grain orientations until the distributions within the generated structure match the 2D scans. Figure 4 shows an example M-Builder microstructure.

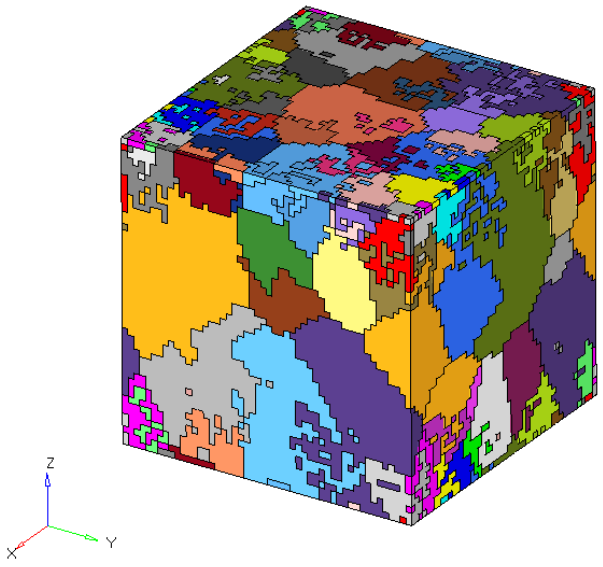

Figure 4: Example of M-Builder microstructure.

2.2. Grain Boundaries

The physical structure of a grain boundary is a planar interface; however, the grain boundary-affected region exists as a volume of material near the grain boundary. Whether the boundary should be modelled as special 3D elements, or whether the boundary should be left as planar interfaces in the FE models is a question of ongoing research. A huge amount of research has been done experimentally with the aid of bicrystalline pillars to isolate the specific grain boundary misorientation (Chalmers [1937], Aust and Chen [1954]). As technology advanced, transmission electron microscopes (TEM's) became available, thin films of samples could be created, and individual grain boundaries could be cut from the overall microstructure and studied (Mompiou et al., [2009]). By taking the thin samples and straining them in-situ, observations could be made of dislocation motion and grain boundary migration. In an attempt to reproduce the observations made during the various experimental studies, atomistic modelling based on molecular dynamics was developed.

2.2.1. Atomistic Models

As mentioned, grain boundaries are where two regions of different crystallographic orientation intersect. Since the physics of what transpires at the grain boundary is at the atomic scale, models representing a collection of atoms operating under the principals of molecular dynamics have been created, and are aptly named atomistic models. The current approach in atomistic modelling is to use the Embedded Atom Method (Baskes [1984]), which treats each atom as an energy embedded in a matrix. Atomistic models are not intended just for grain boundaries, they have been used for a wide variety of applications where phenomena occur at the atomic level, such as hydrogen embrittlement, in which voids in a metal crystal structure are filled with hydrogen atoms and nearly all plastic deformation is impeded (Angelo et al., [1995]).

Kheradmand et al. [2013] used atomistic modelling to study the role of grain boundaries and the hardening effect of ultra-fine grain size. The Hall-Petch effect is consistent with experimental observations for a wide variety of grain sizes, but it typically falls apart at the ultra-fine grain size level. The general understanding of the Hall-Petch effect is that dislocations pile up at the grain boundaries and impede further dislocations, but that dislocation pile-up at the ultra fine grain size is not as straight forward. Kheradmand used his atomistic models to identify that with larger grains, the dislocations would chose a path of least resistance and travel along the boundaries where the dislocation pile up would be predictable. With a grain size below 1 micrometer, however, dislocations are no longer capable of moving along grain boundaries and are forced to interact with the boundary directly at all times. This drastically changes the slip resistance of the material and explains the divergence from the Hall-Petch relationship.

While atomistic modelling can shed great insight into the interactions and mechanical responses at a grain boundary, the computational cost of this approach is high. The goal of this thesis work is to find a relatively computationally efficient method of representing grain boundaries in the crystal plasticity models, so atomistic modelling is not used.

2.2.2. Grain Boundary Elements

The physical concept of a grain boundary is the boundary between two regions of material with different orientations. As described in the literature, most of the existing crystal plasticity models do not have any special calculation or consideration at the grain boundary; they merely represent the boundary by having two neighbouring elements with different orientations. Some success has been seen in the understanding of grain interactions using this method (Rossiter et al., [2010]). The downside to not treating the grain boundaries differently from the grains is that several grain boundary phenomena are neglected, such as grain boundary slip. However, plenty

of models are described in the literature where grain boundaries are represented by distinct elements. The two main types of elements used to represent the boundaries are volume-representing elements and cohesive interface elements. The distinction between these two types of elements is that volume-representing elements (whether it be a 2D or a 3D model) model the grain boundary-affected zone as a region of material following the behaviour of a continuum-based constitutive law that may differ from that of the grain material. A cohesive interface element used for representing a grain boundary will be a planar interface separating the two grains, and it can deform and distort in a variety of ways depending on the cohesive law used. Both the volume-representing element approach and the cohesive interface element approach will be discussed in the next two subsections.

After considering what exactly is being used to model the grain boundary, the next hurdle with respect to grain boundary elements is in defining their size and layout. Grain boundaries are not smooth curves, but rather rough, jagged interfaces. Capturing the rough features of the grain boundaries can require many small elements that can reduce a simulation's efficiency. Subsection 2.2.2.3 discusses the options available.

2.2.2.1. Cohesive Interface Models

A common way of representing grain boundaries is to introduce cohesive elements into the models as surface elements contouring the grain boundaries. Cohesive elements are traction and separation elements, which can operate under a user-defined set of laws. The elements can distort and break completely in a manner different from that of a typical continuum formulation. Cohesive elements have been used in a variety of failure models, the two most notable being the extrinsic failure model by Camacho and Oriz [1996] and the intrinsic failure model introduce by Xu and Needleman [1995] (Espinosa and Zavattieri [2003a; 2003b]). The major difference

between the extrinsic and the intrinsic models relates to the presence of the cohesive elements at the start of the simulation. With the intrinsic approach, elements are placed in preferred locations at the beginning of the run and their presence affects the results throughout the entire simulation. The extrinsic approach is more akin to an element erosion type failure model where the entire simulation is monitored, and when the constitutive material law identifies a region of material failure, the model is altered. In this case, the model is altered by splitting the element connectivity and inserting a cohesive element. These cohesive elements can appear anywhere in the model based on the material response. Since grain boundaries are predefined entities in a specific location and affect the material response from the onset of deformation, the intrinsic cohesive approach is the most appropriate option. Within the intrinsic formulation developed by Xu and Needleman [1993], the cohesive elements are such that the traction across the element increases with interfacial separation to a maximum value and then decreases until it disappears entirely. This aims at representing void nucleation and coalescence at the grain boundary. The length scales at which the traction force operates from onset, to peak value, to elimination is an arbitrary choice based on fitting the observations made from the individual material responses. Modifications have been made to this approach over time, such as the addition of a cohesive-friction law that takes over if the cohesive element fails under compressional loading (Benedetti and Aliabadi [2013]).

For the purposes of this work, cohesive formulations were attempted; however, the MPP-LS-DYNA code available for the work and used in this proposal was not capable of using cohesive elements in parallelized simulations. Due to the computationally intensive crystal plasticity-based constitutive model used as the basis for this research, parallelization is crucial for obtaining reasonable simulation run times. For this reason, cohesive formulations were not pursued.

2.2.2.2. Volume-Representing Element Models

The concept of volume representing elements being used to model grain boundaries relates to the physics of what goes on around the boundary. The mismatch of the crystal lattice structure at the grain boundary impedes dislocation motion, causing dislocation pileup. This pileup can affect the material properties surrounding the grain boundary, and it gives rise to the grain boundary-affected zone. 3D elements are placed in the model along the boundary with thickness equal to the grain boundary-affected zone. Like the cohesive element approach, this still requires use of an arbitrary length scale to build the model. In this research, the grain boundary-affected zone will be considered to be 20 μm thick, based on observations made on aluminum (Siamoto [2011] (personal communication)).

Onck and Van der Giessen [1999] developed a 2D "grain element" model, where the material is modeled by a regular grid of hexagonal elements (one element per grain) and the edges of each of these elements are separated from their neighbouring grain by a boundary element, as shown in Figure 5. The grain boundary elements were developed to account for creep phenomena and material cavitation.

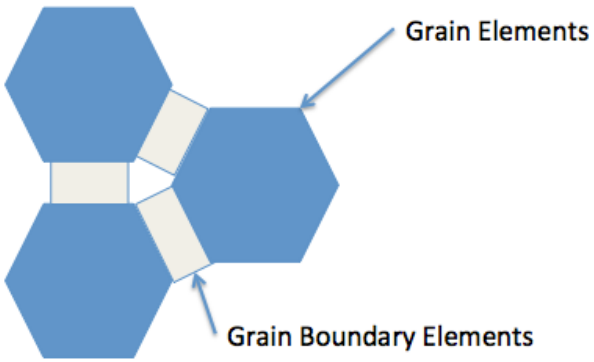

Figure 5: Grain Element Model (Onck and Van der Geissen [1999]).

2.2.2.3. Grain Boundary Smoothing

Modelling the rough, jagged surfaces of grain boundaries can require very small elements when compared to element sizes within the grains. This can cause large, inefficient meshes and small time step sizes. It is currently unclear what the effect of these fine geometrical details on the overall material response is. If these details can be removed and the grain boundary smoothed to a surface with large radius of curvature, then much larger elements can be used to model the microstructure. The coarse mesh would increase the minimum time step size of the simulation and reduce the number of elements required for the model. An understanding of the impact of the fine geometrical details is needed to either allow the complete removal of the features, or allow coarser elements to be used with a modification put in place to account for the smoothing operation. Either of these two options would allow for substantial improvement of the analysis capabilities of crystal plasticity-based FEA.

Smoothing out the grain boundaries and modelling them with larger elements has the potential to increase a model's efficiency, but the accuracy of the simulations can be affected. The impact of capturing all the small features of a grain boundary on the response of the system is not explored in the literature, so it should be investigated.

2.2.3. Dislocation Density Models

Dislocation density-based crystal plasticity theory is a development that accumulates a number of dislocations within an element that in turn influences the slip resistance within that element. This development allows for the pileup of dislocations at grain boundaries to be considered. Lim et al. [2011] introduced a two stage model in which a standard crystal plasticity theory-based FE model containing dislocation density-based hardening characteristics is used for the first stage, and a dislocation-distributing algorithm is used for the second stage. The

dislocation-distributing algorithm occurs at predefined intervals and modifies the dislocation density around grain boundaries. The goal of the second stage is to represent physical phenomena associated with dislocation motion, such as nucleation, transmission and cancellation. The algorithm treats the boundary as a membrane, which allows some but not all dislocations to be transferred. This stage in the model is what allows dislocation pileups to be represented. The ability to represent the natural distribution of dislocations within a microstructure along with the ability to alter material response based on dislocation density allows the model to capture the hardening effect of grain refinement. The drawback to such an approach is added complexity of the model and computational costs. The objective of this work is to obtain a similar result (ability to predict the effect of adding grain boundaries) without incurring the large computational costs. The current crystal plasticity model used for this research does not have dislocation density-based hardening characteristics.

2.3. Mesh for Finite Element Analysis (FEA)

The construction of the models used in FEA simulations is critical to the accuracy of results. There are many ways of building a mesh and representing the grain structure of a material. Multiple grains can be represented by a single element, and a polycrystal model discussed above can be used to approximate the behaviour of the material region represented by the element. Alternatively, every element within the model can represent a single grain and behave in the manner that a single crystal of that grain's orientation would behave. Similarly, every grain within the material could be represented by many elements, each acting as a single crystal of that grain's orientation. For the purposes of this work, the latter method is used due to the ability to model grain morphology, local strain partitioning within the grain, and grain interactions.

There are two main methods of building the mesh that represents the microstructure: Gridded Mesh, and Grain Boundary Surface Mesh. They both have their advantages and disadvantages, and are both used in this thesis work. Both of these methods are discussed individually in the following subsection.

2.3.1. Gridded Mesh

Building the mesh for the FE simulations from the 3D grain data can be performed in many ways. Since the 3D microstructure data is typically in voxelized form (3D pixels) regardless of how the data was obtained, the simplest method of building the mesh is to create a grid of hexahedral (brick) elements the same size as the voxels and assign each element the orientation of the voxel it represents (Figure 4).

The advantages of this method include fast and efficient meshing procedure, complete control over the element size, uniform elements, and perfect element shapes with no distortion. The main disadvantage of this method is the inevitable existence of "staircase" grain boundaries.

This method is most suitable in situations where grain boundary performance is not of high interest and where many microstructural changes and adjustments are being made. It is useful for doing comparative studies where parameters within the model are being adjusted and their impact on the results are being analyzed.

2.3.2. Grain Boundary Surface Mesh

In order to make a mesh with smooth grain boundaries, a surface mesh that contours the grain boundaries can be made and the region of each grain can then be populated with solid elements. To achieve this, a program capable of identifying grain boundaries from the microstructure data and then placing elements along the boundaries is needed.

The disadvantages of this method include very complicated meshing procedure, which often can not be fully automated, little control over element size or element quantity, and highly varied elements. The loss of control over element size can be burdensome since explicit FE codes use minimum element size to control the maximum time step size.

The major advantage of employing a grain boundary surface mesh is the generation of smooth grain boundaries, and therefore, this approach is most appropriate when grain boundary phenomena are being studied.

2.4. Orientation Dependent Response (Textures in FCC crystal)

It is well known that many materials behave anisotropically, and after all, this behaviour is what has driven the research on crystal plasticity models. For metals, the specifics of the anisotropic behaviour are derived from the material's texture (preferred crystallographic orientations). Each material will have its own texture, and that texture is dependent on the material processing. The question then becomes what are the influencing textures on the specific material being studied. For aluminum, the main texture components are Cube, Brass, Goss, S1 and Copper. The orientation of these components can be described using a set of rotation angles. The common notation is with the use of Bunge angles, and the Bunge angles for the five aluminum texture components can be found in Table 1. The order of Bunge angle rotations is Φ_1,Φ,Φ_2. Since all of these texture components are created from the same crystal structure, their physical responses in the local coordinate system of the crystal are identical. It is when the global coordinate system of the material is considered that differences arise. Each of these orientations has a distinct response when loaded relative to the global coordinate axes. Cube texture tends to be a relatively soft orientation since the resolved shear stress of a load applied to one of the global coordinate axes happens to coincide closely with the orientation of a material slip plane.

Then one can observe S1 and discover that it is quite hard with respect to all axes. An interesting orientation to consider is Goss. The only major difference in orientation between Goss and Cube is $\Phi = 45°$. Since the order of the Bunge angle axis rotations is ZX'Z", the crystal orientations relative to the X axis are identical, but the orientations with respect to the Y and Z axes are 45° away between Goss and Cube. Kuroda and Tvergaard [2007] showed that when Goss is pulled along the X-Axis, it exhibits a very soft response that matches that of Cube, but when it is loaded in the transverse direction it becomes the hardest orientation (Figure 1a-b). This feature of Goss plays a major role in the findings of the work done in this thesis, and will be discussed further in later sections.

Table 1: Euler angles for the orientations used in this study

Orientation (Texture component)	Φ_1	Φ	Φ_2
Cube	0	0	0
Goss	0	45°	90°
Brass	35.26°	45°	90°
Copper	90°	35.26°	45°
S1	59°	37°	63°

2.5. Bending of Aluminum

When producing virtually any component out of sheet metal, it is very likely that a certain amount of bending must be withstood during the forming process. The most notable bending load in most cases is due to hemming. Hemming of the metal's edge is used as a multi-purpose action that removes sharp edges, stiffens the material, and can join panels together. Hemming typically consists of a very tight bend radius, which increases the material strain at the bend. Bending loading condition is a unique and complicated loading condition that has multiple simultaneously

occurring regions. There exists the outer (tensile) side of the bend where the material is in tension along the arc of the bend. Within this region the material is forced to thin due to a plane strain condition that arises when dealing with a long piece of material being bent, such as a hem. On the inner (compressional) side of the bend, the material is compressing along the arc of the bend, which forces the thickness to expand due to the same plane strain condition. At the interface between the inner and outer regions of the bend exists the neutral axis, where the material does not stretch or compress; however, this does not mean the material is unaffected. For the regions of material at the ends of the hem where the plane strain loading condition no longer applies, the material in the outer region of the hem will not only thin, but also contract in the direction parallel to the bend axis. The opposite occurs in the inner region of the bend (the material expands parallel to the bend axis). This creates a situation where the material will "curl" slightly along the end of the hem (see Figure 6). The curled material tends to find itself almost entirely on the outer side of the neutral axis and experiences a large amount of tensile loading. It is this location of the material that is most likely to begin the failure process. To add to the complexity, there exist materials where compressional behaviour differs from tensile behaviour (such as Magnesium due to twinning behaviour), which can result in a shifting of the neutral axis and increased strain on the tensile side of the bend (Rossiter et al., [2013]).

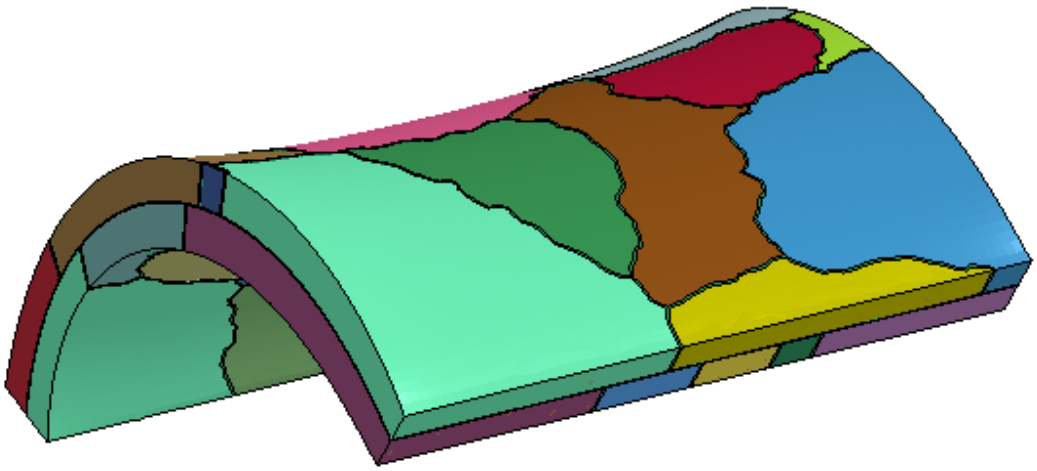

Figure 6: Phenomenon of edge “curl” during bending.

2.5.1. Applications of Bending for Material Research

Bending is not only found in forming operations, but has been used as a tool for metal research in a variety of applications. The most famous form of bending test is the rotational bend test used to evaluate the fatigue properties of materials. Duncan and Ragab [1973] demonstrated the usefulness of bending as a form of creep test. Ivlieva and Novikov [1990] used bending as a method of applying very localized high strain in order to help identify the burning temperature of aluminum. The approach looked for a transition between ductile failure of the bent aluminum and brittle failure. The onset of brittle failure indicated localized melting along the grain boundaries and, therefore, no stress being passed between the grains. Lloyd et al. [2002] described a cantilever bend test intended for use as a test that did not touch the surface of the sample bend and therefore provided good data for surface roughness analysis. The application was to use it for controlled radii bends, where previously a wrap bend test was used.

2.5.2. Measuring Strain During Bending

Early research into bending faced a serious challenge when attempting to measure the strain distribution found within a bend. Because the deformation changes at the edges of a bend, only the material deep within the hem is truly representative of the loading path. In consequence, unlike in typical tension experiments, the strain found within the specimen can not be identified using a grid or speckle pattern. Strain quantifications have been made in some materials using etching techniques sensitive to dislocations, or precipitates induced at dislocations, but this is not suited to all materials (Geist and Parker [1984]). Geist and Parker [1984] presented a method of measuring the plastic strain values found within AA5082 after bending; they took a series of microhardness measurements and correlated them with microhardness readings found in the same alloy subjected to highly controlled tensile tests with known local plastic strain levels.

2.5.3. Relating Bending Deformation to Tensile Deformation

In some cases attempts have been made to link bending performance with plane strain tensile results. Lin et al. [2009] performed a study relating the fracture strains of plane strain tension tests to the outer surface strain of the sample in a bend test at failure. Their results were reported as being consistent for two grades of aluminum tested. Iacono et al. [2010] proposed a simple formula to relate the minimum bend ratio with the reduction in area, hardening exponent, and yield stress of a tensile experiment. Thuillier et al. [2010] and Thuillier et al. [2011] described using a finite element model in conjunction with parameters derived from tensile tests of straight and notched specimens along with equibiaxial tests to predict the failure point of the material during hemming operations. They were able to monitor void growth parameters based on stress triaxiality, and had good correlation between a critical void growth value and the point of observed cracking in the real hemmed specimens.

2.5.4. Bending of Aluminum in the Automotive Industry

As mentioned previously, the automotive industry is highly motivated to reduce car weight, and using aluminum in cars in place of steel is an attractive solution. Aluminum 6061 can absorb up to seven times more energy in bending than steel for the given weight of material (Easton et al., [2006]). This has inspired a considerable level of research into the forming of automotive components with aluminum. Abernathy [1976] studied the use of aluminum for automotive hoods, and found that splitting of the aluminum forced the exterior surface of the hood to be steel while the inner brackets could be aluminum. Early automotive aluminum experiments used either AA5182-O or AA2036-T4 alloys. AA5182-O presented larger strain to failure over AA2036-T4 and was more readily formed, but exhibited low final strength and dent resistance. AA2036-T4 exhibited good strength but poor final surface appearance. Often, combinations of the two alloys were used depending on the specific component requirements. Evancho and Kaufman [1977] discussed the introduction of 6xxx series aluminum alloys as having the combination of the high formability of AA5182-O and high strength of AA2036-T4 alloys previously used for automotive body panels. It uses the aging characteristics of the AA6xxx series aluminum during the paint booth cycles to achieve this combination of formability and final strength. Finelli and Kelly [1977] produced an all aluminum hood using the same manufacturing technique as steel hoods (including joining by hemming) in order to make an interchangeable set of tooling to produce steel or aluminum hoods depending on the vehicles weight requirements. This was achieved by increasing the radius of the bend with a rope hem to reduce the occurrence of checking-related surface defects. Wolff [1978] delivered a comprehensive discussion on the formability of aluminum, in which an almost recipe-like outline of forming approach and tooling design is given, which highlights the use of rope hemming as the required method of closing the

edges of aluminum panels to prevent cracking. Several papers were published with the intent of convincing the metal forming industry to stop comparing the formability of aluminum with the formability of steel. The act of taking aluminum and running it through a forming operation tooled for steel, only to see the parts fail, is misleading about the usefulness of aluminum. Instead, these papers encourage the readers to consider redesigning the way cars are structured and parts are tooled, so as to enable the use of aluminum (Wheeler et al., [1987], Story et al., [1993]). Muderrisoglu et al. [1996] did a spring back study analysing the three stages of a hemming/flanging operation (bending, pre-hemming, and hemming) of Aluminum 1050, and encountered cracks as early as the pre-hemming operation. The final hemming operation produced enough cracking that the authors were unable to draw any spring back conclusions during that phase.

2.5.5. Quantifying Bendability of Aluminum

The automotive industry's interest in aluminum has led to extensive work characterizing the material's forming characteristics. Some typical figures reported for formability include Limiting Draw Ratio (LDR) and R-values. R-values give the relationship of the material's tendency to stretch in-plane with the sheet versus straining in the thickness direction. For example, a large R-value means the material is able to stretch further in the plane of the sheet for the same thinning as a low R-value material. Good draw quality steel will have r-vales close to 2 while aluminums show R-values in the 0.7-1.0 range (Jain et al., [1998]). Jain et al. [1998] studied the effect of tooling design on the LDR and showed that by keeping the profile radii on the punch large, the LDR for AA5754 can be brought above 2.0 and slightly out-performs AA6111. Sarkar et al. [2001] studied the bendability of AA5754 based on its iron (Fe) content. They showed that an increase of Fe content in AA5754 drastically reduced the bending limit of the material. This

outcome was caused by an increase in the abundance of Fe rich particles, which caused surface cracks on the tensile side of the bend, and these propagated through the material early on. Sarkar et al. [2004] then studied the effect of Fe content on AA6111, and they observed the same behaviour. Lloyd et al. [2002] compared the surface roughness characteristics and maximum bend angle of AA6111 and AA5754. Their findings showed that AA5754 out-performs AA6111 in both maximum bendability and surface roughness suppression (linked as being a contributing factor to the better bend performance).

A common tool for characterizing the formability of steels is the Forming Limit Diagram (FLD). Schleich et al. [2009] demonstrated that due to the ductile failure characteristics of aluminum, the FLD is not a useful tool for predicting the formability of aluminum during operations that involve a lot of bending. Instead, the concept of a Bending Limit Diagram was presented, where specimens were prestrained in tension and then subjected to pure bending. The resulting curve was reported to be more accurate for formability predictions of aluminum.

2.5.6. Finite Element Modelling of Aluminum Bending

With the introduction of powerful numerical modeling, Crystal Plasticity based FE modelling researchers began performing their own studies on the bending of aluminum. Dao and Li [2001] studied a variety of influencing factors on FCC bendability using 2D models. These factors included particle distribution and location, as well as crystallographic texture. Their results showed that rolling texture can have a significant detrimental effect on the overall bendability of the material as well as the particle distributions close to the surface of the sheet. Kuroda and Tvergaard [2007] presented an extensive paper comparing the bending response of each commonly found aluminum texture component. They reported that the Cube texture is highly advantageous for suppressing shear band formation and can be used to increase aluminum

bendability. Later, Ikawa et al. [2011] presented the results of a comparison between experiment and numerical simulation of bends with Cube texture and Goss texture. The study confirmed that Cube shows good bendability but that Goss has bendability characteristics that depend highly on the orientation of the bend axis. Shkatulyak and Pravednaya [2013] studied the texture development in aluminum 1050A and reported that with repeated bending, the quantity of Goss orientation increases and the quantity of Cube orientation diminishes. Hu et al. [2010] performed a micro-macro combined model to analyze the effects of particles on the wrap-bendability of aluminum. They presented a detailed observation of the effect of particle distribution on the propagation of shear bands in AA5754. They found that a random distribution of particles, such as that found in direction-chilled aluminum, exhibits much higher bendability than caused by stringer arranged particles such as that found in continuous cast aluminum. A follow-up paper by Davidkov et al. [2012] presented an experimental study of the same phenomenon using DIC measurements to try to capture the presence of shear bands being affected by the particle distribution.

Mattei et al. [2013a] performed a study aimed to assess the contribution of developed surface roughness to the failure of AA6016 in bending. Samples were partially bent, then polished to remove any resulting surface roughness, then bent further. The result was no change in the overall bendability of the material. It was concluded that the shear bands formed during the failure of the material were caused by microstructure characteristics such as grain interaction. Mattei et al. [2013b] extended the work into a finite element model where the grains are modelled by five shell elements and given a flow stress that varies from grain to grain. They claim that the model supports their conclusion that grain interaction leads to failure in bending.

2.5.7. Improving the Bendability of Aluminum

In order to try and improve the bendability of aluminum, heating operations have been implemented with a strong interest in laser heating. Mohammadi et al. [2012] presented a study investigating the effect on the bendability of aluminum AA2024 after it was heat treated using laser heating. It was shown that the spring back of the part can be reduced by 43%. Laser roller hemming is a process in which a laser is mounted just in front of the leading edge of a roller hemming operation. The laser heats the material as the roller makes each pass. This approach uses a combination of annealing and the higher forming temperature to achieve greater bendability (Levinson et al., [2012]). Another approach aimed at improving aluminum's bendability is to introduce layers of residual stress on the surfaces of the sheet using un-lubricated rolling. Weiss et al. [2012] presented a study showing the softening behaviour observed in AA6063 at various levels of thickness reduction using un-lubricated rolling. Comparing the effects to the result from uniaxial tensile loading experiments, they found that the softening effects of the residual stress layer were not present. Therefore this was a technique aimed solely at improving the bendability performance of the material. Jin and Lloyd [2013] studied the effect of cladding AA3003 onto AA6xxx aluminum. The aim was improve the bendability of the material by introducing a surface layer that could withstand the plain strain loading condition of the outer surface of the bend without breaking and causing crack initiators. The results proved quite favourable, with positive effects on the bendability of the material even with cladding thicknesses less than the average grain diameter.

3. Constitutive Model

Since the current work involves the use of finite element analysis, a constitutive model is required for characterising the material. As previously mentioned, this research deals with crystal plasticity theory to predict the stress versus strain response of the material. Ls-Dyna explicit is used for this research due to its highly parallelizable MPP (massively parallel processing) version. The following subsection presents the formulation of the crystal plasticity theory-based constitutive model implemented into LS-Dyna and used in the current work.

3.1. Kinematics and Constitutive Framework

Two main deformation mechanisms are being considered within the constitutive model: crystallographic slip, and elastic distortion of the lattice. These two mechanisms combine to form the total deformation of the crystal structure. For an FCC structure, crystallographic slip occurs on the $\{111\}\langle 110\rangle$ slip systems to form plastic deformation. These slip systems consist of slip planes $\{111\}$ with normals $\boldsymbol{m}$, and slip directions $\langle 110\rangle$ with slip vectors $\boldsymbol{s}$. In the two stages of total plastic deformation, the first is conceived as undergoing dislocation motion under various slip systems, leaving the lattice vectors undistorted and in their original orientation. In the second stage, lattice vectors distort and rotate to their final position.

The deformation gradient tensor $\boldsymbol{F}$ is taken to use multiplicative decomposition, and is written as

$$\boldsymbol{F} = \boldsymbol{F}^{*}\boldsymbol{F}^{p}, \tag{4}$$

where $\boldsymbol{F}^{p}$ represents the crystallographic slip along the respective slip systems, and $\boldsymbol{F}^{*}$ represents the elastic deformation and rigid body rotation.

The spatial gradient of velocity $\boldsymbol{L}$ can be written as

$$\boldsymbol{L} = \dot{\boldsymbol{F}}\boldsymbol{F}^{-1} = \boldsymbol{L}^{*} + \boldsymbol{L}^{p}, \tag{5}$$

where

$$\boldsymbol{L}^{*} = \dot{\boldsymbol{F}}^{*}\boldsymbol{F}^{*-1},\ \boldsymbol{L}^{p} = \boldsymbol{F}^{*}(\dot{\boldsymbol{F}}^{p}\boldsymbol{F}^{p-1})\boldsymbol{F}^{*-1} \tag{6}$$

Breaking the velocity gradient down into the symmetric part leads to the elastic and plastic strain-rates $\boldsymbol{D}^{*}$ and $\boldsymbol{D}^{p}$, while the antisymmetric part leads to the plastic spin $\boldsymbol{W}^{p}$, and the spin $\boldsymbol{W}^{*}$ associated with the rigid lattice rotation

$$\boldsymbol{D} = \boldsymbol{D}^{*} + \boldsymbol{D}^{p},\ \boldsymbol{W} = \boldsymbol{W}^{*} + \boldsymbol{W}^{p} \tag{7}$$

The vectors $\boldsymbol{s}_{(\alpha)}$ and $\boldsymbol{m}_{(\alpha)}$, which have index α that ranges from one to the total number of slip system (the brackets indicate that it is not a tensor index), are the lattice vectors that distort and rotate by

$$\boldsymbol{s}^{*}_{(\alpha)} = \boldsymbol{F}^{*}\boldsymbol{s}_{(\alpha)},\ \boldsymbol{m}^{*}_{(\alpha)} = \boldsymbol{m}_{(\alpha)}\boldsymbol{F}^{*\text{-}1} \tag{8}$$

By using the symmetric tensor $\boldsymbol{P}_{(\alpha)}$ and skew-symmetric tensor $\boldsymbol{W}_{(\alpha)}$ as follows for each slip system α,

$$\boldsymbol{P}_{(\alpha)} = \frac{1}{2}\left[\boldsymbol{s}^{*}_{(\alpha)} \otimes \boldsymbol{m}^{*}_{(\alpha)} + \boldsymbol{m}^{*}_{(\alpha)} \otimes \boldsymbol{s}^{*}_{(\alpha)}\right] \tag{9}$$

$$\boldsymbol{W}_{(\alpha)} = \frac{1}{2}\left[\boldsymbol{s}^{*}_{(\alpha)} \otimes \boldsymbol{m}^{*}_{(\alpha)} - \boldsymbol{m}^{*}_{(\alpha)} \otimes \boldsymbol{s}^{*}_{(\alpha)}\right], \tag{10}$$

the plastic strain-rate $\boldsymbol{D}^p$ and spin $\boldsymbol{W}^p$ can be written as

$$\boldsymbol{D}^p = \sum_{\alpha} \boldsymbol{P}_{(\alpha)} \dot{\gamma}_{(\alpha)}, \quad \boldsymbol{W}^p = \sum_{\alpha} \boldsymbol{W}_{(\alpha)} \dot{\gamma}_{(\alpha)} \tag{11}$$

where $\dot{\gamma}_{(\alpha)}$ is the rate of shear on the slip system α.

The elastic constitutive equation for a crystal is specified by

$$\overset{\nabla}{\boldsymbol{\tau}}^* = \dot{\boldsymbol{\tau}} - \boldsymbol{W}^* \boldsymbol{\tau} + \boldsymbol{\tau} \boldsymbol{W}^* = \mathbb{L}\, \boldsymbol{D}^* \tag{12}$$

where $\overset{\nabla}{\boldsymbol{\tau}}^*$ is the Jaumann rate of the Kirchhoff stress tensor $\boldsymbol{\tau}$ based on the lattice rotations, and $\mathbb{L}$ is the tensor of the elastic moduli. This elastic moduli tensor is based on the anisotropic elastic constants of the crystal structure and contains cubic symmetry due to the symmetry of the FCC structure. The work presented by Asaro and Needleman [1985] used a rate tangent formulation which requires the use of the elastic visco-plastic moduli; however, the explicit formulation used here makes use of its small time step to allow the simplification of just using the elastic moduli.

To express the constitutive equation (12) in terms of the Jaumann rate $\overset{\nabla}{\boldsymbol{\sigma}}$ of the Cauchy stress $\boldsymbol{\sigma} = det(\boldsymbol{F})^{-1} \boldsymbol{\tau}$ based on $\boldsymbol{W}$, a second-order tensor $\boldsymbol{R}_{(\alpha)}$ is introduced for each slip system as follows:

$$\boldsymbol{R}_{(\alpha)} = \mathbb{L}\, \boldsymbol{P}_{(\alpha)} + \boldsymbol{W}_{(\alpha)} \boldsymbol{\sigma} - \boldsymbol{\sigma} \boldsymbol{W}_{(\alpha)} \tag{13}$$

Using (7) – (11) and (13), the constitutive equation (12) can be rewritten in the form

$$\overset{\nabla}{\boldsymbol{\sigma}} = \mathbf{L}\,\boldsymbol{D} - \dot{\boldsymbol{\sigma}}^{0} - \boldsymbol{\sigma}\,\mathrm{tr}\boldsymbol{D} \tag{14}$$

where $\dot{\boldsymbol{\sigma}}^{0}$ is a viscoplastic type stress-rate defined by

$$\dot{\boldsymbol{\sigma}}^{0} = \sum_{\alpha} \boldsymbol{R}_{(\alpha)}\,\dot{\gamma}_{(\alpha)}. \tag{15}$$

The viscoplastic type stress-rate can be viewed as the stress that is expelled or "relaxed" by the plastic deformation. The viscoplastic type stress-rate is subtracted from the combination of elastic moduli tensor and the total strain rate, which would represent the stress increment caused by a completely elastic material. The slip rates $\dot{\gamma}$ used in equation (15) are calculated by the following power-law expression

$$\dot{\gamma}_{(\alpha)} = \dot{\gamma}_{(0)}\,\mathrm{sgn}\,\tau_{(\alpha)} \left| \frac{\tau_{(\alpha)}}{g_{(\alpha)}} \right|^{1/m} \tag{16}$$

Here $\dot{\gamma}_{(0)}$ is a reference shear rate assumed to be the same for all the slip systems, $\tau_{(\alpha)} = \boldsymbol{P}_{(\alpha)} : \boldsymbol{\sigma}$ is the resolved shear stress on slip system α after being distorted and rotated to its current configuration, $g_{(\alpha)}$ is its hardness, and m is the strain-rate sensitivity index. $g_{(\alpha)}$ represents the current strain-hardened state of all slip systems where each slip system is initially given a value of τ_0 and rises with the accumulation of slip on the respective slip systems by the hardening law

$$\dot{g}_{(\alpha)} = \sum_{\beta} h_{(\alpha\beta)} \left| \dot{\gamma}_{(\beta)} \right| \tag{17}$$

where $h_{(\alpha\beta)}$ are the hardening moduli that take the form

$$h_{(\alpha\beta)} = q_{(\alpha\beta)} h_{(\beta)} \text{ (no sum on } \beta) \tag{18}$$

where $h_{(\beta)}$ is a single slip hardening rate, and $q_{(\alpha\beta)}$ is the latent hardening matrix. Asaro and Needleman [1985] use the following latent hardening matrix for FCC crystals

$$q_{(\alpha\beta)} = \begin{bmatrix} A & qA & qA & qA \\ qA & A & qA & qA \\ qA & qA & A & qA \\ qA & qA & qA & A \end{bmatrix} \tag{19}$$

where q is the ratio of the latent hardening rate to self hardening rate, and A is a 3 x 3 unity matrix.

For the calculation of each $g_{(\alpha)}$, Asaro and Needleman [1985], among others, simply assume they depend on the accumulated sum γ_a of the slips; that is,

$$g_{(\alpha)} = g_{(\alpha)}(\gamma_a), \quad \gamma_a = \int_0^t \sum_{\alpha} |\dot{\gamma}_{(\alpha)}| dt \tag{20}$$

To calculate slip hardening, Peirce et al. [1982] take it to be a function of γ_a, the total slip on all of the systems:

$$h_{(\beta)} = h_0 \left(\frac{h_0 \gamma_a}{\tau_0 n} + 1 \right)^{(n-1)} \tag{21}$$

where h_0 is a hardening constant, n is the hardening exponent, and τ_0 is the critical resolved shear stress.

For each time step, once the elastic spin, $\boldsymbol{W}^*$, is known, the lattice can be rotated by updating the orientation matrix. The orientation matrix, $\boldsymbol{Q}$, rotates the crystal axis using the method of Raphanel et al. [2004].

$$\boldsymbol{Q}_{n+1} = e^{\boldsymbol{W}^*_{\Delta t}} \boldsymbol{Q}_n \tag{22}$$

exp ($\boldsymbol{W}^*\Delta t$) is obtained through the Euler-Rodrigues formula

$$e^{\boldsymbol{W}^*_{\Delta t}} = \boldsymbol{I} + \frac{\boldsymbol{sin}\ \boldsymbol{w}^* \Delta \boldsymbol{t}}{\boldsymbol{w}^*} \boldsymbol{W}^* + \frac{1 - \boldsymbol{cos}\ \boldsymbol{w}^* \Delta \boldsymbol{t}}{(\boldsymbol{w}^*)^2} \boldsymbol{W}^* \boldsymbol{W}^* \tag{23}$$

where $\boldsymbol{w}^* = \sqrt{\left(\boldsymbol{W}^*_{ij} \boldsymbol{W}^*_{ij}\right)/2}$.

As the orientation matrix is updated throughout deformation, the Euler angles ($\boldsymbol{\phi}_1, \boldsymbol{\phi}, \boldsymbol{\phi}_2$) in Bunge's notation are extracted and recorded for tracking purposes. These angles can be used to monitor the texture evolution during polycrystal simulations (Kocks et al., [2001]).

4. Research Results – Numerical Simulations of Instabilities and Localized Deformation

As mentioned earlier, the work will include a study of the impact of grain orientation on the surface roughness developed during bending, as well as a study of grain boundary characterization within crystal plasticity simulations. These two studies are presented in the following subsections.

4.1. Numerical Modelling of Surface Roughness During Bending

To revisit the problem statement, surface roughness on the outer bend surface of a hem is detrimental in various ways. Cosmetically, unpainted surfaces lose their mirror-like finish with added surface roughness. Conversely, painted surfaces can develop issues with primer adherence with added surface roughness. From a performance standpoint, fatigue resistance in materials declines with added surface roughness (Yue [2005]), while at extreme levels, surface roughness can trigger localization during forming operations (Becker [1998]).

A special case in the surface roughness of stamped metal panels, known as “roping,” is highly undesirable in automotive body panels. Surface roughness can be linked with a material’s crystallographic texture; in other words, changing the texture will change the resultant surface roughness (Dao and Li [2001]). Lefebvre et al. [2012] showed that surface anomalies depend strongly on neighbouring grains. The interaction between neighbouring grains not only included grains found on the sheet surface, but also included grains located below the surface of the sheet. This conclusion is consistent with the results of Guillotin et al. [2011]. The impact of this grain interaction has not been studied for bending loading conditions. Groche et al. [2010] and

Nygårds and Gudmundson [2004] discuss the impact of grain size on surface roughness; however, this study has chosen to focus on grain orientation effects.

Bending has been explored using isotropic material models (Lele and Anand [2009]) as well as anisotropic models (Lee et al., [2012]) to study a variety of phenomena such as spring back. However, in order to study surface roughness, a distribution of material properties is required to create localized non-uniform deformation. For this reason, a crystal plasticity theory-based constitutive model is used for this study.

Surface roughness studies during uniaxial tension have been performed with two-dimensional (2D) models (Becker [1998]), providing some understanding of the mechanisms responsible for their appearance. However, bending is a relatively more complicated loading condition. While 2D studies using shell elements to model a plane perpendicular to the bend axis have been used to simulate bending (Kuroda and Tvergaard [2004], Kuroda and Tvergaard [2007], Hu et al., [2010]), the capability of 2D models to represent accurately the state of strain and stress as well as to reveal the presence of banding is inadequate. Mattei et al. [2013a] performed an experimental study on the bending response of aluminum sheet. The results included a linking of surface roughness with localized surface strain; however, they did not give a microstructure based explanation of their observations.

This study investigates the surface roughness that develops during bending in FCC crystals. Five common orientations (texture components) found in aluminum sheets, Copper, Brass, Cube, Goss, and S1, are employed in the simulations. To investigate the effects of crystallographic orientation on the overall surface roughness (of the outer surface of the bent material), bending simulations are performed using both single crystals and polycrystals. First, the predictive capabilities of two-dimensional (2D) models are investigated by simulating plane

strain tension (for the top layer of the bend). The predicted surface profile obtained by the 2D model is then compared with the surface roughness predicted by the full 3D model. Simulations of surface roughness during bending of single crystals of different orientations using the 3D model are presented. A series of bending simulations with polycrystals containing an equal distribution of only two of the above orientations within the structure are performed, and the relative contributions of different orientations to the surface roughness are discussed. Following that, simulations of bending are performed in a polycrystal containing all five orientations, to gain insight into mitigating any surface roughness concerns during deformation of aluminum sheets undergoing bending mode of deformation. Finally, the effect of bend axis is examined by repeating the study using single crystals and ploycrystals containing two orientations, only updating the axis of the bend to be rotated 90 degrees within the plane of the sheet orientation.

The commercial Finite Element package LS-Dyna is used in this study. The constitutive model described in the previous section is implemented through a User Defined Material Subroutine (UMAT) so that each grain within a polycrystal is represented by multiple elements. Due to the computational demands of 3D crystal plasticity modeling, a volume element with periodic boundary conditions along the axis of the bend is employed. The so-called unit-cube contains 25x25x25 elements and is subjected to pure bending loading conditions (Figure 7) so that: the plane that represents the x=0 plane is fixed in the x direction, the plane that represents the x=25 plane is rotated to a total angle of 24° about the y-axis and the nodes on the x=25 plane are restricted in the normal direction of the plane as it rotates. All nodes on the y=0 plane are linked with their respective node on the y=25 plane and constrained to have no relative motion (periodic boundary conditions). The z=0 and z=25 planes are free to deform as the inner and

outer surfaces of the bend respectively. The angle of 24° is chosen as this is the largest bend possible before some orientation combinations start presenting simulation stability issues.

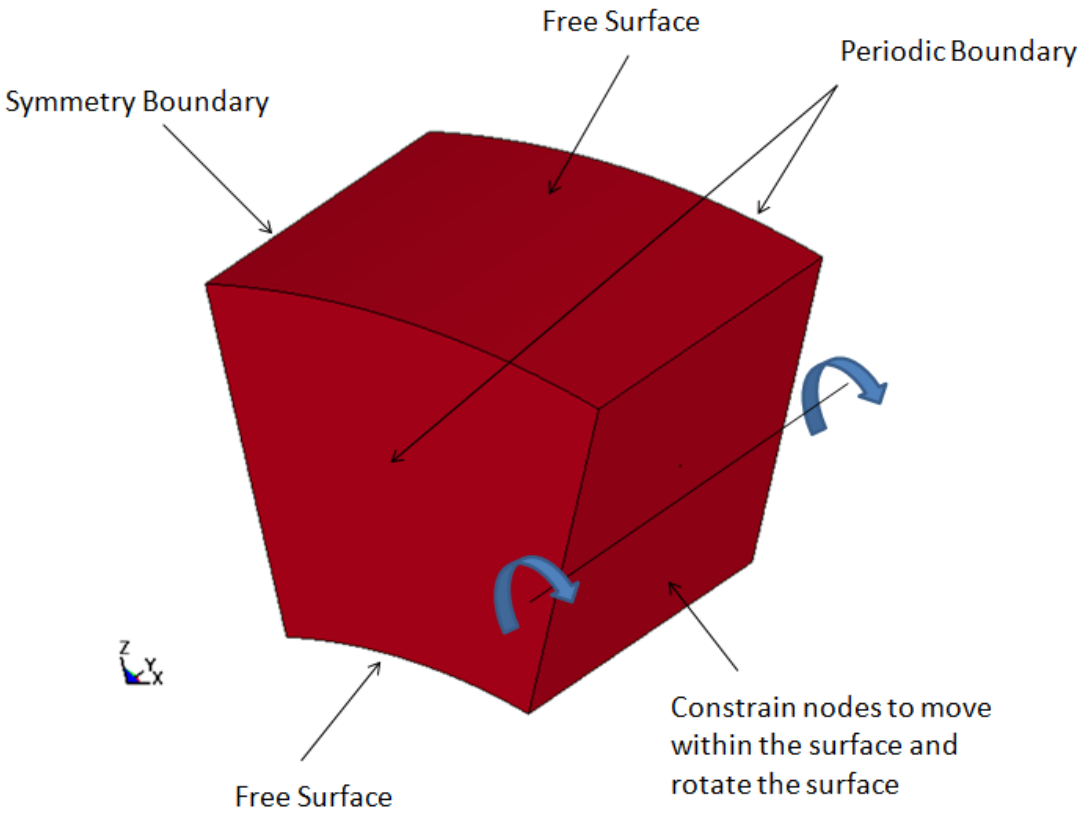

Figure 7: Boundary conditions for full 3D bending simulations.

The overall dimensions of the representative volume element (RVE) are 250 μm x 250 μm x 250 μm constructed with hexahedral, fully integrated, selective reduced solid elements (LS-DYNA element formulation #2). The bending load is applied at 0.4875 rad/ms. Since the model is using the explicit finite element formulation found within LS-DYNA, the rate at which the load is applied is an important factor for consideration. The rate of applied load used for this study has been identified by performing simulations using a power-law plasiticy model where the

rate of loading is varied and the fastest rate that still provided a uniform bending deformation without affecting the predicted stress distributions is chosen to ensure no inertial effects existed in the results.

The microstructure incorporated into the RVE is the only item varied between the simulations in the study. For single crystal simulations, the models are divided into 240 distinct sub-grains (Figure 8), each with a randomly assigned orientation that lies within 10 degrees of the single crystal orientation being studied. To achieve this random orientation, quaternions were employed to manipulate the ideal orientation being studied. When applying quaternions to 3D rotations, they can be described as using the first three components to define the axis of rotation, and the final component representing the angle of rotation about the defined axis. For this application, the ideal orientation was used as the starting point, then a completely random axis was defined, and a rotation angle randomly assigned between 0 and 10 degrees was used to rotate the ideal orientation (Figure 9). This results in an assigned orientation that must be within 10 degrees of the ideal orientation, but it could be deviating from the ideal orientation in any direction. The Euler angles for the five orientations are listed in Table 1.

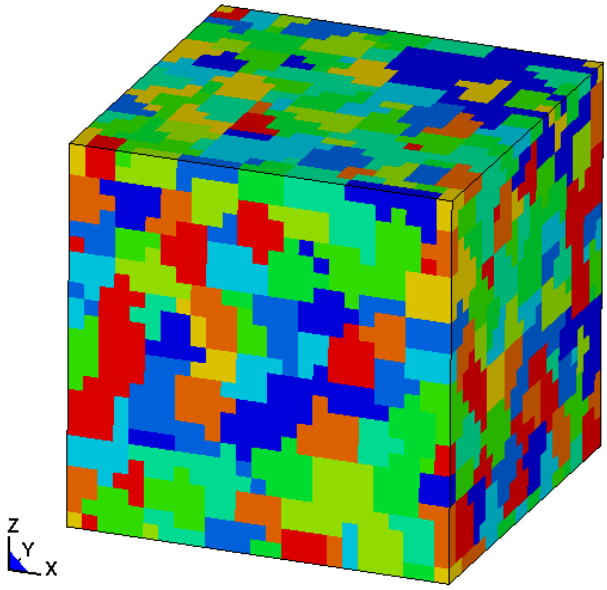

Figure 8: Sub-grain structure used for assigning the orientations to the single crystal and polycrystal models (colours are purely for visualization of sub-grains and do not indicate orientation, model size 250 μm x 250 μm x 250 μm).

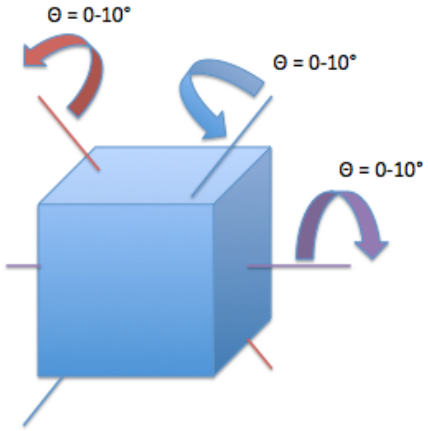

Figure 9: Visual representation of random axes with randomly assigned rotations from 0 to 10 degrees.

For the polycrystal models containing two orientations, the same approach as with the single crystal models is used; however, each of the 240 sub-grains is randomly assigned an orientation

that lies within 10 degrees of one of the two ideal orientations. It should be mentioned that the 120 sub-grains of one orientation are not structured in any assigned way and are randomly distributed within the microstructure. All ten possible combinations of the five texture components listed in Table 1 are simulated. A second set of polycrystals is created in the same fashion as the first, only instead of two orientations, all five orientations are included, and the relative amounts of each of the orientations are adjusted to test the conclusions drawn from the first set of polycrystals. This is explained in detail in the results section later.

Typical representative volume elements (RVEs) containing a single crystal structure and a polycrystal structure (two orientations) are presented in Figure 10. The colors in the figure are derived from the inverse pole figures (IPF). Pole figures from different regions and planes of the sample are compared to confirm that there are no local anomalies within the microstructure and that each sub region is representative of the overall microstructure for the case considered.

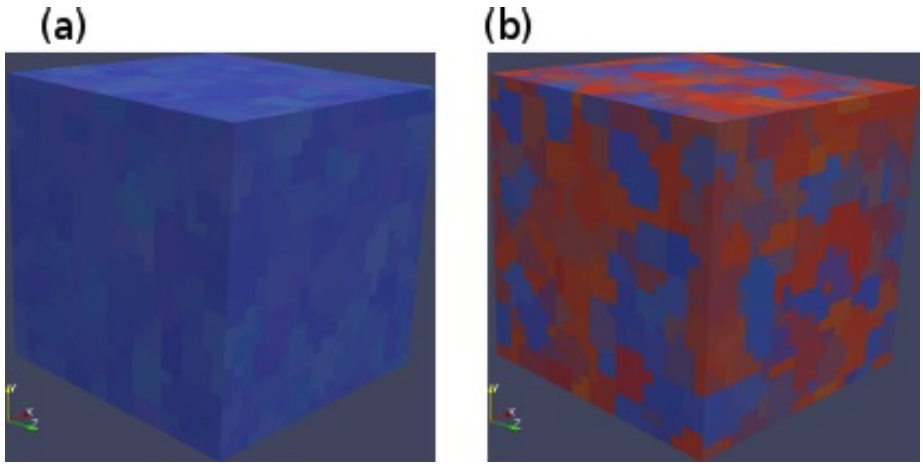

Figure 10: (a) Copper single texture, and (b) Cube-Copper polycrystal (red=cube, blue=copper, model size 250 μm x 250 μm x 250 μm).

The main limitation of this model is that the boundary conditions used elimitate the possibility of producing any deformation modes that exist at a larger scale than the model. Any

surface roughness phenomenon seen within the material that exists at a larger scale than the RVE cannot be captured. The model only considers the effects of orientation distribution within the microstructure. Among others, the model does not consider grain boundary effects, particle effects, or precipitate effects. The element formulation used in this study does exhibit the potential for shear locking in pure bending, however with 25 elements used in the thickness direction of the bend, the load being applied on the elements is a combination of bending and axial loading.

A second set of simulations is used where the top surface (z=25) of the 3D sample (Figure 8) is subjected to plane strain tension (as described in Figure 11). The boundary conditions applied in this model are, x=0 is fixed in the x direction, y=0 and y=25 are periodic in the y direction, and x=25 is pulled in the x direction. The elements are allowed to thin in the z direction, but are not able to move in the z direction. The material properties used in the simulations are listed in Table 2. The simulations employ the explicit solver in the commercial software LS-DYNA where no time scaling or mass scaling is used. The overall unit convention for the simulations is listed in Table 3.

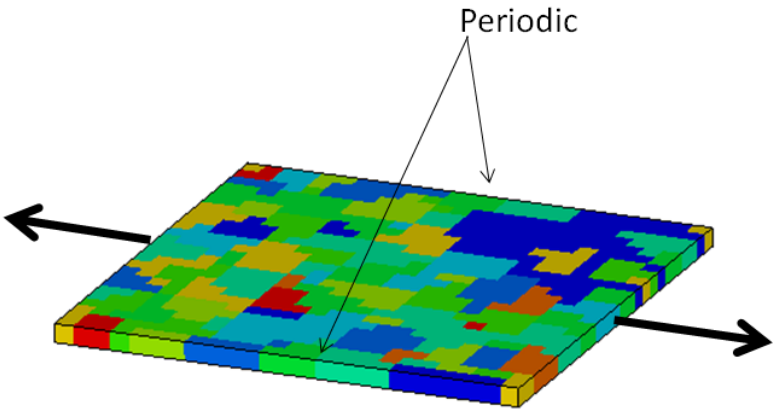

Figure 11: Top layer of Figure 8 used with 2D plane strain boundary conditions (model size 250 μm x 250 μm).

Table 2: Material properties used in surface roughness during bending study

Property	$\dot{\gamma}_{(0)}$	h_0	m	τ_0	n
Value	0.001 1/s	206 MPa	0.02	41.6 MPa	0.3

Table 3: Unit convention

Measurement	Time	Length	Mass	Force	Stress
Unit	μs	μm	ng	μN	MPa

4.1.1. Surface Roughness Quantification

Different techniques have been employed to measure surface roughness. The large impact of surface roughness on friction, lubrication and wear of contacting surfaces has led researchers to study and develop methods for quantifying surface roughness. Many of these methods involve the fraction of surface area above or below a given smooth plane parallel to the sample surface in question. Measuring surface roughness is commonly done by tracing a line on the surface of the material and recording the height of the surface along the scan line. By using multiple scan lines, the three-dimensional (3D) surface of the material is constructed (see example in Figure 12). Mathematically, calculating the second derivative of the plots created by the scan lines can provide an instantaneous quantitative measurement of the curvature of the surface line (Williams [2005]). By analyzing the spread of the second derivative, the overall surface roughness can be quantified. However, experimental surface scan data contain much artificial noise, which interferes with the second derivative calculation. To reduce the amount of noise in the experimental data, filters can be used with moderate success (Schouterden et al., [1996]). Another problem with second derivative calculations is that the data resolution can affect the results. For the study presented in this paper, second derivative calculations have been used due

to the ease of obtaining trace lines in finite element method (FEM) simulations where there is no experimental noise in the data and every simulation has the same mesh and, therefore, the same data resolution (Williams [2005]). An advantage to using a measurement of curvature for quantifying surface roughness is that it can be directly related to the radius of the surface grooves, and this information in turn helps predict stress concentrations due to geometrical imperfections. Along with the second derivative roughness quantification, a more commonly used root mean square (RMS) is used for comparison purposes.

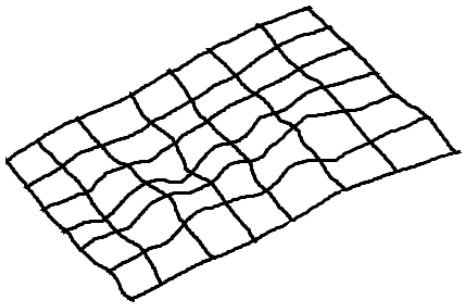

Figure 12: Example of surface roughness construction from multiple scan lines.

4.1.2. Banding

Imperfections in the form of banding (parallel ridges on the surface of the deformed specimen) can also be attributed to localization and failure. The ridges cause localization in the valleys and limit the formability of the material (Becker [1998]). The work of Lefebvre et al. [2012] showed that a crystal plasticity based model could be used to predict the banding effect in ferritic stainless steel sheets. Any insight on the factors that lead to banding can be used to help suppress the formation of banding and provide more versatility to the material being studied. The second derivative surface roughness values along perpendicular scan lines are used to quantify the banding in this study.

4.1.3. Surface Roughness Study Results

The simulations that have been described were performed. Since Lucachick and Sanchez [2013] found that surface roughness development was near linear during the first bend cycle of an experimental study analyzing the developed surface roughness in AA6022 sheets during repeated bending and unbending, the choice of how much to bend the samples became a decision based on reasonable computation time of the simulations. The "surface elevation contour plots" corresponding to a bend angle of 24° for the 3D model and tensile strain of 20% for the 2D model for three orientations are compared in Figure 13. The tensile strain value of 20% in the 2D layer corresponds to the tensile strain on the outer surface of the bent specimen. These plots are generated by normalizing the surface profiles (highest peak is 1 and lowest valley is 0). The bend angle and tensile strains are small compared to what one encounters in commercial hemming operations, but the mechanisms and conclusions would still provide insights for such large strain conditions. For the 3D bending simulations, the surface profiles are created by calculating the distance from the center of the bend (bend radius). Comparisons between the 2D and the 3D surface elevation contours show that there are significant differences between the 2D surface profiles and the 3D surface profiles (Figure 13). This observation is valid for all three sets of simulations and for both single crystals and polycrystals. Given that the 2D models contain only one layer of grains (the surface layer), the surface profiles obtained from 2D simulations are due to the effect of surface grains, while the surface profiles obtained from 3D simulations are the cumulative effect of surface grains as well as the internal grains.

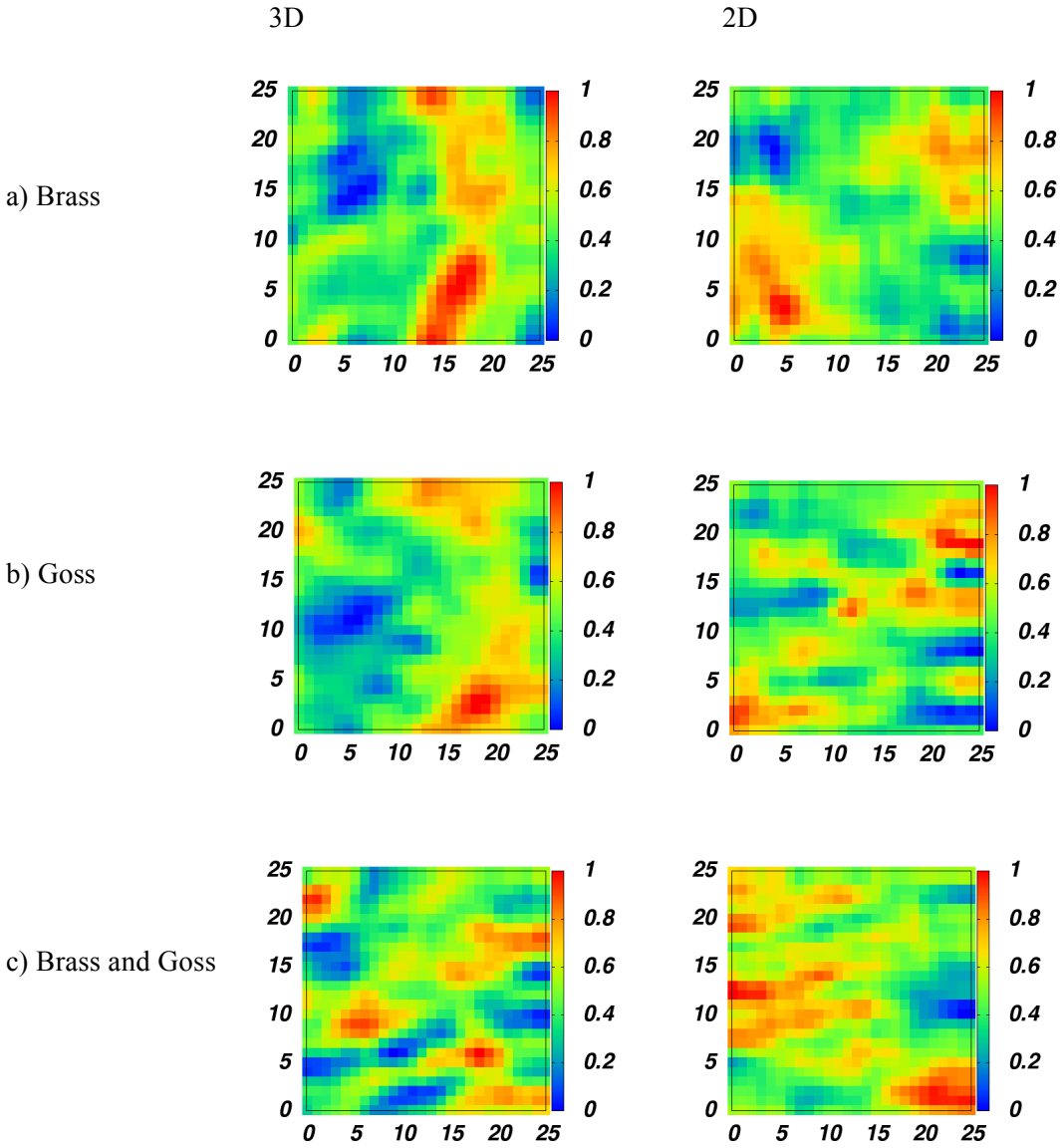

Figure 13: Comparing the normalized surface contour plots for both 3D and 2D simulations, (1 indicates highest peak while 0 indicates lowest valley) for a) Brass, b) Goss, and c) Brass and Goss (plot size 250 μm x 250 μm).

To further investigate the effect of subsurface grains, through thickness strain plots were created, and are presented in Figure 14. The strain plots in Figure 14 are fringe plots of the relative increase, or decrease, in effective strain that occurs when grain orientation is considered. To obtain the fringe plots shown in Figure 14, the effective strain distribution from an isotropic and

homogeneous material simulation was subtracted from the effective strain distribution from the Brass and Goss simulation. This allows the localization of strain due to grain orientation to be separated from the gradient in strain that exists in a bending operation. Two slices of the simulations are presented: Figure 14a) represents the slice through the 5th row of elements in the y-direction, while Figure 14b) represents the slice through the 7th row of elements. The results show that there exist locations of high strain (indicated by the arrows) below the surface of the bend which cause regions of elevated strain on the surface. Mattei et al. [2013a] have shown that surface roughness is directly related to surface strain localization. The predictions presented in Figure 13 as well as the observations from Figure 14 lead to the conclusion that surface roughness during bending cannot be accurately predicted with a 2D model. The underlying grains (below the surface) have a significant effect on the surface roughness and, thus, cannot be neglected in the simulations. Not only is the predicted surface roughness different in the simulated results, but also the locations of the high and low roughness zones are different. Note that these observations are in good agreement with the findings of Raabe et al. [2003].

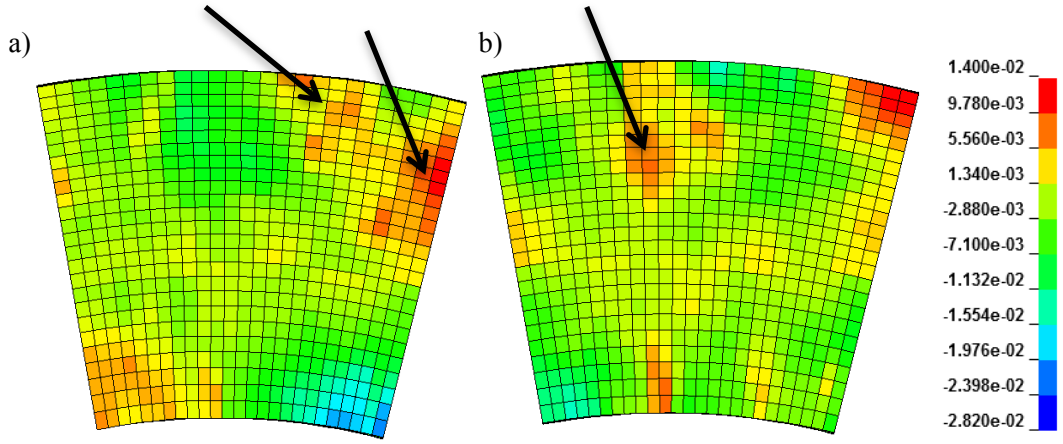

Figure 14: Fringe plot of relative increase or decrease in effective strain when grain orientation is considered for Brass and Goss (arrows indicate strain hotspots below the surface which affect the surface strain). a) represents the 5th row of elements in the y-direction, and b) represents the 7th row of elements in the y-direction (model size 250 µm x 250 µm x 250 µm).

3D models are employed in all the simulations to investigate the surface roughness in detail. An example of the deformed sample after 24° of bending predicted by the 3D model is presented in Figure 15a) for the polycrystal containing Goss and Brass orientations. The contrast and brightness in the rendering (during post-processing) of the surface is adjusted so that the surface roughness becomes visible. Figure 15b) shows the same simulation as a fringe plot of normalized surface roughness (1 is highest peak and 0 is lowest valley). The surface of the sample is not smooth and shows a banded structure, indicated by lines on Figure 15b). The general orientation of the bands is close to being along the arc of the bend (perpendicular to the bending axis).

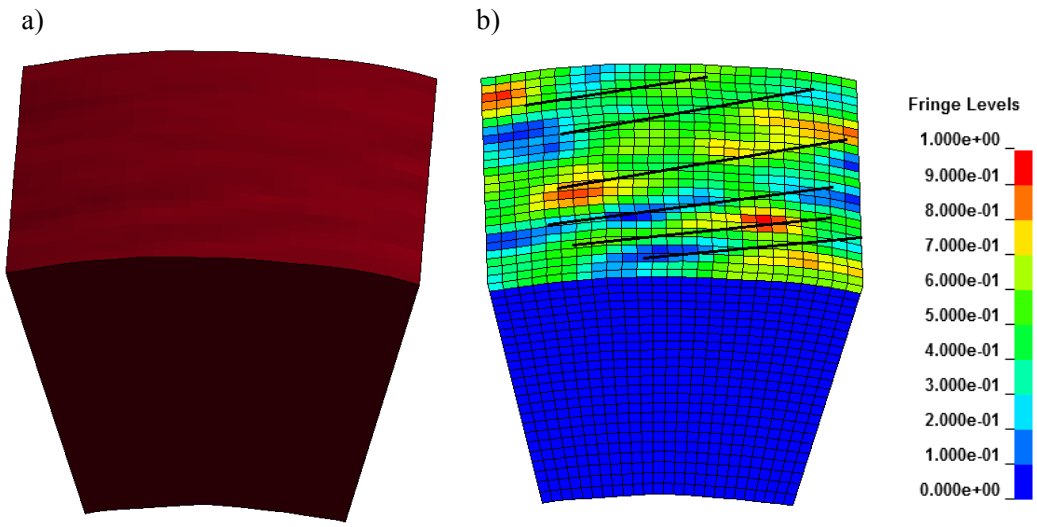

Figure 15: The final deformed bend for Brass and Goss, a) shaded model results, and b) fringe plot of normalized surface roughness (1 is highest peak and 0 is deepest valley) where lines indicate observed banding (model size 250 μm x 250 μm x 250 μm).

The surface roughness is quantified by calculating the standard deviation of the second derivative of multiple scan lines on the surface of the bend. Two sets of parallel scan lines are considered: one perpendicular to the bend axis, and one parallel to the bend axis (Figure 16). There were 25 scan lines in each set (one for each row of elements). The ratio of surface roughness (RSR) perpendicular to the bend axis and parallel to the bend axis is used to quantify

banding. This approach to quantifying the anisotropic phenomenon is most appropriate when the parallel ridges on the surface are in line with the circumference of the bend. Figure 15 shows that the parallel ridges are not perfectly aligned with the bend circumference. However, for the comparative purposes of this paper, the ratio mentioned above is considered adequate. Another quantification of surface roughness used in this research is the root mean square (RMS) of the distance between the instantaneous surface height and the average surface height (Turner and Miller [2007]). Since the deformed surface is the arc of a bend, the heights are considered to be the distance to the center of the circle, which contains the arc of the bend. The standard deviations (in two directions) as well as the RSR and the RMS are presented in Table 4 for each orientation. As expected, the polycrystal simulations produce higher surface roughness than the single crystals: 42 to 68 units for single crystals as opposed to 50 to 200 units for polycrystals (for parallel to Bend axis).

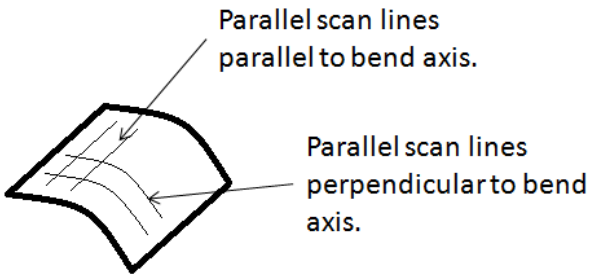

Figure 16: Directions of scan lines used for the second derivative calculations

Table 4: Standard deviation of the second derivative of the surface scan lines, Ratio, and RMS.

Orientation	Parallel to Bend Axis [μm^{-1} x10^{-5}]	Circumference of Bend	Ratio	RMS [μm]
Cube	43	12	3.58	0.120
Brass	68	53	1.28	0.217
Copper	61	35	1.76	0.143
Goss	42	26	1.61	0.127
S1	53	48	1.12	0.183
Brass and Cube	200	53	3.75	0.333
Brass and Goss	187	58	3.25	0.258
Brass and Copper	157	72	2.17	0.297
Brass and S1	138	112	1.24	0.340
S1 and Cube	97	52	1.84	0.279
S1 and Goss	92	63	1.46	0.275
S1 and Copper	91	62	1.45	0.226
Copper and Goss	74	44	1.69	0.208
Copper and Cube	71	28	2.58	0.222
Goss and Cube	50	18	2.79	0.096

Predictions with the numerical model show that the amount of surface roughness parallel to the bend axis is higher than the amount of surface roughness perpendicular to it (Table 4) in all orientations. The polycrystal simulations containing two orientations are listed in the table in order, from highest surface roughness to lowest surface roughness predicted by the 3D simulations. The sorting of the polycrystals is based on the surface roughness parallel to the bend axis; however, all three surface roughness quantifications give similar trends. Simulations show that all four polycrystals containing Brass have the highest surface roughness. These are followed by three polycrystal aggregates that contain S1, and two polycrystal aggregates that contain Copper. The polycrystal with the predicted lowest surface roughness contains Goss and Cube orientations. The order of the orientations with respect to their effect on surface roughness,

within a polycrystal aggregate, from highest to lowest is Brass, S1, Copper, Cube, and Goss, with the last two orientations very close. This finding is in good agreement with the results presented by Raabe et al. [2003].

Table 5: Surface roughness and grain boundary misorientation for each polycrystal containing two orientations.

Orientation	Surface Roughness [μm^{-1} x10^{-5}]	Misorientation [Degrees]
Brass and Cube	200	56.4
Brass and Goss	187	35
Brass and Copper	157	1.145
Brass and S1	138	20.5
S1 and Cube	97	41.8
S1 and Goss	92	32.5
S1 and Copper	91	20.7
Copper and Goss	74	35.4
Copper and Cube	71	56.1
Goss and Cube	50	45

Historically the cause of surface roughness is attributed either to the grain boundary misorientation or to the mismatch in the hardness of the neighboring grains (Raabe et al., 2003). Table 5 presents the misorientation for each polycrystal containing two orientations as well as the surface roughness value (parallel to the bend axis). The predictions demonstrate no obvious trends that could be used to relate misorientation to the predicted surface roughness, ruling out misorientation as a dominant factor behind surface roughness. Evolution of the local stress (simulations with single crystals) show that Brass, S1, and Copper have higher values of stress (effective stress) than Cube and Goss. However, the local stress distribution fails to explain why Brass produces more surface roughness than Copper or S1. These observations suggest that the evolution of local stress distribution is not the dominant factor affecting surface roughness.

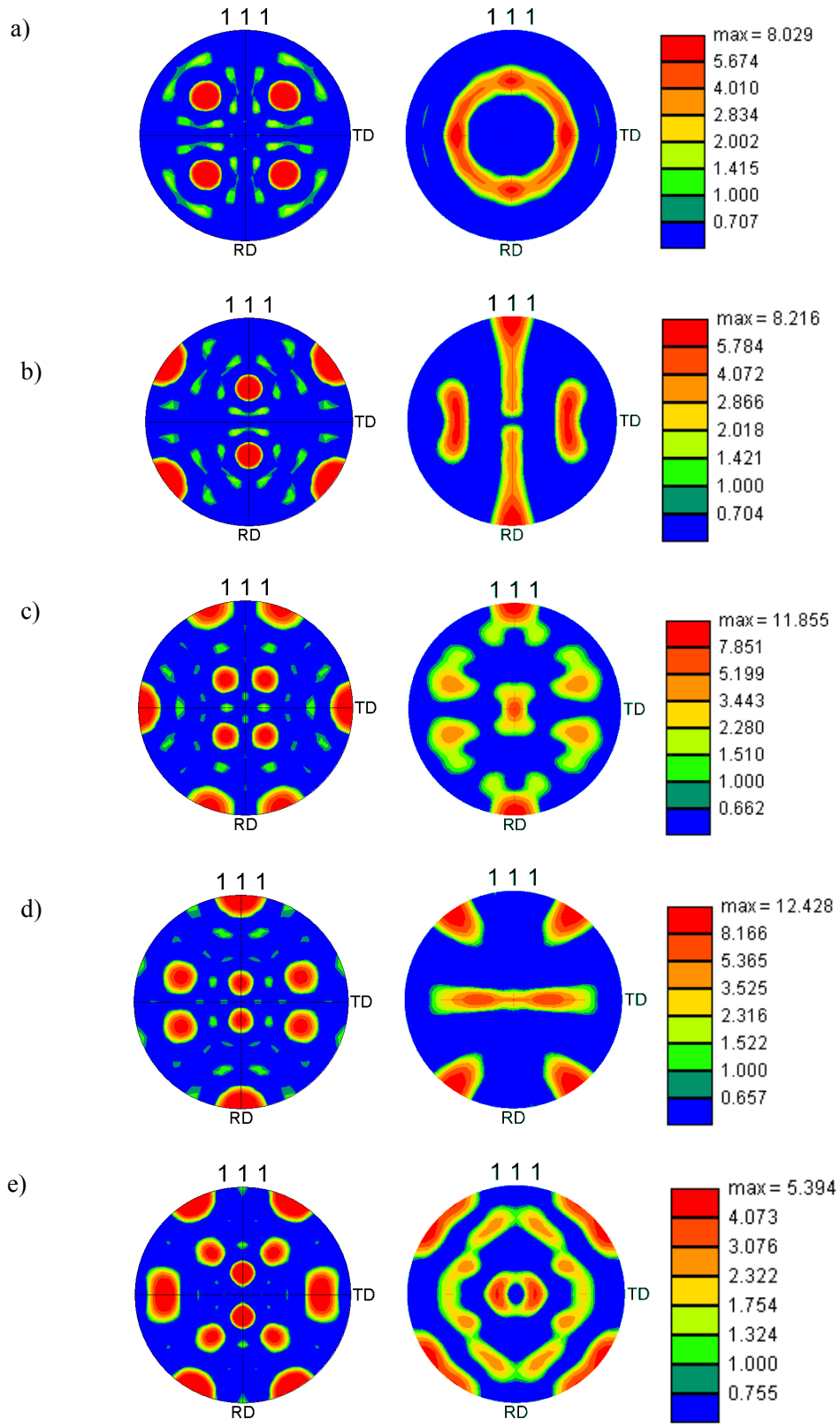

Figure 17: Initial and final (respectively) pole figures for the single crystal simulations, a) Cube, b) Goss, c) Brass, d) Copper, and e) S1.

Wittridge and Knutsen [1999] have experimentally demonstrated that spatial differences in texture, where R-component colonies are imbedded in a cube matrix, lead to differential straining, causing surface roughness. To investigate texture evolution, the texture evolution within each element (in the models) is calculated, and the rigid body rotation caused by the curvature of the bend is removed. This is the disorientation between initial orientation and final orientation (rotation) due solely to the deformation of the material. The initial and predicted evolved textures are presented in Figure 17a-e, where texture evolution is less significant in Brass and Copper than in Cube and Goss. To further quantify texture evolution, a histogram (obtained from simulations with the five single crystals) is presented in Figure 18. This plot shows the number, or frequency, of elements with certain disorientations as a function of the disorientation. A higher peak in the histogram indicates that there is less variation of crystal rotation within the simulation since the total number of elements is constant. It can be seen that the trend of surface roughness in a polycrystal from highest to lowest (Brass, S, Copper, Cube and Goss, with Cube and Goss being very close) corresponds to the height of the peaks in the histogram. Note that this could be interpreted as texture evolution stability, that is, Brass rotates the same amount regardless of slight variations in the initial orientations (± 10 degrees) and slight variations in stress and strain distributions within the sample, while Goss is more sensitive to these variations and shows a wide distribution of rotations within the sample. If these two orientations share a boundary, additional rotational (here, rotation implies texture rotation) incompatibility at the boundary occurs, resulting in an incompatibility in strain on either side of the grain boundary. In contrast, if the Brass grain is next to another Brass grain, which has a similar rotation, or next to an S1 grain, which can rotate by ~10° with a slightly larger spread, the likelihood of the two neighboring grains having a large incompatibility in rotation is smaller. In this case, the

rotational incompatibility will be lower and will, on average, result in smaller strain incompatibility. Thus the microstructure with more Brass-Cube/Goss neighbors might have larger roughness than the microstructure with Brass-Brass/S1 neighbors. Furthermore, the observation that the higher peaks occur at lower disorientations means that the rotations of Brass and S1 orientations are consistently low throughout the bent specimen.

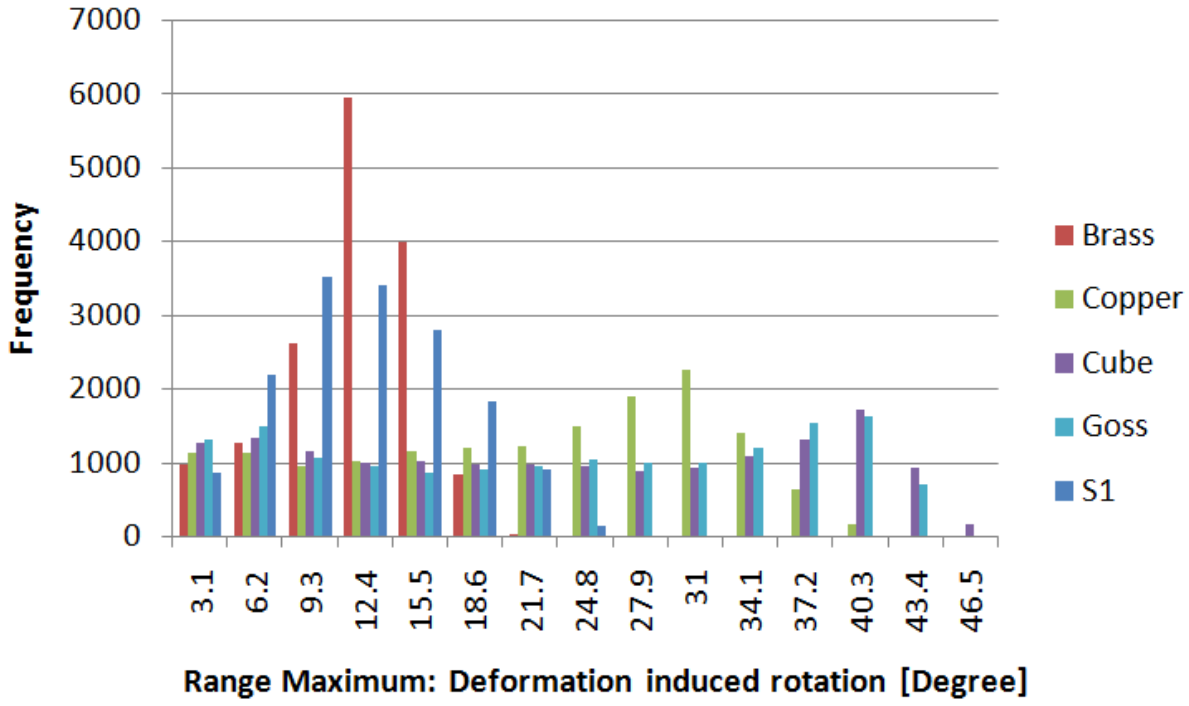

Figure 18: Frequency of deformation-induced rotation in the single crystal simulations.

Simulations show that the numerical models with the most pronounced banding are the ones where Brass is paired with Cube or Goss: the least strain-accommodating orientation and the most strain-accommodating orientation. Similarly, least banding is predicted in the models where Brass is paired with S1 (the two lowest strain-accommodating orientations).

The observations from the polycrystal simulations clearly indicate that Brass is an undesirable orientation to have during a bending operation. To validate this observation, the bending of three new polycrystal aggregates (with the above studied five orientations) was simulated. The orientation distribution functions (ODF) from the textures associated with these three microstructures are presented in Figure 19a-c. The three new polycrystal aggregates are designed so that the first one has all five orientations with the same volume fraction, while the second and the third aggregates have high Brass component (40% volume fraction) and no Brass component respectively (Figure 19a-c). The distributions of the five different orientations (volume fractions) as well as the predicted surface roughness are presented in Table 6. It can be seen that for all three surface roughness quantifications (second derivative along the bend axis, second derivative along the circumference of the bend, and the RMS), the addition of Brass increases the surface roughness, while the removal of Brass reduces the surface roughness.

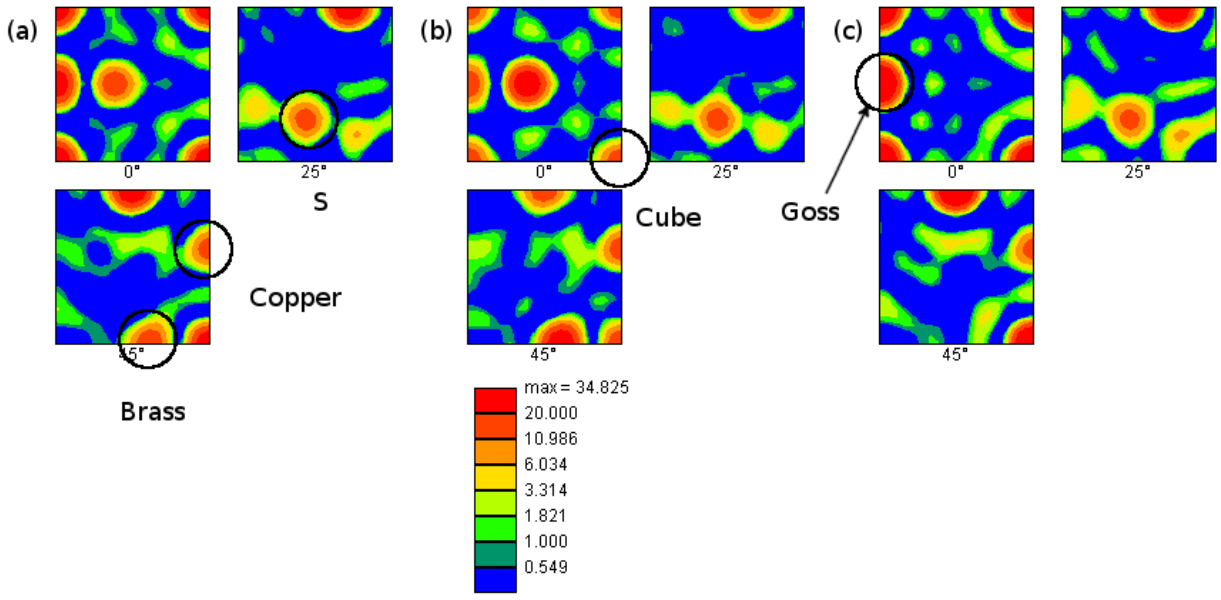

Figure 19: Textures for three microstructures with (a) all components having equal volume fraction, (b) with high Brass, and (c) without Brass.

Table 6: Polycrystal simulations varying the quantity of Brass and their surface roughness results.

	Equal	High Brass	No Brass
Cube	20%	10%	30%
Brass	20%	40%	0%
Copper	20%	20%	20%
Goss	20%	10%	30%
S1	20%	20%	20%
Roughness Parallel to Bend Axis [μm^{-1} $x10^{-5}$]	140	162	104
Roughness Along Circumference of Bend [μm^{-1} $x10^{-5}$]	59	73	47
Banding Ratio	2.37	2.22	2.21
RMS [μm]	0.321	0.375	0.218
Stress Triaxiality	3.5	3.7	2

The final set of simulations is performed to investigate the relationship between surface roughness and non-uniform deformation. Besides surface roughness being a serious problem for the appearance of the products, it can also be linked to the initiation of instabilities and localized deformation (Becker (1998)). It is well known that high stress triaxiality (effective stress over hydrostatic stress) within the material is directly linked with failure in aluminum alloys (Rossiter et al., [2011]). The simulated peak level of stress triaxiality is presented in Table 6, as well as the surface roughness results. Because the peak level of stress triaxiality rises throughout the bending simulations, the values are taken from the end of the simulations. The numerical analyses predict a direct relationship between surface roughness and high stress triaxiality; the peak level of stress triaxiality in the models rises with increased surface roughness. These results agree well with the analyses presented in Rossiter et al. (2011) where zones of high stress triaxiality are observed between soft and hard grains due to strain incompatibilities. As discussed,

the surface roughness that occurs during bending is caused by local strain incompatibilities, which also lead to zones of high stress triaxiality. Furthermore, the level of peak stress triaxiality rises slightly with the introduction of more Brass, but drops off significantly with the removal of Brass (Table 6). The observations suggest that the propensity of a material to develop surface roughness may be a predictor of its susceptibility to early crack nucleation during bending.

To complete this study, the effect of changing the axis of the bend was investigated by altering the bend axis. A way of visualizing this is to imagine that this is a physical experiment and that the sample is removed from the test fixture, rotated 90 degrees about the z-axis, and reinserted into the fixture. The surface roughness results of the polycrystals containing two orientations can be found in Table 7. The first observation that can be made is that the overall values of surface roughness are higher than the values found with the original loading direction. But without a doubt, the most surprising change is that the mixture of Cube and Goss changes from being the model with the least surface roughness to that with the highest surface roughness. This observation can be explained by combining the conclusions already drawn from this study – that a combination of hard and soft orientations produce enhanced surface roughness – as well as a result presented in Kuroda and Tvergaard [2007]. Kuroda and Tvergaard showed that when Goss is pulled along the x-axis, it acts as if it were identical to Cube, but when pulled along the y-axis, it becomes the hardest orientation. So when the axis of the bend is oriented in such a way that the majority of the tension (or compression) from the bend is aligned with the x-axis of the material (such as in the first loading orientation), there is no difference in hardness between the two orientations and, therefore, little produced surface roughness. But when the axis of the bend is orientated with the tension from the bend being along the y-axis, the pairing of Goss and Cube produces the largest difference in hardness and, therefore, the largest surface roughness. This

finding also agrees with work by Raabe et al. [2003], who report that the largest strain incompatibility was observed with Goss and Cube under tensile loading in the transverse direction. After moving Goss to the top of the list of orientations to cause surface roughness, the remaining orientations remain in the same order of influence on produced surface roughness, that is, Brass, S1, Copper, and finally Cube; however, this trend in the table is not quite as obvious as it is in the original loading. In an experimental study, Liao and Chen [2010] confirmed that tensile loading in the y-direction (similar to the second bending loading condition) produces larger surface roughness but also more inconsistent surface roughness development with respect to applied strain. Loading along the x-direction produced a clear linear relationship between applied strain and developed surface roughness, but this observation did not hold with the y-direction. Part of the lessening trend in the surface roughness table order may be due to this non-linear surface roughness development.

Table 7: Standard deviation of the second derivative of the surface scan lines with loading rotated by 90 degrees [μm^{-1} $x10^{-5}$] and their Ratio.

Orientation	Parallel to Bend Axis	Circumference of Bend	Ratio
Brass and Cube	124	69	1.80
Brass and Goss	183	96	1.91
Brass and Copper	105	79	1.33
Brass and S1	180	117	1.54
S1 and Cube	152	102	1.49
S1 and Goss	168	116	1.45
S1 and Copper	95	88	1.08
Copper and Goss	109	93	1.17
Copper and Cube	85	78	1.09
Goss and Cube	206	77	2.68

4.1.4. Surface Roughness Conclusions

In this study, the surface roughness developed in single crystals and polycrystals during bending is analyzed for five different orientations commonly found in aluminum alloys. The surface roughness is quantified by using the standard deviation of the second derivative of scan lines along the surface of the simulation. This approach is possible since there is no experimental noise in the data and all the data points are equally spaced. Banding is quantified by calculating the ratio of surface roughness parallel to the bend axis and perpendicular to the bend axis.

Simulations show that the texture, misorientation, and local stress state in the material can not be correlated with the surface roughness measured on the outer surface of the bend. However, the surface roughness is found to be directly related to the difference in the strain accommodating capabilities of the different orientations within a polycrystal aggregate. The order of the orientations from highest surface roughness to lowest surface roughness is Brass, S1, Copper, Cube, and Goss. Furthermore, the orientations causing the highest surface roughness are orientations that have low texture evolution during bending. In other words, the more stable orientations (during bending) lead to higher surface roughness during bending. Simulations of bending with polycrystals containing all five orientations predict that increasing and decreasing the Brass content of the material increases and decreases the surface roughness, respectively. Finally, banding is found to be most pronounced when Brass was mixed with Cube or Goss, and least pronounced when Brass was mixed with S1.

When the loading direction is rotated by 90 degrees about the z-axis, the major change in response is that Goss jumps from being the lowest on the surface roughness list to being the highest. This observation is consistent with observations made in tensile experiments and simulations found in the literature.

To produce an aluminum sheet that has increased bendability, avoiding Goss will allow the sheet to be bent in any direction and make it less suspect to anisotropy. Avoiding the presense brass will help increase the overall bendability.

4.2. Numerical Modelling of Grain Boundaries

The second study covered in this work explores the use of crystal plasticity theory-based numerical models for characterising what occurs at grain boundaries. Crystal Plasticity Theory is the study of plastic yielding by considering the arrangement of the atoms within metallic materials. Crystal plasticity has been shown to predict very accurately the anisotropic behaviour of single crystals (for example: Izadbakhsh et al., [2010]). A set of material parameters can be fit to a single crystal orientation, which in turn can be used to predict the response of other orientations. However, the material parameters obtained from a single crystal need to be adjusted to predict accurately the polycrystal results. One major assumption for this difference is that the grain boundaries are responsible for the difference between polycrystal results and single crystal results. The main focus of this research is to develop different methods of modelling the grain boundaries and to determine what methods of modelling the grain boundaries are the most realistic – that is, allow the polycrystal material parameters to more closely match the single crystal material parameters.

To revisit some of the points covered in the introduction, the physical structure of a grain boundary is a planar interface; however, the grain boundary-affected region exists as a volume of material near the grain boundary. Whether the boundary should be modelled as special 3D elements or whether it should be left as a planar interface in the models is a question of ongoing research. Grain boundaries are not smooth curves, but rough, jagged interfaces. Capturing the rough features of the grain boundaries can require many small elements that can reduce a

simulation's efficiency. Modelling the grain boundaries with larger elements has the potential to increase a model's efficiency; however, the accuracy of the simulations can be reduced. According to the literature, most of the existing crystal plasticity models do not have any special calculation or consideration at the grain boundary; they merely represent the boundary by having two neighbouring elements with different orientations (Li et al., [2004], Delannay et al., [2006], Erinosho et al., [2013]). Some models have been proposed in which cohesive elements have been placed along the grain boundaries to account for small amounts of grain boundary slip, fracture, and grain boundary accommodation (Sfantos and Aliabadi [2006]).

The mismatch of lattice structure at the grain boundary impedes dislocation motion, causing dislocation pileup. This dislocation pileup can affect the material properties surrounding the grain boundary. For this reason, some crystal plasticity models attempting to model grain boundaries have 3D elements to model the boundary as a region with thickness equal to the grain boundary-affected zone. This is the approach taken in this research, and the grain boundary-affected zone will be considered to be 20 μm thick (Siamoto [2011] (personal communication)).

Modelling the rough, jagged surfaces of grain boundaries can potentially require very small elements when compared to the elements size within the grains. This requirement can cause large, inefficient meshes and small time step sizes. It is still unclear what the effect of these fine geometrical details is on the overall material response. If these details can be removed and the grain boundary smoothed to a surface with large radius of curvature, then much larger elements can be used to model the microstructure. The coarse mesh would increase the minimum time step size of the simulation and reduce the number of elements required for the model. An understanding of the impact of the fine geometrical details is needed to either allow the complete removal of the features or allow coarser elements to be used with a modification put in place to

account for the smoothing operation. Either of these two options would allow for substantial improvement of the analysis capabilities of crystal plasticity-based FEA.

Surface roughness on the outer face of a hem is very important from an aesthetics as well as a formability standpoint – the fatigue resistance decreases with added surface roughness (Yue, [2005]). The same second derivative surface roughness quantification used in the previous study can be used in this study due to the ease of regulating data resolution as well as the lack of experimental noise. For this work, the surface roughness developed during the bending models will be compared between the different modelling approaches, and discussed.

4.2.1. Experimental Data

Two sets of experimental data are used in this research. The first is the single crystal aluminum data found in Inoko et al. [2010], and is used to calibrate the single crystal constitutive response of the crystal plasticity material model. The second set is the polycrystal data previously presented in Zhu et al. [2011].

For the single crystal data, Inoko et al. [2010] presents an extensive study of single crystal aluminum deformation mechanisms. In this study, tensile loading tests on single crystals are conducted, and the direction of the loading axis is reported. Figure 20 presents the curves reported for the <001>, <111>, and <112> directions. These are the curves that will be used to obtain the single crystal material fit discussed in Section 4.2.3.1.

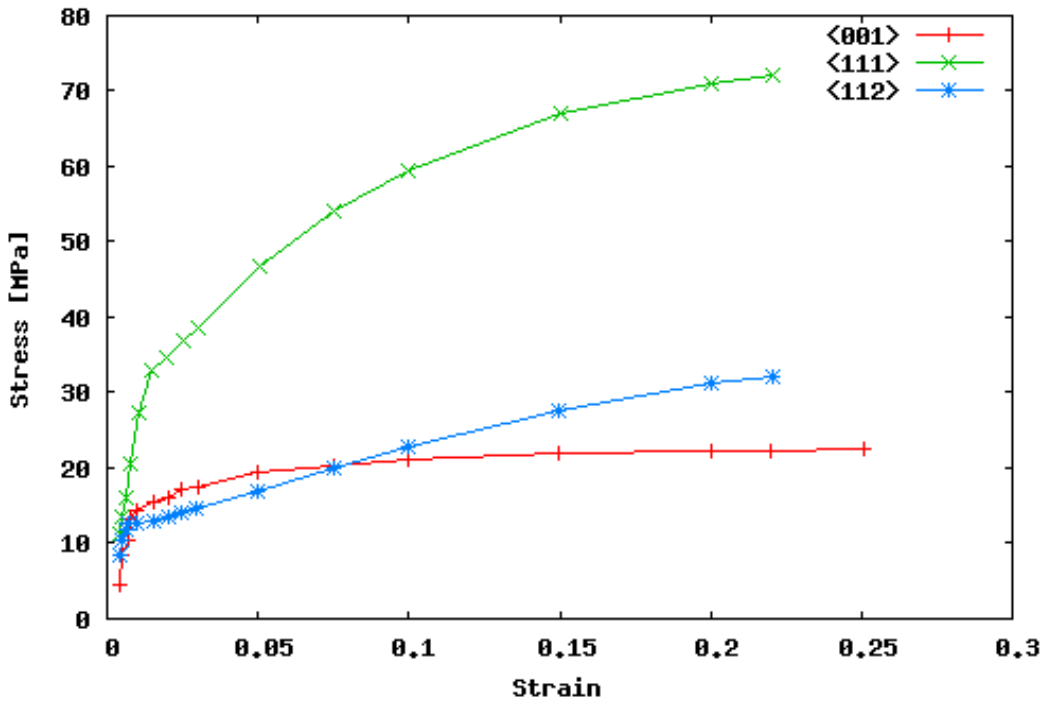

Figure 20: Single crystal tensile response for three different loading axes (Inoko et al., [2010]).

For the polycrystal data, Zhu et al. [2011] present some unique work in which a 6 mm x 5 mm large-grained aluminum sample with two layers of columnar grains is created, and studied extensively. The advantage of the columnar structure is that non-destructive 2D EBSD scans can be used to establish the 3D material microstructure. Since the sample consists of two layers, a scan from each side of the sheet is required, and the structure can be made with the assumption that the two layers interface at the center of the sheet thickness. The material can then be subjected to destructive tests, such as uniaxial tension tests, while recording strain distributions with DIC methods. This allows direct comparison with simulations using initial microstructure input and experimental results. The measured microstructure can be seen in Figure 21 a) and b); note that the inverse pole figures presented here are the ND pole figures, while the figures presented in Zhu et al. [2011] are RD pole figures.

a)

b)

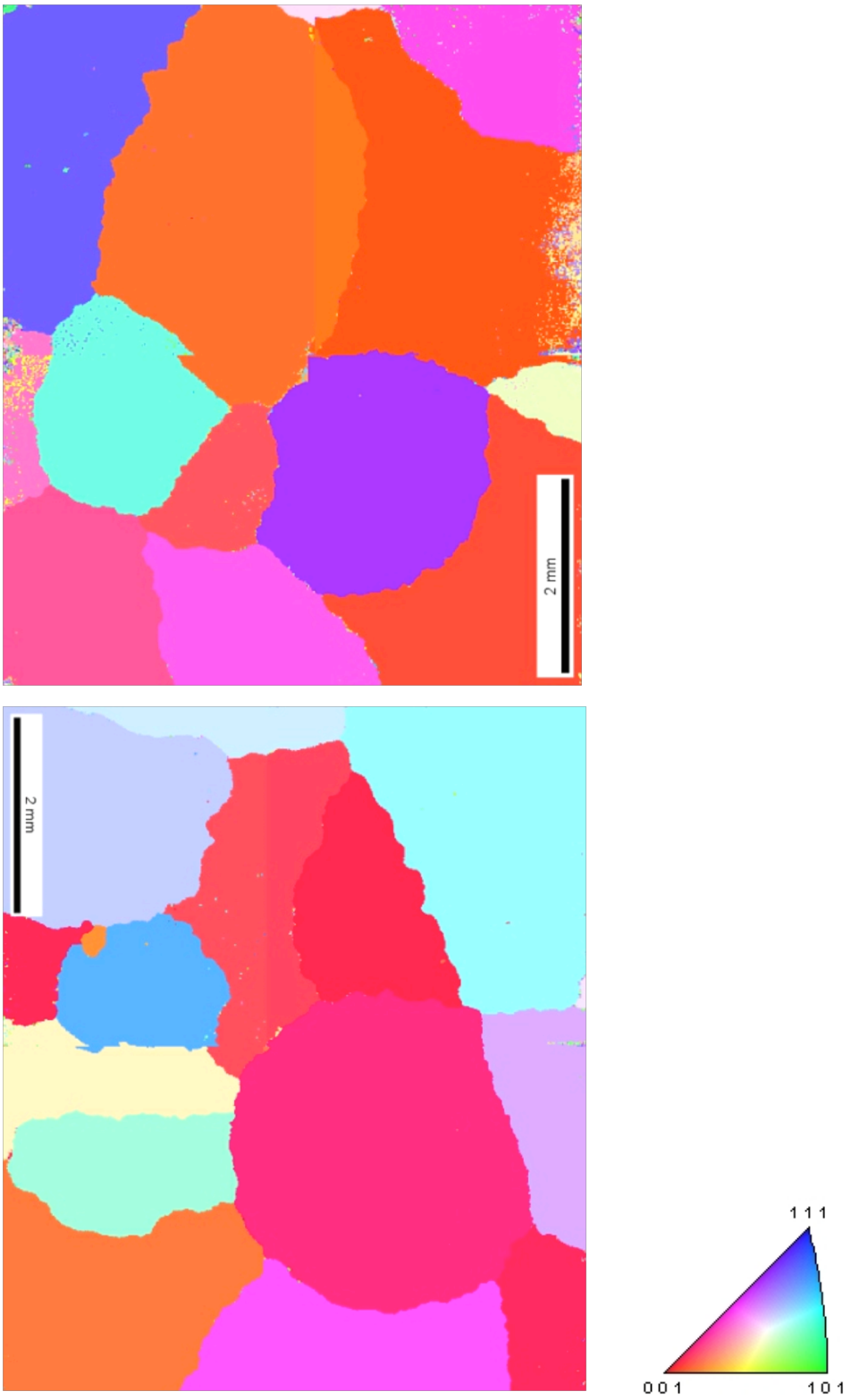

Figure 21: Inverse pole figure for large-grained aluminum polycrystal, a) Side A, and b) Side B (Zhu et al., [2011]).

The DIC data was recorded as outlined in Zhu et al. [2011]. Images were recorded every 2 s during the tensile test (1mm/min crosshead speed, 6 mm gauge length). The speckle pattern was processed using the Aramis software package, and a regular grid of nodes was established, as well as nodal movements throughout the test. As the DIC data is very sensitive to image quality, some regions of the images are processed with a lesser degree of confidence than is the bulk of the image. These regions of bad data are filtered out and removed. For that reason, the data was inspected, and the point of strain that indicated the least amount of missed data was chosen for the analysis presented in this study. The point with an applied strain of 14% can be seen in Figure 22 in the form of an effective strain contour map.

a)

b)

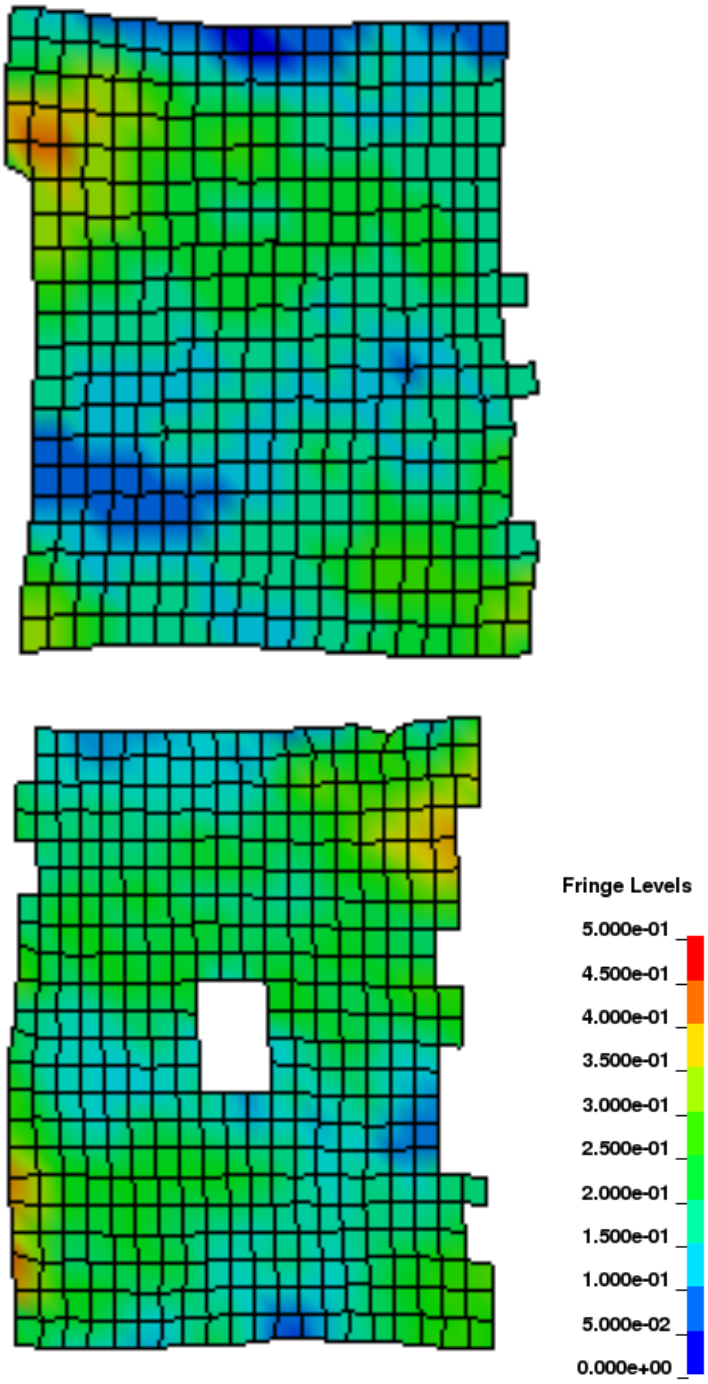

Figure 22: Fringe plots of DIC measured effective strain maps for both sides of the specimen's gauge at 14% strain (sample size 6 mmx 5 mm).

In addition to the DIC data, the overall stress versus strain curve from the tensile test was recorded as well, and will be used to calibrate the model along with single crystal data. The measured stress versus strain curve is shown in Figure 23.

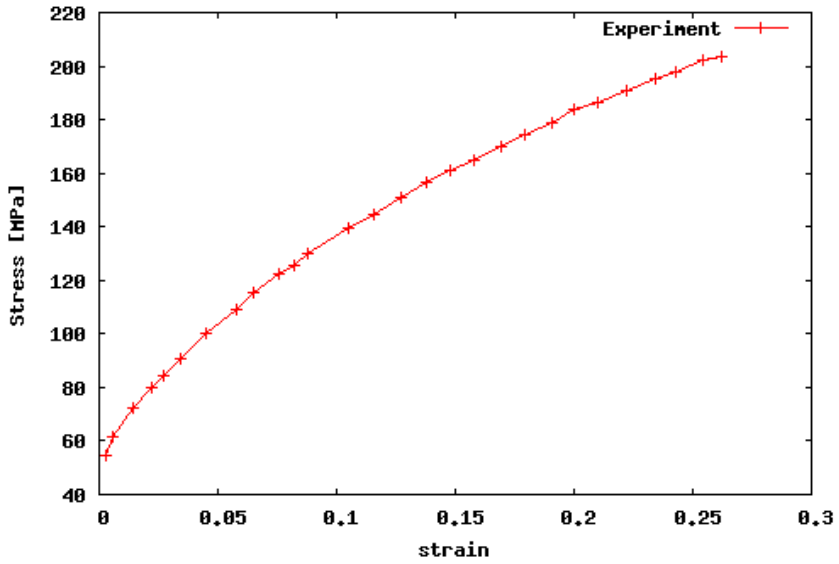

Figure 23: Experimentally measured stress vs. strain response (Zhu et al., [2011]).

4.2.2. Numerical Data

In this section the development of the numerical model is discussed. The material constitutive model is the model presented early, and only deviations from the description presented earlier are presented here. The development of the finite element meshes of the polycrystal microstructure from Section 4.2.1 is presented as well.

4.2.2.1. Constitutive Model Modification

The simulations performed for this study use a rate dependent crystal plasticity theory formulated by Asaro and Needleman [1985] implemented into the commercial FEM software LS-DYNA. The complete constitutive model can be found in Section 3. The only modification made to the constitutive model is the slip hardening model used for the single crystal material fit.

The hardening model was varied with a variety of different hardening models, and it was discovered that the best fit could be achieved with one found in Harren et al. [1989]:

$$h_{(\beta)} = h_s + (h_o - h_s)\,\mathrm{sech}^2\left\{\left(\frac{h_o - h_s}{\tau_s - \tau_o}\right)\gamma_a\right\}, \tag{24}$$

where h_o is the system's initial hardening rate, h_s is the system's asymptotic hardening rate, τ_o is the critical resolved shear stress of the system, τ_s is the saturation value of the shear stress, and γ_a is the accumulated slip. The reason for implementing this hardening law is that the single crystal experimental data found in Figure 18 displays a saturation hardening characteristic for the <001> direction, which is not obtainable using the power law hardening model used previously. The model that does not contain grain boundary zones and single crystal material parameters still uses the original power law hardening model from Pierce et al. [1982], as described in Section 3, in order to be consistent with our previous modelling approach, and becaue it produces a good fit.

For the grain boundary zones, a simple linear piecewise material constitutive model (LS-DYNA MAT24) is used. The stress versus strain curve that is provided to the model is the experimentally measured stress versus strain curve obtained from the tensile test modified by a scalar, which will be discussed in Section 4.2.3.2.

4.2.2.2. Finite Element Mesh Generation

There are two main models for this work, both of them derived from Sample A found in Zhu et al. [2011]. These will be the polycrystal material models used to study the effect of modelling grain boundary zones. The first polycrystal model has the material shown in Figure 21 meshed without grain boundary zones, and the second has the grain boundaries modelled as ~20 μm wide zones that map along the grain boundaries. The two meshes are identical in all other

aspects. To create these meshes, a series of programs were created to process the 2D EBSD data as follows.

The data was processed to clean any bad data points and assign each pixel to a grain number (Figure 24). The pixels were processed, each pair of neighbouring pixels that belonged to two different grains was identified, and a node representing a point on a grain boundary was placed between them (Figure 25). The pixels were processed again, whereby every possible region of 2x2 square pixels was analyzed, any region containing pixels from three or more grains were identified, and a node representing a triple point was placed in the center (Figure 26). A series of bar elements was then created where each string of elements started at a triple point and connected all the boundary nodes along a boundary until it reached the triple point on the opposite end of the boundary (Figure 27). The end result was a map of the grain boundaries consisting of 1D bar elements, a sample of which appears in Figure 28. Since the sample consists of two layers of grains, the procedure for mapping the boundaries was conducted for both sides and then overlaid to produce a single map that contained outlines of all the grain boundaries on both layers of grains. The reason for combining the two layers of grain boundaries onto a single mesh is that when the final mesh is created, the elements and nodes at the interface between the two layers of grains need to match completely to allow a conforming mesh.

3	3	3	3	3
7	7	3	3	14
7	7	3	3	14
7	7	14	14	14
7	7	14	14	14
7	7	14	14	14
7	7	14	14	14

Figure 24: Sample data where pixels are assigned grain numbers.

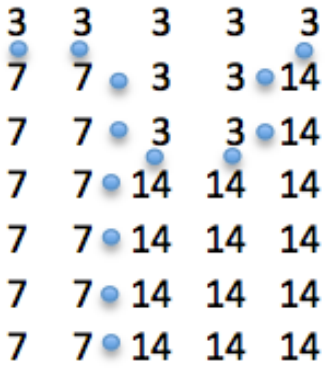

Figure 25: Sample data where nodes are placed on grain boundaries.

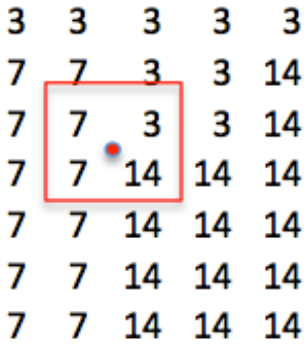

Figure 26: Sample data where nodes are placed at triple points.

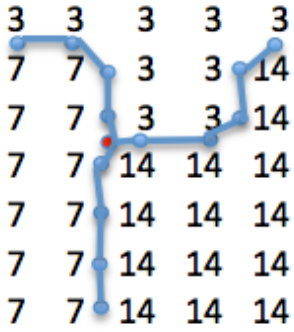

Figure 27: Sample data where bar elements are placed along grain boundaries.

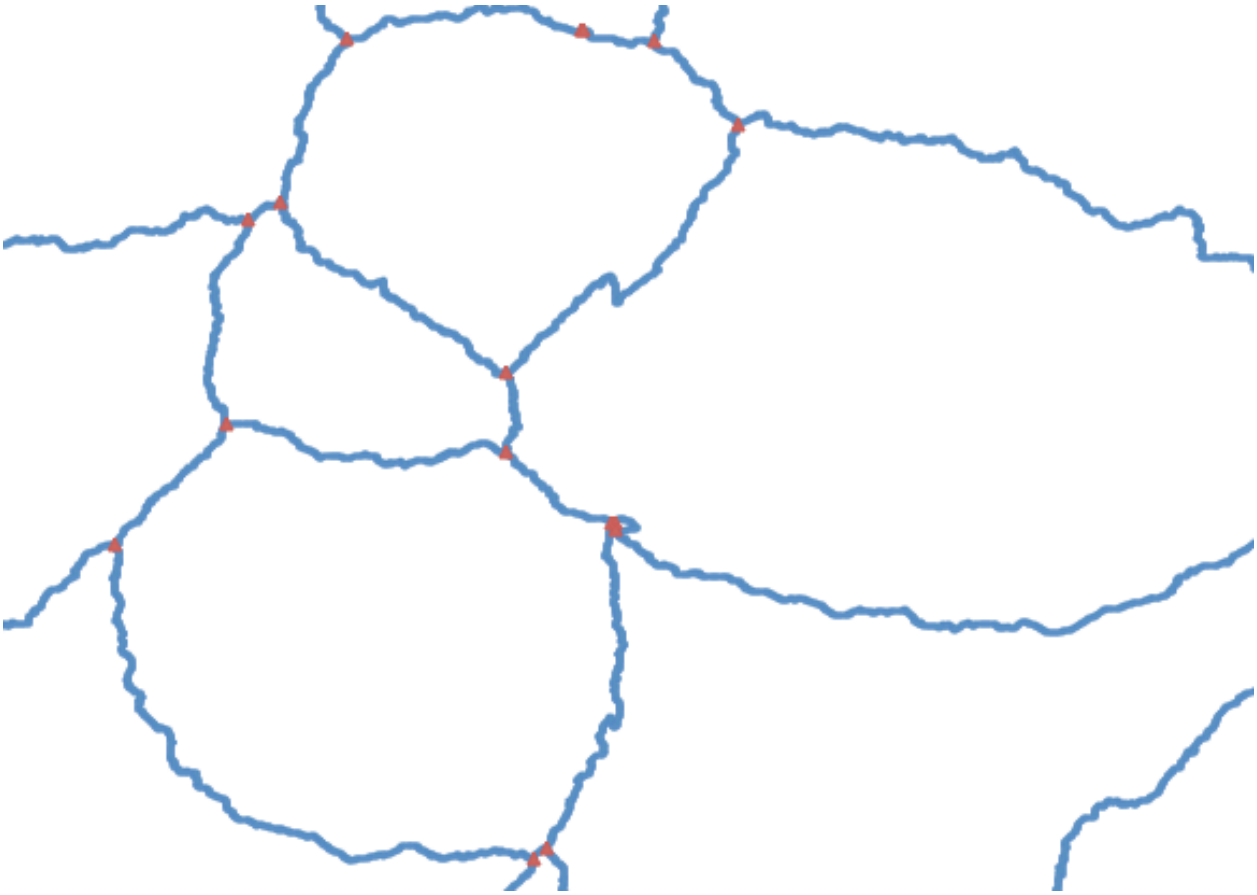

Figure 28: Grain boundary map for a portion of the data.

Once the system of bar elements representing the grain boundaries was completed, the 2D region within each grain was meshed with shell elements. At this point, the addition of grain boundary zones was performed and the two distinct meshes were produced separately. For the mesh, which includes the grain boundary zone, the nodes that represent the grain boundary nodes were duplicated, separated by a distance of ~20 μm, and a quadrilateral shell element was placed in the gap. This resulted in triangular holes in the mesh at each triple point, which were filled manually with triangular elements (Figure 29).

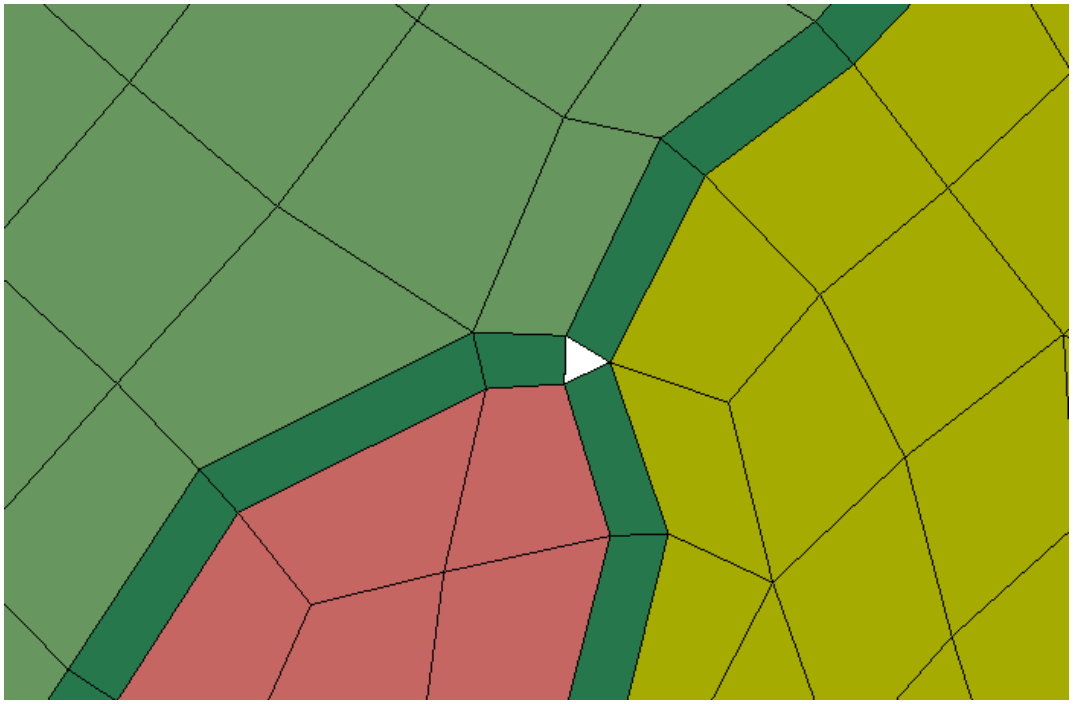

Figure 29: Hole located at triple point caused by creating grain boundary zones.

Both meshes were then extruded, with 9 layers of elements, to the thickness of the sample. The regions representing each grain were combined and assigned to their own part designation, and the orientations of the grains were assigned to the mesh. The grain boundary zone elements for the whole structure were combined onto a single part designation, which was assigned a phenomenological material model. The final mesh for the grain structure can be seen in Figure 30 for the model without grain boundaries, and in Figure 31 for the model with grain boundaries. Both meshes are virtually identical except for the addition of the narrow grain boundary zone.

The mesh primarily consists of hexahedral elements with the occasional wedge element (for example, at each triple point). The boundaries created are columnar in nature due to the assumption that the surface EBSD scans represent a constant grain pattern throughout the thickness of the specimen. This an approximation of the real material as it is expected that the

real boundaries would not be perfectly columnar. As with the previous study the elements use LS-DYNA element formulation #2. The model does not include any form of particle effects.

The unit convention used for the models can be found in Table 8.

Table 8: Unit convention for grain boundary study.

Measurement	Time	Length	Mass	Force	Stress
Unit	μs	μm	ng	μN	MPa

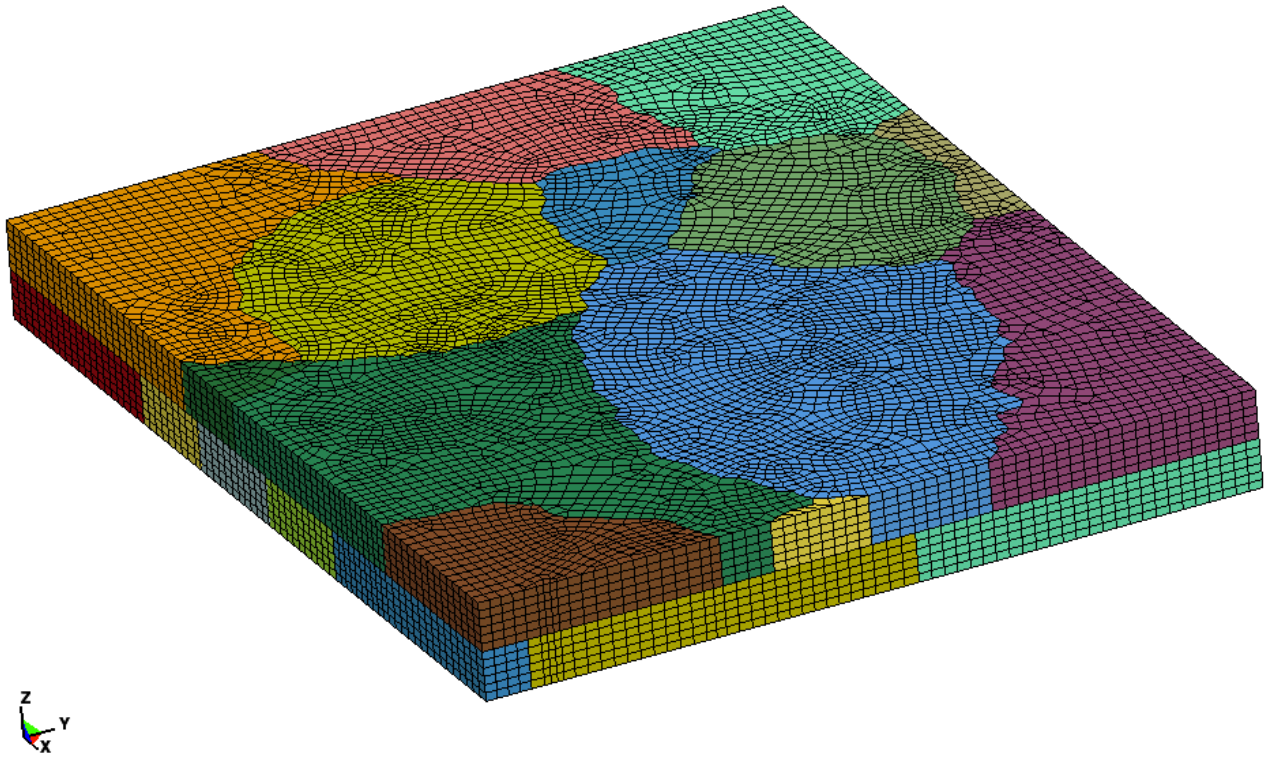

Figure 30: Final mesh for grain structure without grain boundaries (sample size 6 mm x 5 mm).

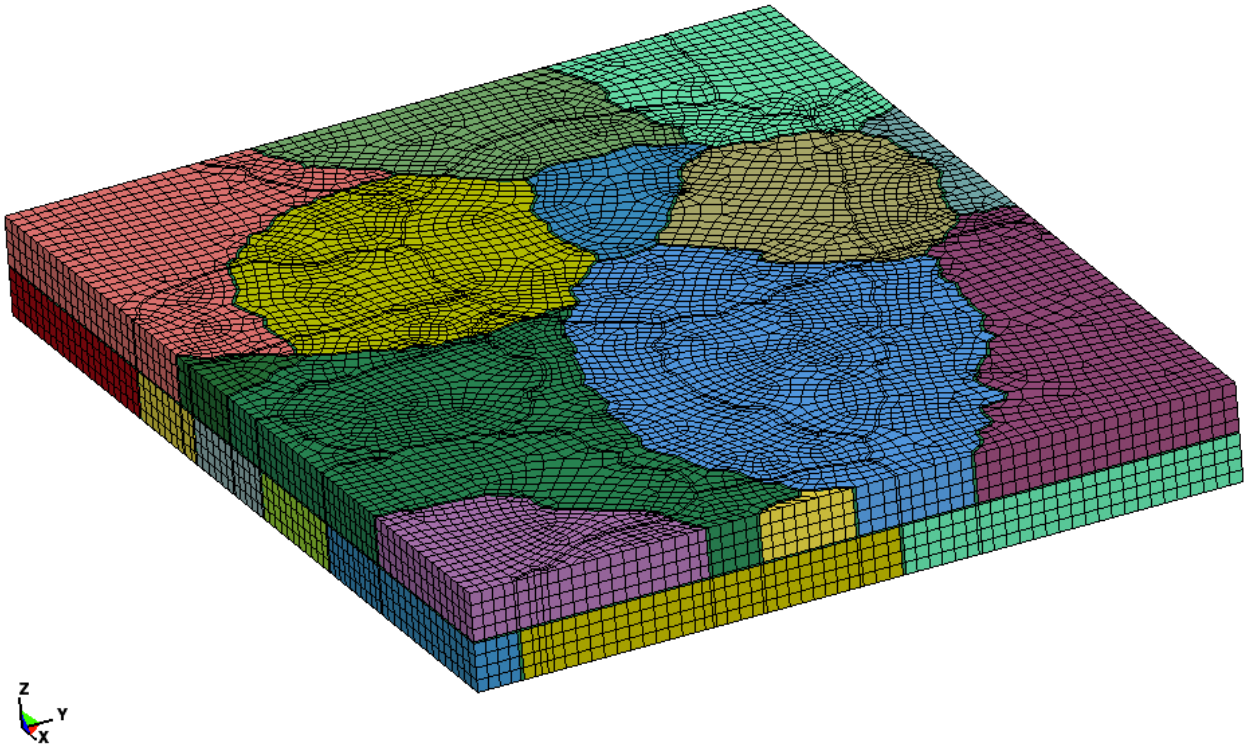

Figure 31: Final mesh for grain structure with grain boundaries (sample size 6 mm x 5 mm).

4.2.3. Model Validation

Since the goal of this work is to develop a method of modeling polycrystals that can account for grain boundary effects, the first case that should be studied is one where no boundaries exist, that is, single crystals. In the single crystal case, only the grain orientation affects the stress-strain response. This allows the single crystal constitutive model to be fitted with published single crystal data. Section 4.2.3.1 presents the single crystal fit procedure and results.

Once the single crystal constitutive properties have been established, the grain boundary properties can be established using the macroscopic polycrystal response of the sample. For the model that does not contain grain boundary zones, the macroscopic polycrystal response can be used to fit the constitutive model to act as a comparison to evaluate the benefits of modelling

grain boundary zones. It can be used to compare the effects on the results of using a grain boundary zone as opposed to using the historical method of fitting the crystal plasticity parameters. The polycrystal fit is presented in Section 4.2.3.2.

To validate the model and to quantify the improvement in the model due to adding the grain boundary zones, the in-situ DIC strain measurements from the experimental tensile test can be compared with the strain distributions measured from the simulations. The distributions can be evaluated and quantified to establish whether the addition of grain boundaries increased the accuracy of the model. The comparison is presented in Section 4.2.3.3.

4.2.3.1. Single Crystal Fit

To identify the appropriate material parameters for the crystal plasticity constitutive model, single crystal simulations were performed and compared with published single crystal aluminum data. The single crystal response shown in Figure 20, taken from Inoko et al. [2010], is used for the fitting procedure. A single element simulation of uniaxial tension was set up in LS-Dyna, and LS-Opt was used to perform a parametric study to identify the appropriate material parameters. LS-Opt is an optimization software that allows the user to select a set of simulation parameters and vary them within a certain range. The software creates an input deck for each model, and a set of custom scripts were created to allow the queuing software to communicate with LS-Opt. The first attempt at fitting the single crystal data used a power law slip hardening law from Peirce et al. [1982] presented as equation (21) in Section 3. The problem that arose from using this slip hardening model is that it is not capable of reproducing the saturation effect observed in the <001> loading direction shown in Figure 20. To obtain a closer fit with the single crystal material data, the slip hardening model was modified to the model found in Harren et al. [1989], presented in equation (24). The material parameters obtained by the LS-Opt optimization

were then checked in a single integration point, crystal plasticity, material simulator following the approach of Inal et al. [2004], to ensure the uniaxial responses given by the fitted parameters are in good agreement with the experimental data and are independent of the FE model. The material parameters found can be seen in Table 9 for the model with grain boundary zones.

Table 9: Crystal plasticity constitutive model material parameters for model with grain boundary zones.

Parameter	$\dot{\gamma}_{(0)}$	h_o	τ_o	h_s	τ_s	n
With Boundary Zones	0.001 s^{-1}	86 MPa	1.94 MPa	6.4 MPa	10 MPa	N/A

4.2.3.2. Polycrystal Fit

Once the single crystal material parameters were identified, the polycrystal meshes developed in Section 4.2.2.2 could be used to fit the grain boundary response. Initially, a simulation using the model that does not contain grain boundary zones was performed, and the overall stress versus strain response is shown in Figure 32. The tensile load in the form of applied displacement was applied at a strain rate of $125s^{-1}$ along the top and bottom edges of the model. In order to prevent out of plane distortion of the model, the nodes where the loading is applied (top on bottom of the sample) were constrained from moving in the thickness direction of the sheet. Since the real microstructure was loaded through the grip section of the sample, these boundary conditions are only an approximation of those which were actualy subjected to the physical specimen. This will cause a boundary effect along the upper and lower edges of the simulations, however this area lies outside the region of the available DIC data which is used in the following section. Since both sets of models (with and without grain boundary zones) are subjected to identical boundary conditions, a valid comparison can still be made between their results. When compared with the experimental stress versus strain curve, the model without grain

boundary zones greatly under-predicts the material response. This result is expected since the hardening phenomenon of adding grain boundaries is not included in the model. The model containing grain boundary zones was then used, where the grain boundary zones were given a piecewise phenomenological material model along with a flow stress curve. To obtain the flow stress curve for the phenomenological model, the overall macroscopic stress versus strain response from the polycrystal experimental results (Figure 23) was taken as the base for the curve. A parametric study using LS-Opt was performed, where a scalar value was used to modify the flow stress curve given to the grain boundary zones. The results from the fitting revealed that when the experimental stress versus strain curve used in the grain boundary zones is multiplied by a scalar of 5, the overall response of the polycrystal matches the experimental data, as can be seen in Figure 32. The implication of this result is that a 20-μm zone which encompasses a grain boundary will have a response that is five times harder than that of the macroscopic response. Given the existence of dislocation pileups and lattice mismatch at grain boundaries, this finding is in line with the author's expectations. The exact value of this "five times harder" is subjective since the required added hardness applied to the grain boundaries in a model changes depending on the width chosen for the grain boundary zones. Figure 33 shows the progression of the macroscopic response as the grain boundary zone hardness is increased progressively from a scale factor of 1 times the polycrystal average upto the fitted scale factor of 5. It can be seen that the macroscopic response follows a near linear trend as the grain boundary zone hardness increases. Another factor that would affect the hardness required in the grain boundary zones is the single crystal data used for the crystal plasticity model parameters. The data used for this study comes from pure aluminum single crystal, since that was what was available. The polycrystal used in this work is an AA5754 alloy. The inter-granular material properties may be

slightly different than those found for pure aluminum. Nevertheless, the goal of this research is to investigate the benefit of using this modelling approach; the effects on the simulation results will be investigated.

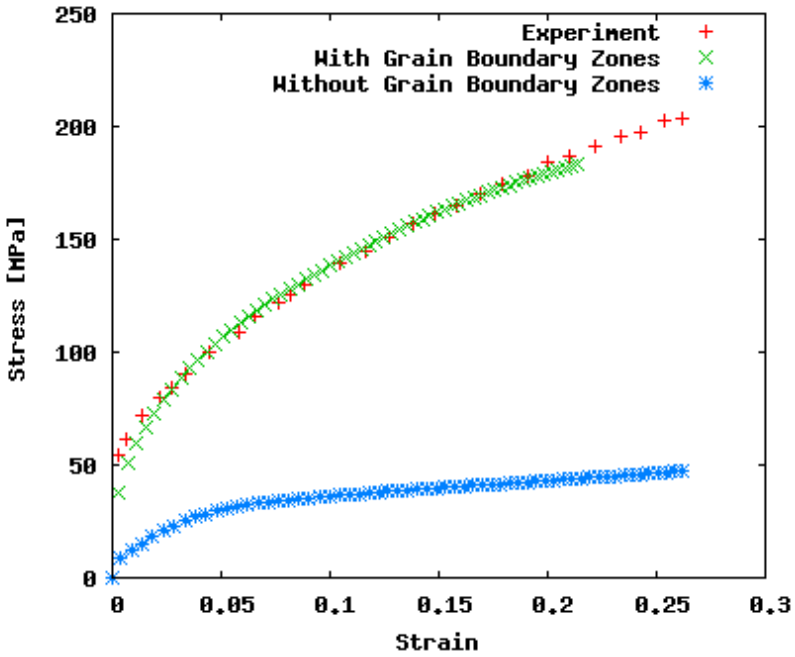

Figure 32: Stress vs. strain response for the polycrystal simulations using the single crystal fitted material response.

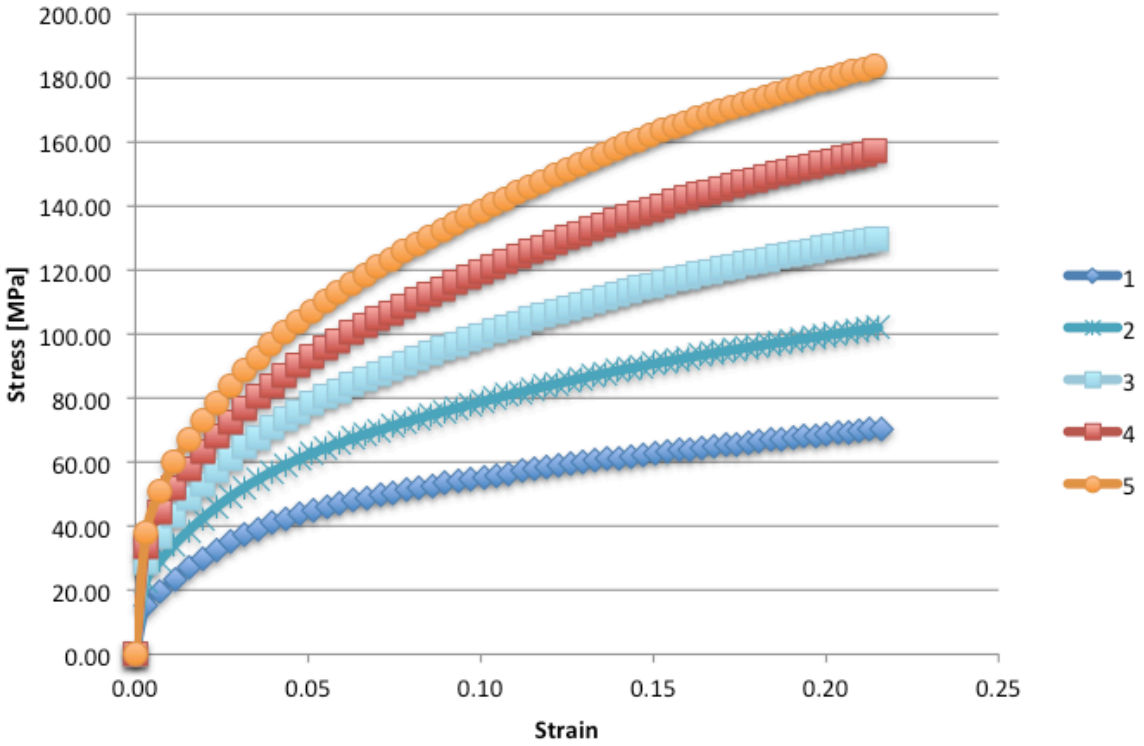

Figure 33: Stress vs. strain response for the polycrystal simulations as the grain boundary zone hardness increases from 1 times the polycrystal average up to 5 times the polycrystal average response.

To compare the modelling approach of using grain boundary zones as proposed in this work, an additional polycrystal fit was performed using the previous technique of fitting the single crystal constitutive material parameters to achieve the macroscopic response of the polycrystal. For this model, the mesh that does not contain grain boundary zones was used for the LS-Opt parametric fitting. It was found that the power law slip-hardening model given in equation (21) gave a near perfect fit when using the material parameters found in Table 10 for the model without grain boundary zones.

Table 10: Crystal plasticity constitutive model material parameters for model without grain boundary zones.

Parameter	$\dot{\gamma}_{(0)}$	h_o	τ_o	h_s	τ_s	n
Without Boundary Zones	0.001 s^{-1}	700 MPa	15 MPa	N/A	N/A	0.4

a)

b)

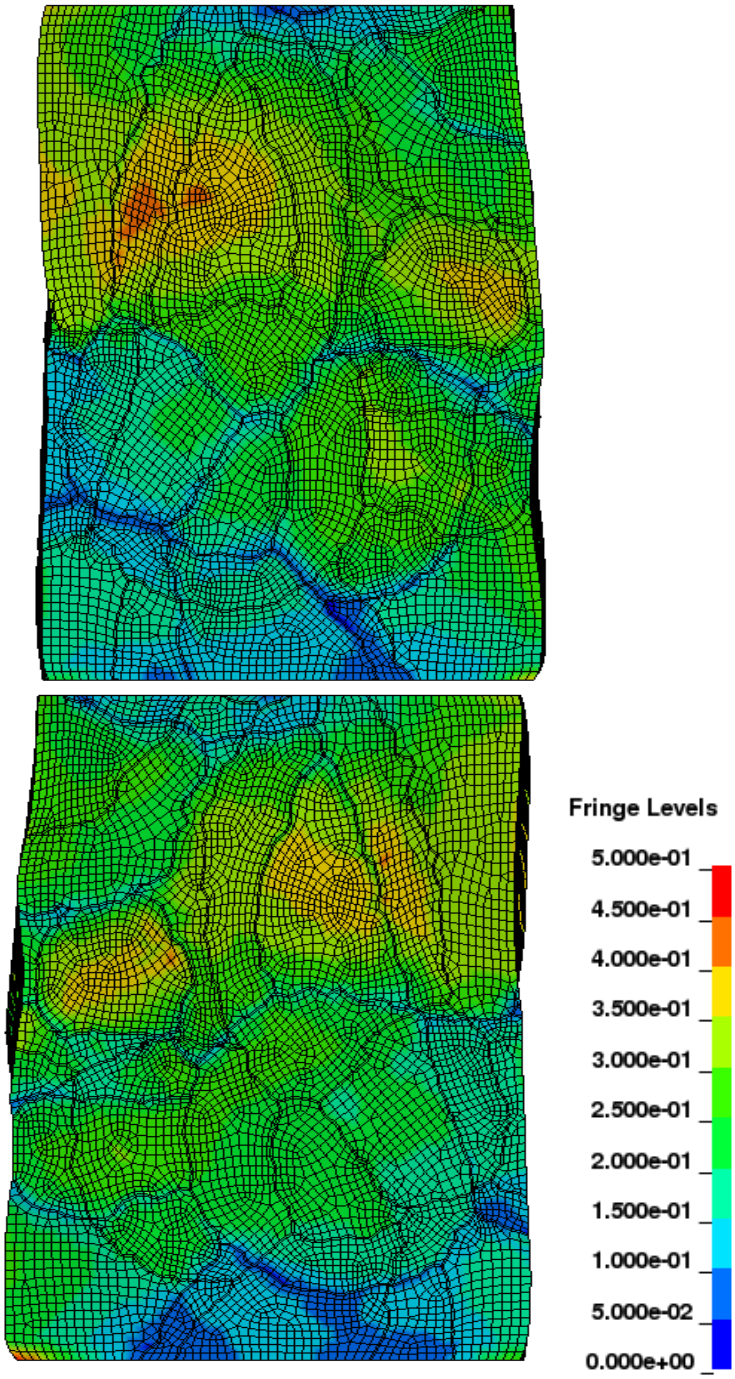

Figure 34: Fringe plot of deformed effective strain maps for the simulations with grain boundary zones at 14% applied strain (sample size 6 mm x 5 mm).

Figure 34 shows an example of the deformed mesh at 14% strain for both sides of the model that includes grain boundary zones. Figure 35 shows an example of the deformed mesh and the same point of strain for the model that does not have grain boundary zones. The results will be discussed more thoroughly in Section 4.2.5.

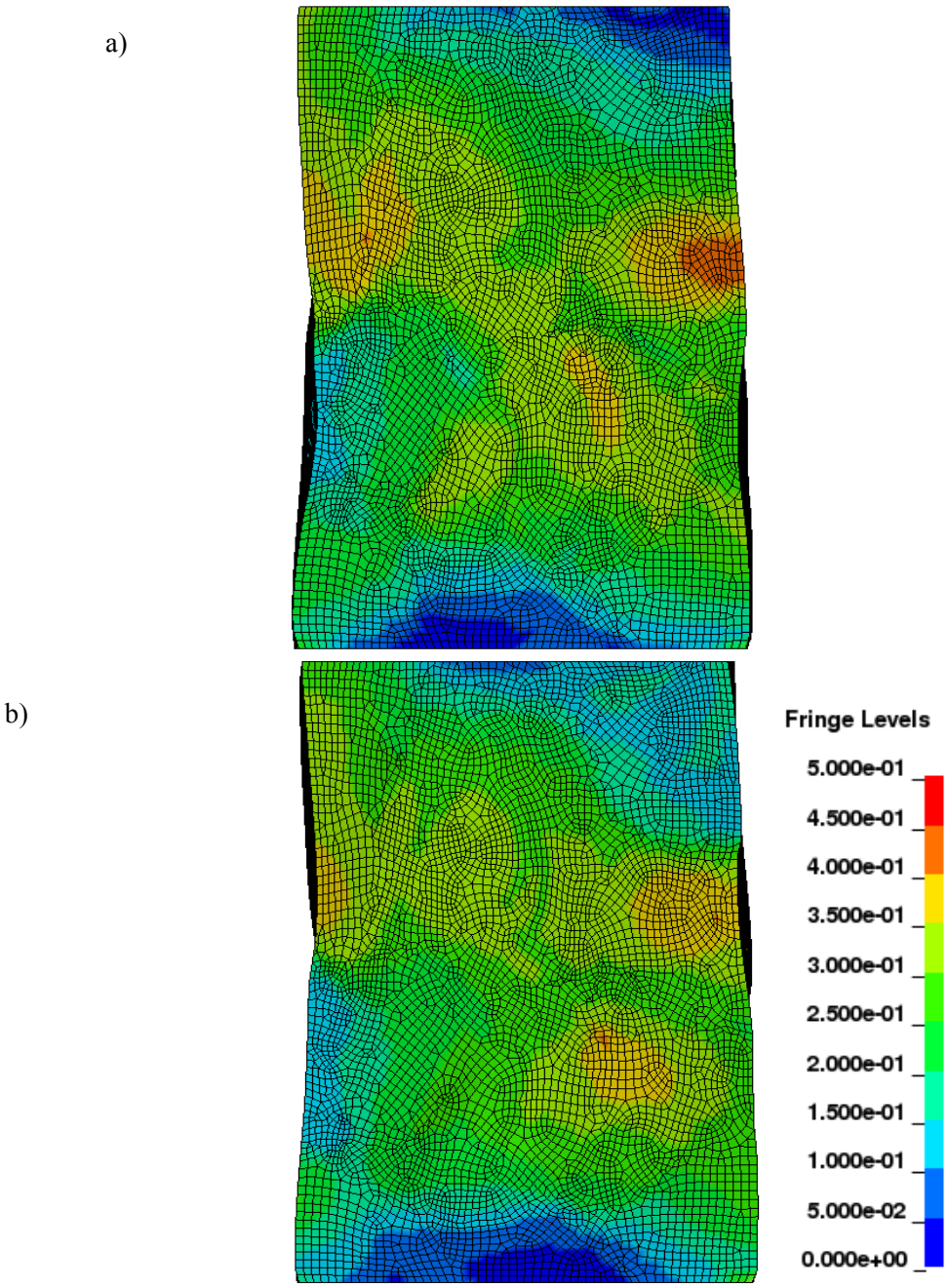

Figure 35: Fringe plot of deformed effective strain maps for the simulations without grain boundary zones at 14% applied strain (sample size 6 mm x 5mm).

4.2.3.3. Experimental DIC Comparison

The raw DIC data that was processed and presented in Zhu et al. [2011] consists of a regular grid of surface points and their in-plane displacements for each side of the sample. This raw data was processed by creating a finite element mesh consisting of quadrilateral shell elements where the DIC surface points represent the nodes of the finite element mesh and the displacements of the points represent the nodal movements. The displacements were processed using quadrilateral element shape functions to create strain distribution maps. As mentioned in Section 4.2.1, Figure 22 shows an example of this mesh, with the bad data points at a minimum. Comparing Figure 23 a) with Figure 34 a) and Figure 35 a), (presented in Figure 36 for convenience) it can be seen that the hot spots and low spots of the model containing grain boundary zones are in better agreement with the DIC data. The same conclusion can be drawn (perhaps to a lesser extent) when observing the b) sections of these same three figures (presented in Figure 37 for convenience). To quantify the superior accuracy of the model containing grain boundary zones, the models were processed to allow a direct comparison with the DIC data. The regular grid of DIC data points was overlaid onto the undeformed finite element mesh of the polycrystal. The surface nodes of the mesh that were the closest to the DIC data points were identified. The simulation results were data mined to extract the surface in-plane nodal movements of these nodes. A new data set was produced that matched the format of the initial DIC data which contained the locations of the mesh nodes closest to the DIC points and tracked their displacements throughout the simulation history. This new data set was then processed in the same manner as the initial DIC data to get a new distribution of strains that have the same resolution and direct element-to-element match with the DIC data.

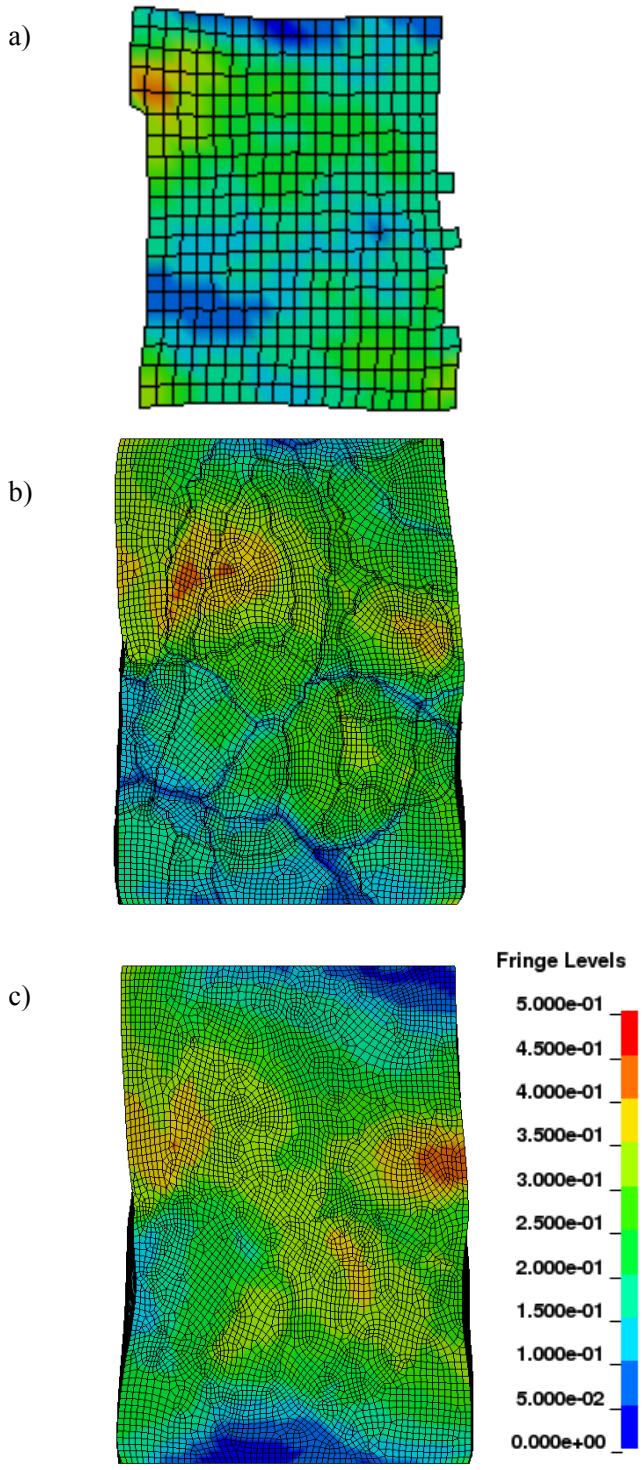

Figure 36: Fringe plots of effective strain on first side of samle for a) DIC measured results b) model with grain boundary zones, and c) model without grain boundary zones at 14% strain (sample size 6 mmx 5 mm).

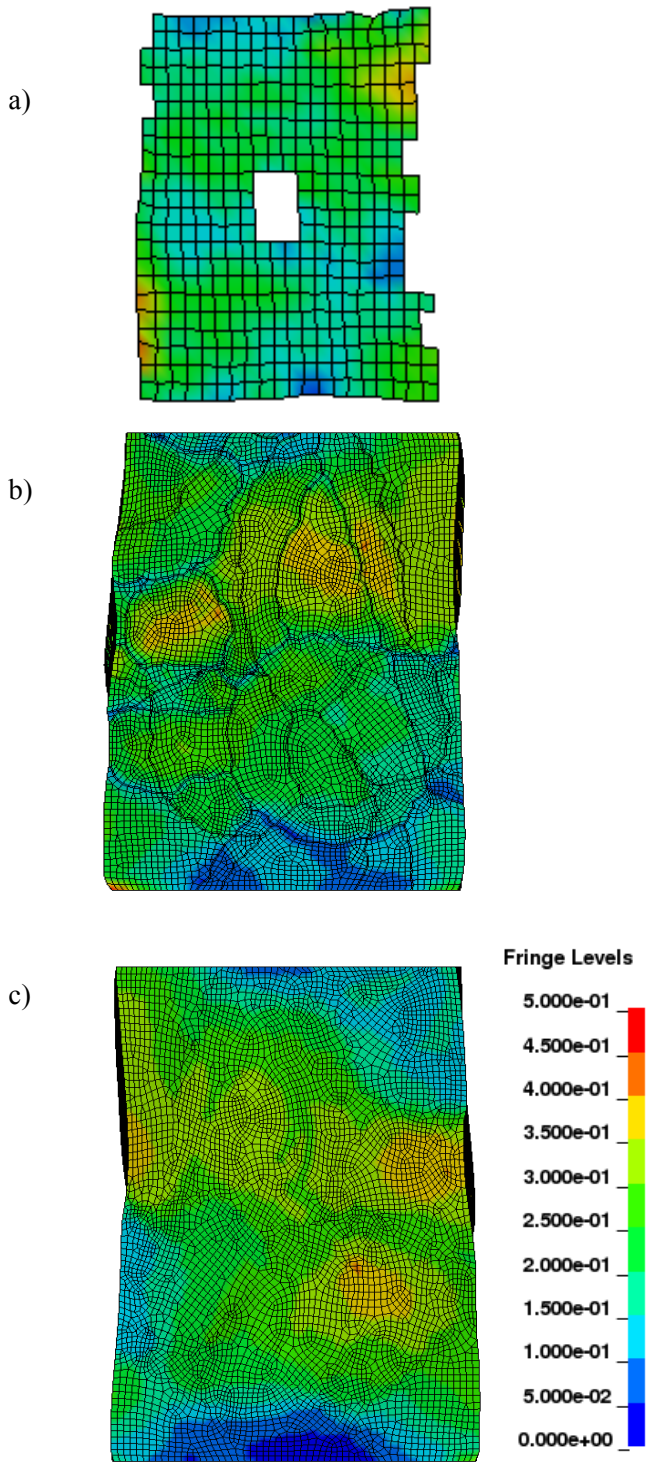

Figure 37: Fringe plots of effective strain on second side of samle for a) DIC measured results b) model with grain boundary zones, and c) model without grain boundary zones at 14% strain (sample size 6 mmx 5 mm).

A pixel based Root Mean Squared (RMS) error approach was used to quantify the accuracy of the two models (with and without grain boundary zones). A square 9-pixel window was marched along each of the three data sets (DIC data set and the two models) in 1-pixel steps, and for each step, the effective strain found within the window was averaged. For each window location, the average effective strain in the DIC data set was subtracted from the averaged strain in the models. Finally, an RMS error calculation was performed to total the error from all window locations. The reason for using a square 9-pixel window for the comparison was to make the approach capable of handling any slight misalignment of the data.

The final result is a total error of 0.122 for the model with boundary zones and an error of 0.304 for the model without boundary zones. This is a significant improvement on the model results. By including the harder grain boundary zones, 60% of the error in the model has been eliminated.

4.2.4. Mesh Sensitivity

The results from the previous section demonstrate that modeling the grain boundary zones has a positive effect on the results. The downside to including the grain boundary zones is the long computation time. The small elements that make up the zone elements cause a significant drop in the maximum time step size for the explicit FE calculations. To reduce the computation time of the model, it would be beneficial if the overall size of the grain elements could be increased to coarsen the mesh. The current size of the grain mesh is a function of the size of the small features found along the grain boundaries. If these features could be smoothed out, then larger elements could be used along the grain boundaries and the overall mesh could be coarser. To smoothen the grain boundaries, each triple point was identified and a parabolic curve was fit between the two triple points separating each section of the grain boundary. The curves were

fitted to the grain boundaries using the statistical software MYSTAT to minimize the error between the parabolic curve connecting the triple points and the grain boundary nodes found from the EBSD data. A series of equal-length bar elements were placed along the grain boundaries, and the length of the bar elements could be varied to adjust the coarseness of the mesh. Once the bar elements were created, the remaining mesh could be created using the same procedure as outlined in Section 4.2.2.2.

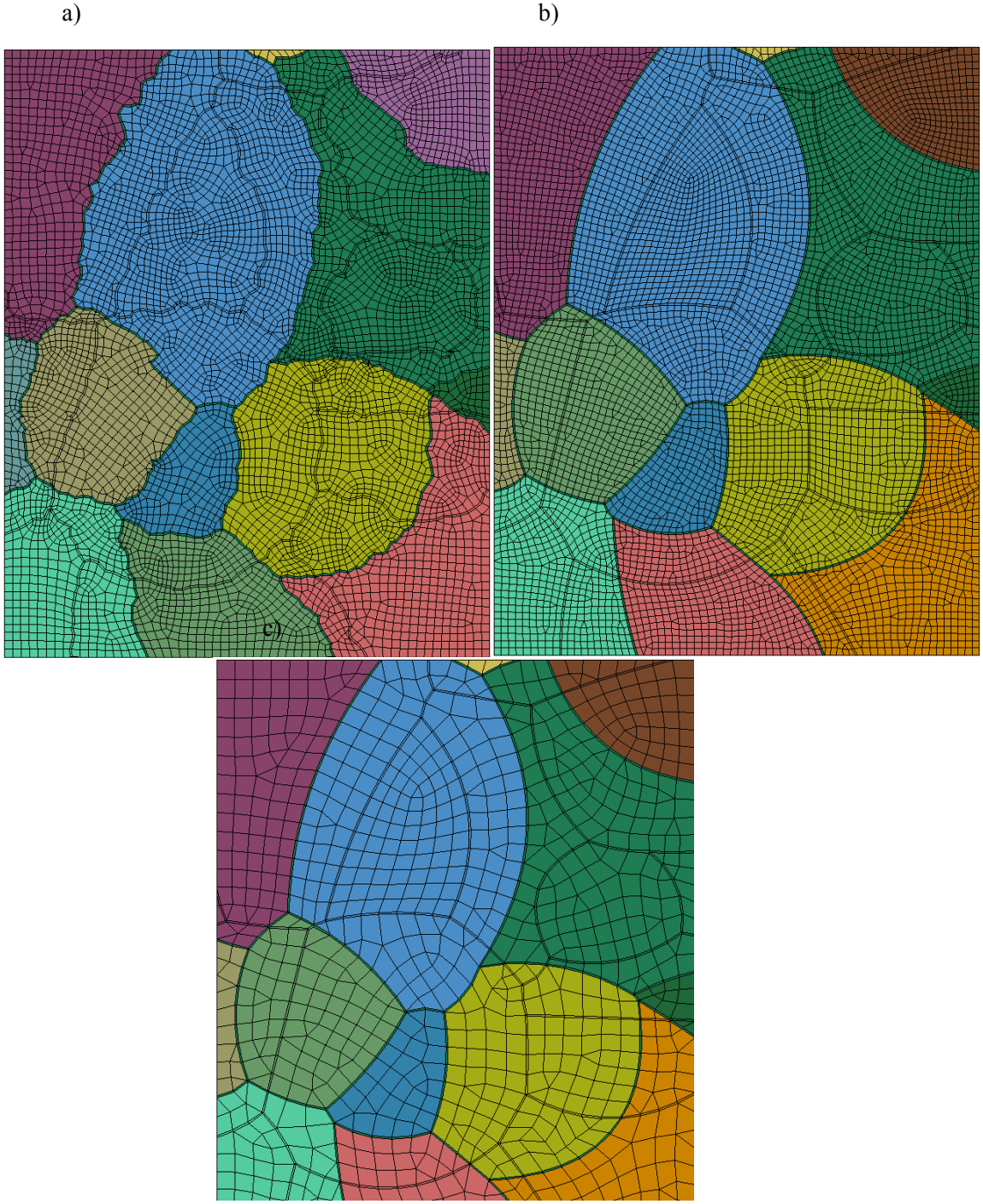

Figure 38: Finite element mesh with a) the original microstructure, b) smoothed grain boundaries with the original element size (~80 μm), and c) smoothed grain boundaries with coarsened element size (~180 μm) (sample size 6 mm x 5 mm).

Two additional meshes were created, one where the same element coarseness as the original mesh was persevered (~80 μm elements), and a second where the average element size was increased to ~180 μm. The smoothed meshes along with the original mesh are depicted in Figure 38. The uniaxial tensile stress versus strain response of these smoothed meshes along with the original mesh and the experimental data can be seen in Figure 39. It shows that smoothing the grain boundaries did not significantly affect the macroscopic stress strain response of the model, but coarsening the elements did cause a change in the resulting stress versus strain curve. The effective strain distributions for the three simulation meshes can be seen in Figure 40. Here it can be seen that while the overall strain distribution is similar when the grain boundaries are smoothed, it does affect the intensities of the strain hot spots. This would indicate that smoothening the grain boundaries to allow for larger elements and a more computationally efficient model has such a large effect on the results that it is unadvisable to smoothen them.

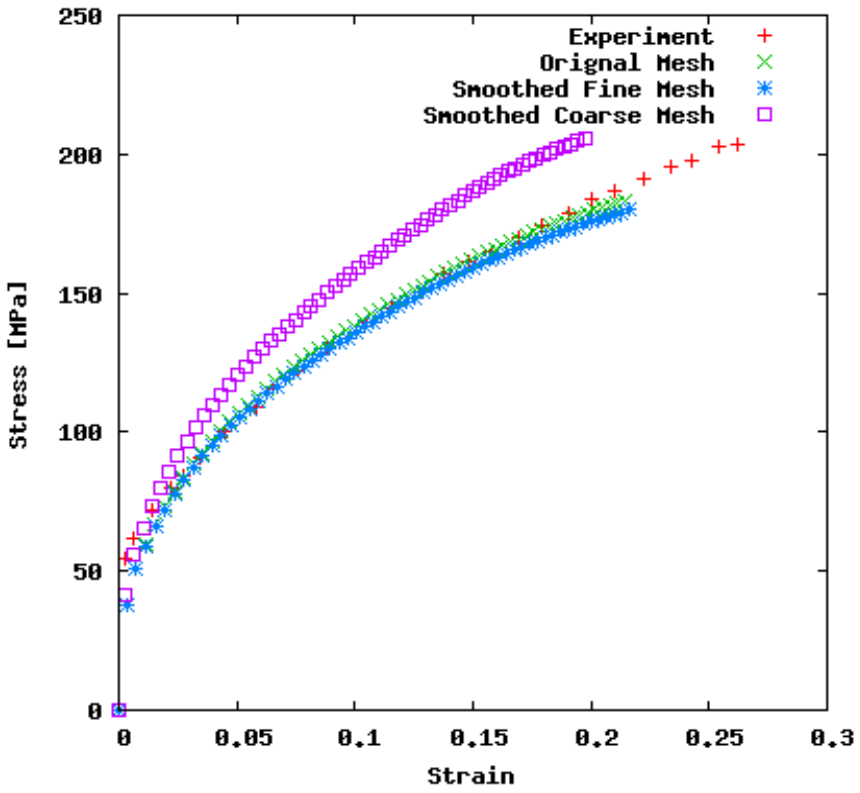

Figure 39: Stress vs. strain response for the polycrystal simulations comparing the effect of smoothing the grain boundaries and coarsening the mesh.

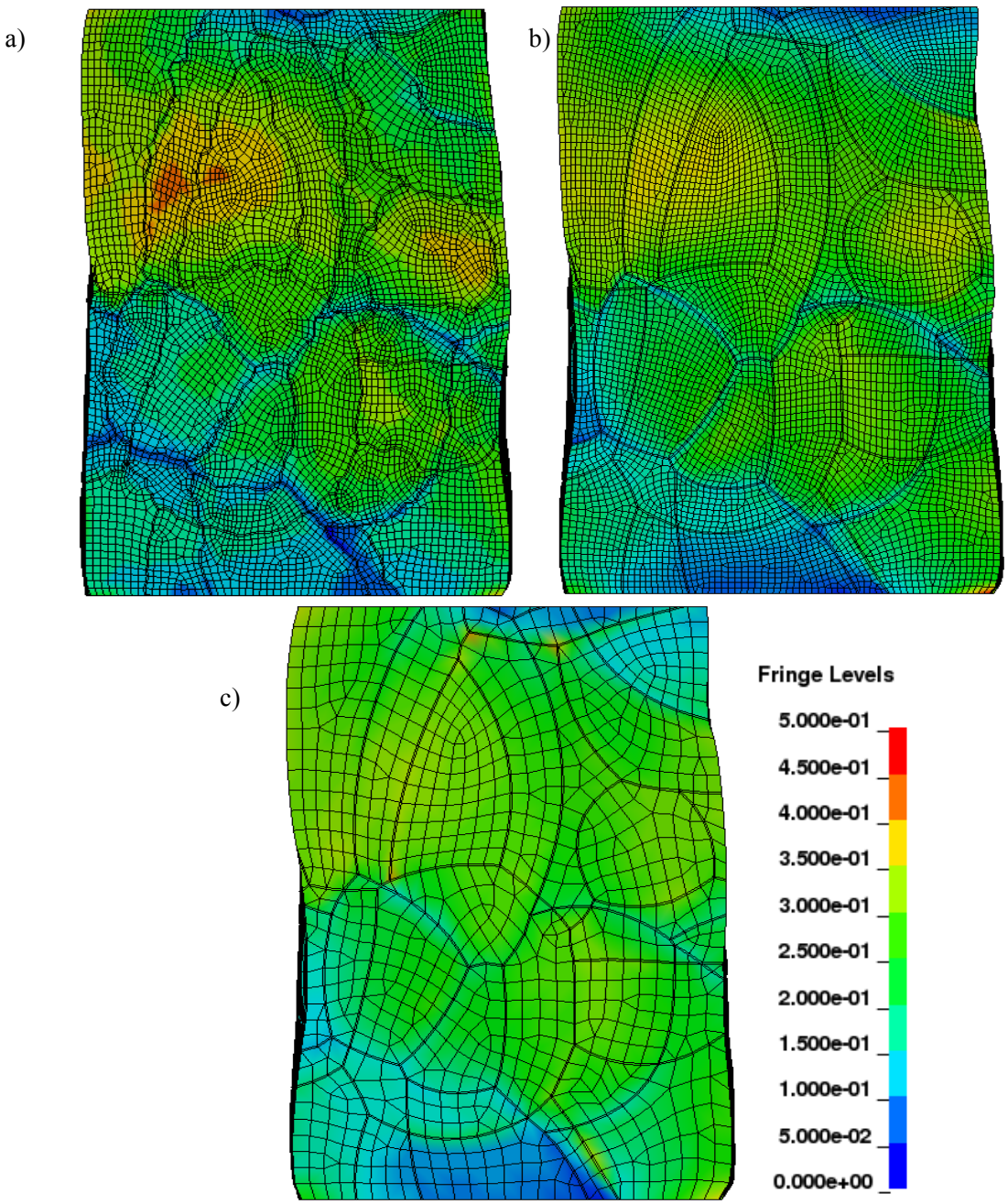

Figure 40: Fringe plot of effective strain distributions for the finite element mesh with a) the original microstructure, b) smoothed grain boundaries with the original element size (~80 μm), and c) smoothed grain boundaries with coarsened element size (~180 μm) (sample size 6 mm x 5 mm).

4.2.5. Results and Discussion

With the model validated, the overall differences in predicted strain distributions can be compared. Since uniaxial tension was done during the validation stage, it will be the first loading condition considered in Section 4.2.5.1. For a second set of simulations, bending loading was performed; the results are presented in Section 4.2.5.2.

4.2.5.1. Uniaxial Tension Loading

The effective strain results for the simulations subjected to uniaxial tension can be found in Figure 34 for the model containing grain boundary zones, and in Figure 35 for the model without grain boundary zones. These effective strain distributions apply to a macroscopic loading of 14% strain. When initially looking at the differences between these two figures, it can be immediately observe that the grain boundaries themselves are mapped out with a low strain zone in the model that includes grain boundary zones. This effect is due to the substantial increase in hardness of the grain boundary zone material, and this should be treated as an artefact of the modelling approach. True grain boundaries exist as a gradient of material properties that changes as the distance from the actual boundary interface increases. The DIC in-situ strain measurement technique used to collect the experimental data does not have the small resolution needed to capture any low strain region, such as that of an actual grain boundary zone.

When comparing Figure 36 b) and c), it can be seen that the highest spot of effective strain moves from the upper left side of Figure 36 b), which will be called Region 1, to the mid-right side in Figure 36 c), which will be called Region 2. Both of these locations contain above-average strain in each figure, the difference is which one registers as having the highest effective strain. The network of hard-grain boundaries combined with the soft grains causes an increase in the effective strain in Region 1 but a decrease in the strain found in Region 2.

4.2.5.2. Pure Bending Loading

Bending simulations were carried out with a sample of the deformed model shown in Figure 42 and the following loading conditions:

- y=0 surface is constrained so that all nodes have the same y displacement.
- y=max surface is constrained so that all nodes have the same y displacement.
- x=0 surface is constrained so that all nodes remain on the surface (but can move within the surface, and the surface is rotated about a line parallel to the y-axis passing through the center of the surface.
- x=max surface is treated in the same manner as the x=o surface only rotated in the opposite direction.
- z=0 and z=max surfaces are free to deform.

The rate of bending loading was reduced from the previous study to 48.75 rad/s due to the larger model and therefore larger succeptability to interial effects. Figure 41 shows the effective stress distribution of a trial bend at 48.75 rad/s with a piecewise material model (phenomenological) to check for the presence of inertial effects. It can be seen that the distribution of effective stress is uniform.

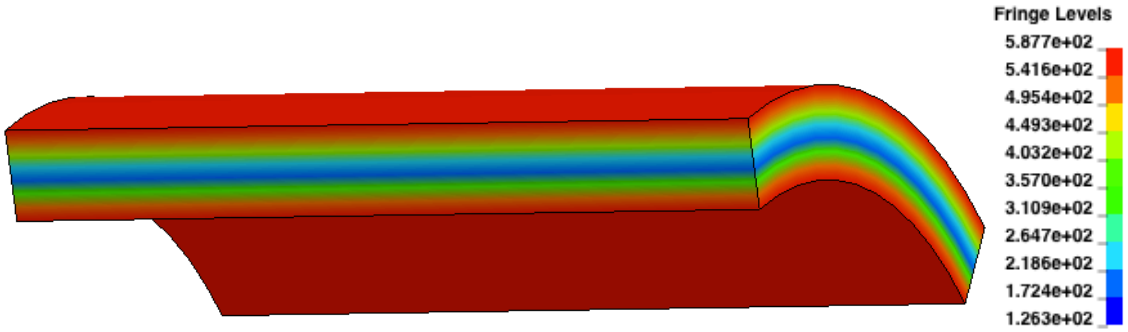

Figure 41: Fringe plot of effective stress with piecewise material model.

The simulations were performed until a total bend angle of 140° was achieved (70° of rotation on each side). Figure 43 shows the definition of a 140° bend angle.

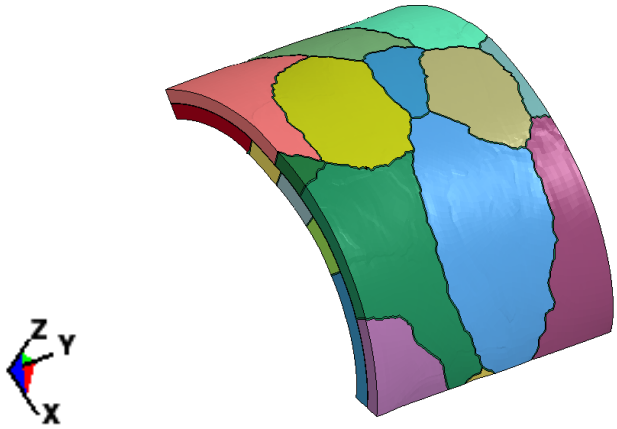

Figure 42: Sample deformation induced during the bending simulations (sample size 6 mm x 5 mm).

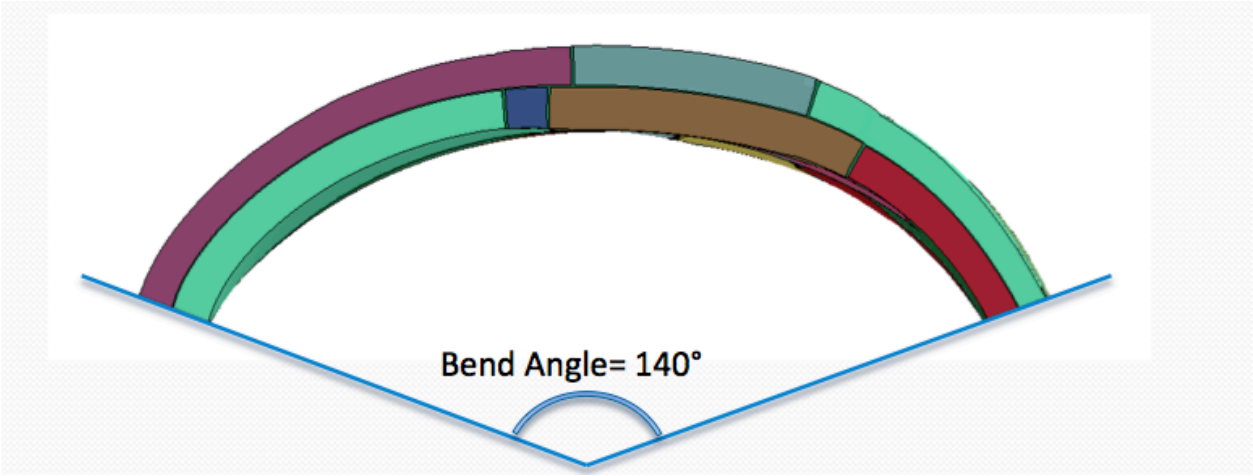

Figure 43: Bend angle of 140°

To make the results easier to observe, the result will be presented on the un-deformed mesh. Figure 44 shows the progression of transitioning the effective strain results to the un-deformed configuration for the mesh containing grain boundary zones.

a)

b)

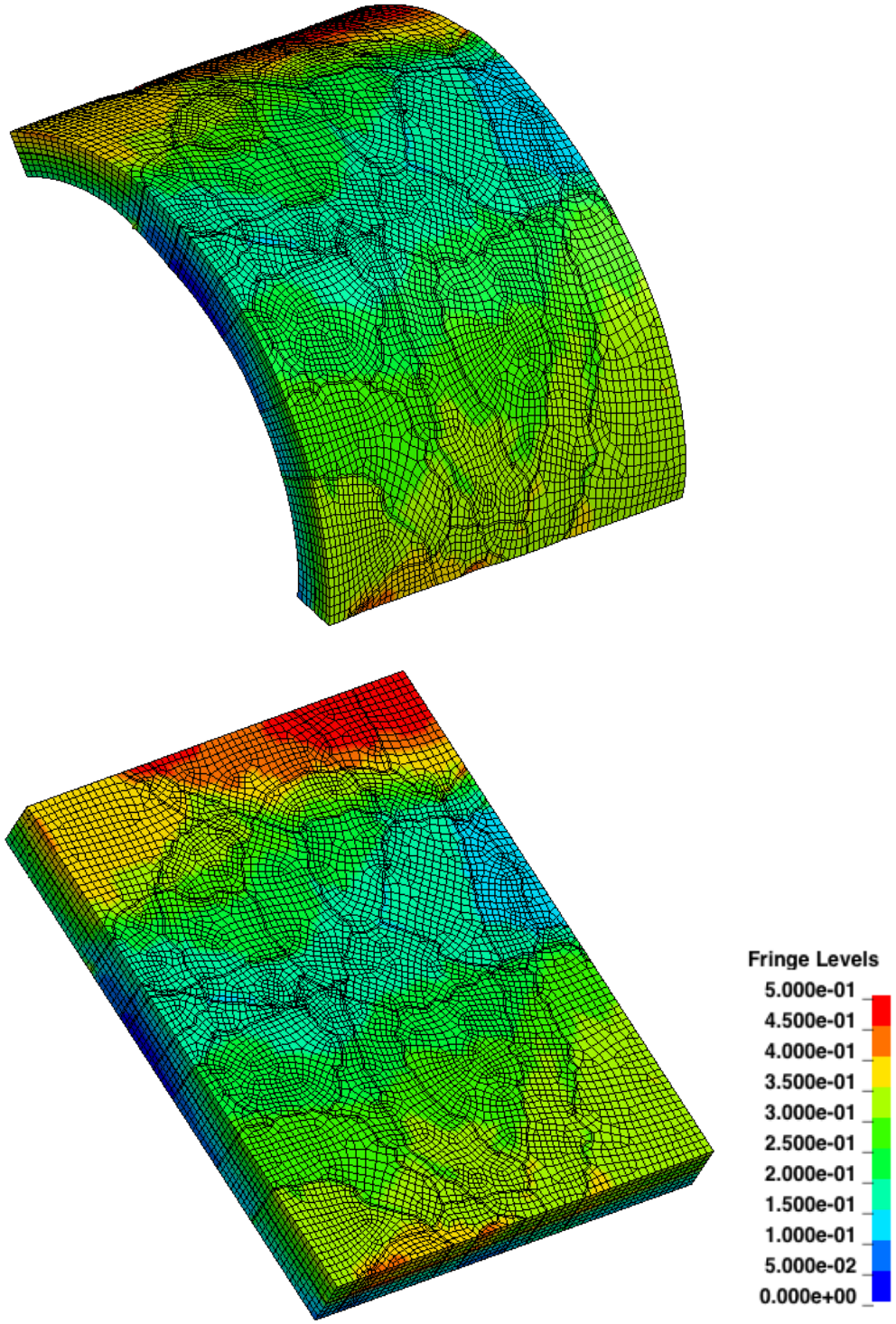

Figure 44: Fringe plot of effective strain results at a 140° bend angle, a) deformed mesh, and b) undeformed mesh (sample size 6 mm x 5 mm).

Figure 45 shows the surface thickness strain results on the top surface for both models, with grain boundary zones and without zones. It is clear that the overall top surface strain for the model with grain boundaries, Figure 45 a), experiences higher strain on average than the model without grain boundaries. Upon investigation, and it was found that the overall average thickness strain for the top half of the specimen (tensile half of the bend) is -0.166 for the model with grain boundary zones and -0.119 for the model without. Since the model experiences very little strain in the y-direction, the finding indicates that there is more tensile strain along the arc of the bend when grain boundaries are present. For there to exist more tensile strain on the top surface of the bend, the neutral axis of the bend must be shifting downwards. To view this, both deformed models were overlapped; the result is seen in Figure 46, which shows that the model with grain boundary zones has a higher arc than the model without. This would indicate that the applied load on the edges causes a more evenly distributed bend when the hard grain boundaries are present. But when the grain boundaries are omitted from the model, the grains near the edges experiencing the applied load do not transfer as much of the rotation through to the midsection of the model.

a)

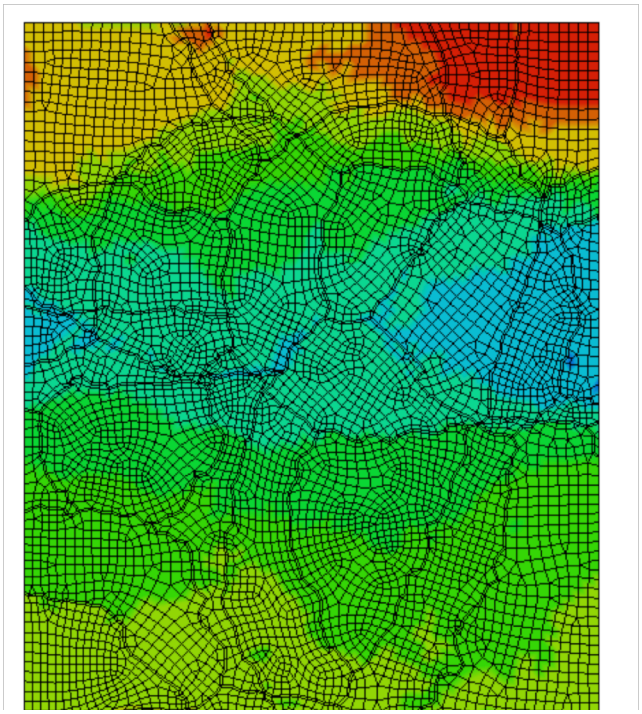

b)

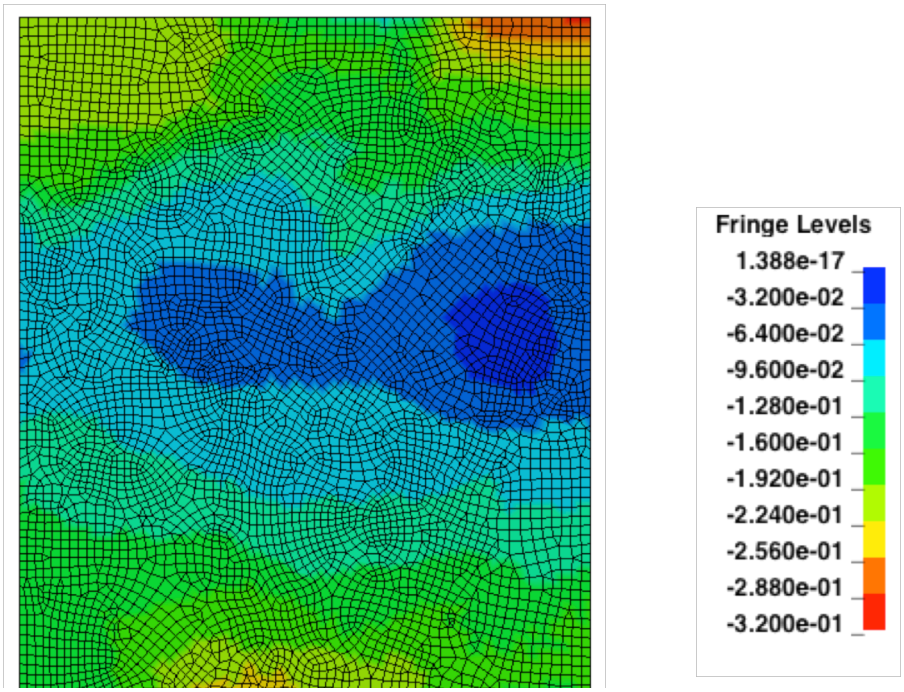

Figure 45: Fringe plot of thickness strain results at a 140° bend angle, a) with grain boundary zones, and b) without grain boundary zones (sample size 6 mm x 5 mm).

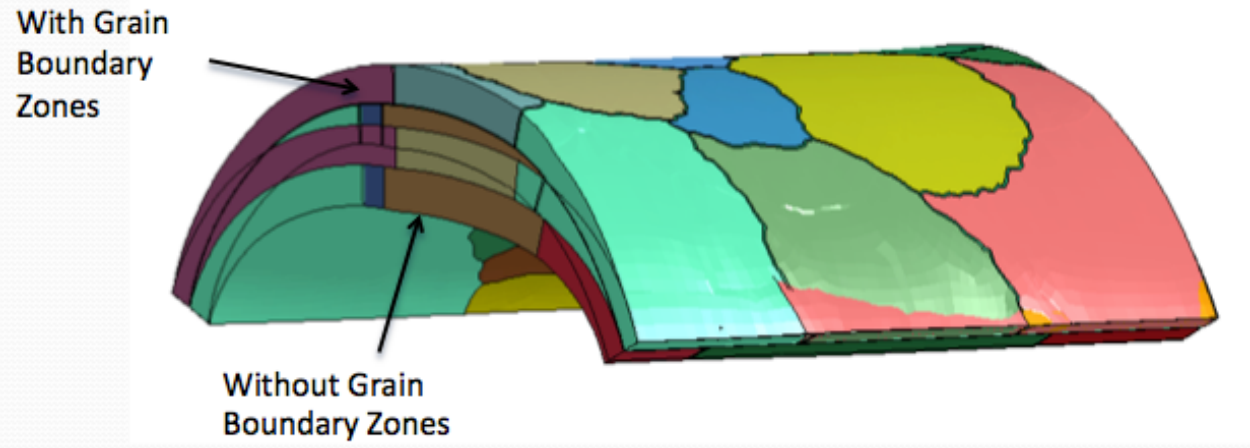

Figure 46: Overlapped models demonstrating the shift in neutral axis (sample size 6 mm x 5 mm).

A second set of simulations were performed in which the rotation applied to the x=0 and x=max surfaces were reversed. This reversed the loading to create a bend in the opposition direction. The thickness strain maps for the tensile surface of the bend at a bend angle of 90° are found in Figure 47. The average thickness strains for the tensile half for the models with grain boundary zones and without are -0.092 and -0.076, respectively. Again, it can be seen that the model without grain boundary zones does not experience as much strain due to the bending load, which indicates that the model with grain boundaries has a higher bend arc.

a)

b)

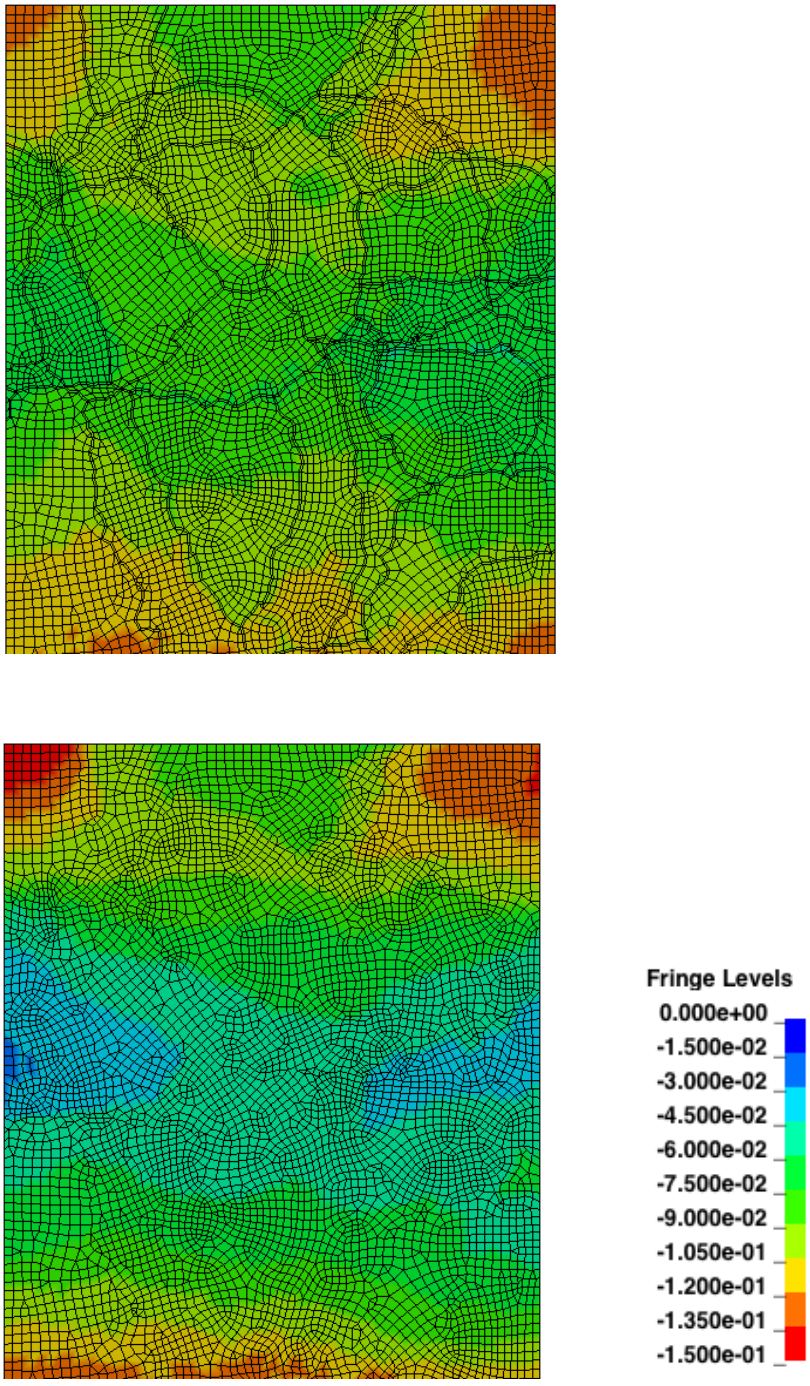

Figure 47: Fringe plots of thickness strain results at a 90° bend angle under reverse loading, a) with grain boundary zones, and b) without grain boundary zones (sample size 6 mmx 5 mm).

Surface roughness calculations were performed following the same second derivative quantification technique as used in Section 0. Trace lines were mapped along the surface both parallel and perpendicular to the axis of the bend. These trace lines had a regular sampling resolution, and identified the surface height of the model along the outer surface of the bend. The second derivative curves for the trace lines were calculated, and the standard deviation for all the lines travelling in the same direction was calculated. This results in two standard deviation values, one along the bend axis and one perpendicular. The two surface roughness values for each model can be found in Table 11. It is clear that the model containing grain boundary zones experiences much higher surface roughness, a finding attributed to the larger gradient in material properties across grain boundaries. This result indicates that modelling a bending operation by including the grain boundary zones provides a more conservative surface roughness prediction.

Table 11: Second derivative surface roughness results.

Standard deviation of 2nd Derivative [μm^{-1}]	Parallel to bend axis	Perpendicular to bend axis
With Boundary Zones	$96x10^{-5}$	$65x10^{-5}$
Without Boundary Zones	$78x10^{-5}$	$58x10^{-5}$

4.2.6. Conclusion

In this study, a new modelling approach of using hard grain boundary zones to allow the single crystal grain material properties to be used for the inter-grain material model was presented, and compared with experimental results. The motivation for the study comes from the drastic difference in material constitutive properties required for modelling single crystals versus modelling polycrystals. If a polycrystal were to be modelled with single crystal calibrated material parameters, the macroscopic response of the material would be underpredicted by a considerable margin. The introduction of grain boundary zones with harder material properties

given to a phenomenological constitutive model has allowed the single crystal parameters to be used with grains, while still achieving the desired macroscopic response of the polycrystal. Comparing the DIC experimental strain distributions with the results from the simulations has shown that introducing the harder grain boundary zones with single crystal grain properties has increased the accuracy of the model by reducing the RMS error from 0.304 to 0.122. Attempts at increasing the computation efficiency of the model by smoothening the grain boundary contours and coarsening the elements proved to be unadvisable, as the effect on the results was not insignificant.

During tensile deformation, the introduction of the grain boundary zones affects the strain partitioning of the model and moves the location of the highest strain concentration. During bending, loading the addition of grain boundary zones causes a higher bend arc, along with increased surface roughness on the outer surface of the bend.

5. Conclusions

The work performed in the two studies presented in Section 4 were conducted with the intention to expand our understanding of how aluminum behaves during bending and to develop an efficient modelling technique for including the effects of grain boundaries. The first of these two intentions was achieved through the first study, that is, surface roughness during bending; the second intention was achieved through the second study, that is, modelling of grain boundaries.

The first study demonstrated that the two crystallographic orientations to be avoided when producing aluminum to enhance bendability are Goss and Brass. Goss produces high anisotropic responses, limiting the material's versatility for forming. Although it is possible in some circumstances to align the forming processes to ensure the material is loaded in the desired loading directions only, it is not a desirable approach, because it leads to increased scrap and inefficient material use. By reducing the Goss content of the material, blanks can be cut in any orientation of the sheet, and the wasted material can be minimized with properly designed cutting dies.

Brass negatively affects the developed surface roughness across the whole range of neighbouring orientations for all loading directions. Increasing the Brass content reduces the bendability of the material in all situations, therefore adding Brass should be avoided if possible.

The first study also revealed that surface roughness develops as a product of strain incompatibility. It is the mismatch in strain from one orientation to its neighbouring orientation that leads to enhanced surface roughness, and it can be both at the surface of the sample and beneath the surface. The study revealed the presence of local strain hotspots beneath the surface

of the sample, contributing to the measured surface roughness. This finding confirms the need for utilizing full 3D models when performing bending studies.

To further the accuracy of the 3D models, a reasonably efficient method of representing the grain boundaries within the microstructure is needed. The second study in this thesis revealed that using grain boundary zones to represent the boundaries reduced the error in the predicted strain distribution by 60%. This method allows the same crystal plasticity parameters to be used for both single crystal models and polycrystal models, which reduces the amount of fitting requirements as well as provides a closer link between the models and real material physics. The disadvantage of this approach is that polycrystal data need to be processed to identify all the grain boundaries and the mesh needs to be created, including the grain boundary zones. It was found during the study to not be possible to smoothen the grain boundaries and reduce the number of element in the model without affecting the simulation results.

During the bending portion of the section study, it was observed that the structure of grain boundaries acts to support the grains, and distributes the bending strain more evenly over all the grains. This produced a more even bend arc, resulting in a high average tensile strain on the outer surface of the bend.

6. Future Work

For future developments in this work, a study analysing a range of different polycrystals, each with a unique grain size, is recommended, to evaluate the effectiveness of modeling the grains with grain boundary zones as a method of capturing grain size effects.

User-friendly software should be developed to produce meshes with grain boundary zones. The programs written during this research could be used as a basis for the user-friendly version. With user-friendly software, small adjustments could be quickly made to the mesh to investigate the sensitivy of the model results to the grain boundary zone thickness.

The work can be extended to try and account for other deformation mechanism such as twinning or grain boundary sliding.

Work can be performed employing the grain boundary model to develop a constitutive model that can account for the effects of the grain boundary.

Experimental work can be performed where the content of Brass and Goss within aluminum is varied and subsequent bending tests performed to analyse the developed surface roughness and overall change in formability.

References

Abernathy, J.L, 1976, Manufacturing Processes for aluminum-steel hoods. SAE 760056, 1-6.

Angelo, J.E., Moody, N.R., Baskes, M.I., 1995, Trapping of hydrogen to lattice defects in nickel. Modelling Simulation Material Science Engineering, 3, 289-307.

Asaro, R.J., Needleman, A., 1985. Texture development and strain hardening in rate dependent polycrystals. Acta Metallurgica, 33, 923-953.

Aust, K.T., Chen, N.K., 1954, Effect of orientation difference on the plastic deformation of aluminum bycrystals. Acta Metallurgica, 2, 632.

Baskes, M.I., 1984, Dynamical calculation of low energy hydrogen reflection. Journal of Nuclear Materials, 128, 676-680.

Baudin, T., Penelle, R., 1993, Determination of the total texture function from individual orientation measurements by electron backscattering pattern. Metallurgical Transactions A, 10, 2299-2311.

Becker, R., 1998. Effect of Strain Localization on Surface Roughening during Sheet Forming. Acta Materialia, 46(4), 1385-1401.

Benedetti, I., Aliabadi, M.H., 2013, A three-dimensional cohesive-frictional grain-boundary micromechanical model for intergranular degradation and failure in polycrystalline materials. Computational Methods Applied Mechanics Engineering, 265, 36-62.

Bhattacharyya, A., El-Danaf, E., Kalidindi, S., Doherty, R., 2000, Evolution of grain-scale microstructure during large strain simple compression of polycrystalline aluminum with quasi-

columnar grains: OIM measurements and numerical simulations. Inernational Journal of Plasticity, 17, 861-883.

Bishop, J.F.W., Hill, R., 1951a. A theory of the Plastic Distortion of a Polycrystalline Aggregate under Combined Stresses. Philosophical Magazine 42, 414-427.

Bishop, J.F.W., Hill, R., 1951b. A Theoretical Derivation of the Plastic Properties of a Polycrystalline Face Centered Metal. Philosophical Magazine 42, 1298-1307.

Brahme, A., Staraselski, Y., Inal, K., Mishra, R.K., 2012, Determination of the minimum scan size to obtain representative textures by electron backscatter diffraction. Metallurgical and Materials Transactions A, 43, 5298-5307.

Budiansky, B., Wu, T.T., 1962, Theoretical Prediction of Plastic Strains of Polycrystals, Proceedings of the 4th Congress of Applied Mechanics, 1175.

Camacho, G.T., Ortiz, M., Computation modelling of impact damage in brittle materials. International Journal of Solids and Structures, 33, 2899-2938.

Chalmers, B., 1937, The influence of the difference of orientation of two crystals on the mechanical effect of their boundary. Proceedings of the Royal Society of London A, 162, 0120-0127.

Cherkaoui, M., Berveiller, M., 2000. Mechanics of Materials Undergoing Martensitic Phase Change: A Micro-Macto Approach for Transformation Induced Plasticity. ZAMM 80, 219-232.

Dao, M., Li, M., 2001. A micromechanics study on strain-localization-induced fracture initiation in bending using crystal plasticity models. Philosophical Magazine A, 81(8), 1997-2020.

Davidkov, A., Jain, M.K., Petrov, R.H., Wilkinson, D.S., Mishra, R.K., 2012, Strain localization and damage development during bending of Al-Mg alloy sheets. Materials Science and Engineering A 550, 395-407.

Davut, K., Zaefferer, S., 2010, Statistical Reliability of phase fraction determination based on electron backscatter diffraction (EBSD) investigations on the example of an AL-TRIP steel. Metallurgical and Materials Transactions A, 41, 2187-2196.

Delannay, L., Jacques, P.J., Kalidindi, S.R., 2006, Finite element modeling of crystal plasticity with grains shaped as truncated octahedrons. International Journal of Plasticity 22, 1879-1898.

Duncan, J.L., Ragab, A.R., 1973, Comparison of bending and tension tests in creep of sheet metal. Journal of Testing and Evaluation, 1, 451-456.

Easton, M., Song, W.Q., Abbott, T., 2006, A comparison of the deformation of magnesium alloys with aluminium and steel in tension, bending and buckling. Materials and Design, 27, 935-946.

Erinosho, T.O., Cocks, A.C.F., Dunne, F.P.E., 2013, Texture, hardening and non-proportionality of strain in BCC polycrystal deformation. International Journal of Plasticity, 50, 170-192.

Eshelby, J.D., 1957, The Deformation Behaviour of the Elastic Field of an Ellipsoidal Inclusion and Related Problems, Proceedings of the Royal Society of London A241, 376-396.

Espinosa, H., Zavattieri, P., 2002a, A grain level model for the study of failure initiation and evolution in polycrystalline brittle materials. Part I: Theory and numerical implementation. Mechanics of Materials, 35, 333-364.

Espinosa, H., Zavattieri, P., 2002b, A grain level model for the study of failure initiation and evolution in polycrystalline brittle materials. Part II: Numerical examples. Mechanics of Materials, 35, 365-394.

Evancho, J.W., Kaufman, J.G., 1977, New 6XXX-Series alloys for auto body sheet. SAE 770307, p1-8.

Finelli, T.M., Kelly, B., 1977, Design and manufacturing considerations for aluminum hood assemblies. SAE 770336, p1-8.

Geist, G.J., Parker, B.A., 1984, Experimental studies of the strain distributions in bends from aluminium sheet. Journal of Mechanical Working Technology, 9, 201-207.

Groche, P., Schäfer, R., Justinger, H., Ludwig, M., 2010, On the correlation between crystallographic grain size and surface evolution in metal forming processes. International Journal of Mechanical Sciences, 52, 523-530.

Guillotin, A., Guiglionda, G., Maurice, C., Driver, J.H., 2011, Correlation of surface roping with through-thickness microtextures in an AA6xxx Sheet. Metallurgical and Materials Transactions A, 42, 1919-1924.

Harren, S., Lowe, T.C., Asaro, R.J., Needleman, A., 1989, Analysis of large-strain shear in rate-dependent face-centered cubic polycrystals: Correlation of micro and macromechanics. Philosophical Transactions of the Royal Society of London A, 328, 443-500.

Hill, R., 1965, Continuum Micro-Mechanics of Elasto-Plastic Polycrystals. Journal of Mechanics Physics and Solids,13, 89-101.

Hill, R., Rice, J.R., 1972, Constitutive analysis of elastic-plastic crystals at arbitrary strain. Journal of Mechanics Physics and Solids, 20, 401-413.

Hu, X.H., Jain, M., Wu, P.D., Wilkinson, D.S., Mishra, R.K., 2010, A macro-micro multi-level modeling scheme to study the effect of particle distribution on wrap-bendability of AA5754 sheet alloys. Journal of Materials Processing Technology, 210, 1232-1242.

Hutchinson, J.W., 1970. Elastic-plastic behaviour of polycrystalline metals and composites. Proceedings of the Royal Society of London A, 319, 247-272.

Iacono, C., Sinke, J., Benedictus, R., 2010, Prediction of minimum bending ratio of aluminum sheets from tensile material properties. Journal of Manufacturing Science and Engineering, 132, 021001-1-9

Ikawa, S., Asano, M., Kurad, M., Yoshida, K., 2011, Effects of crystal orientation on bendability of aluminum alloy sheet. Materials Science and Engineering A, 528, 4050-4054.

Inal, K., Mishra, R.K., Cazacu, O., 2010. Forming simulation of aluminum sheets using an anisotropic yield function coupled with crystal plasticity theory. International Journal of Solids and Structures 47, 2223-2233.

Inal, K., Neale, K.W., Aboutejeddine, A., 2004, Forming limit comparisons for FCC and BCC sheets. International Journal of Plasticity, 21, 1255-1266.

Inoko, F., Kashihara, K., Tagami, M., Okada, T., 2010, Relationship between <111> rotation recrystallization mechanism and slip bands with compressive strains during tensile deformation in aluminum single crystals. Materials Transactions, 51, 597-606.

Ivlieva, O.V., Novikov, I.I., 1990, Determination of the burning temperature for aluminum alloys by a bending method with heating. Metallovedenie I Termicheskaya Obrabotka Metallov, 11, 58-59.

Izadbakhsh, A., Inal, K., Mishra, R.K., 2010. Numerical formability assessment in single crystals of magnesium. Computational Materials Science 50, 571-585.

Jain, M., Allin, J., Bull, M.J., 1998, Deep drawing characteristics of automotive aluminum alloys. Materials Science and Engineering A, 256, 69-82.

Jin, H., Lloyd, D.J., 2013, Improvement of bendability in Fusion AA3003/AA6xxx sheets with different clad thickness after artificial aging. Materials Science and Technology, 29, 1447-1452.

Kheradmand, N., Vehoff, H., Barnoush, A., 2013, An insight into the role of the grain boundary in plastic deformation by means of a bicrystalline pillar compression test and atomistic simulation. Acta Materialia, 61, 7454-7465.

Kochendorfer, A., 1941, Plastiche Eigenschaften von Kristallen und Metallischen Werkstoffen, Springer, Berlin.

Kocks, U.F., Tome, C.N., Wenk, H.R., Mecking, H., 2001. Texture and Anisotropy. Cambridge University Press.

Kröner, E., 1958, Berechnung der Elastischen Konstanten des Vielkristalls aus den Konstanten des Einkristalls, Zeitschrift für Physik, 151, 504-518.

Kuroda, M., Tvergaard, V., 2004, Shear band development in anisotropic bent specimens. European Journal of Mechanics A, 23, 811-821.

Kuroda, M., Tvergaard, V., 2007, Effects of texture on shear band formation in plane strain tension/compression and bending, International Journal of Plasticity, 23, 244-272.

Lee, J.W., Lee, M.G., Barlat, F., 2012, Finite element modeling using homogeneous anisotropic hardening and application to spring-back prediction. Inernational Journal of Plasticity, 29, 13-41.

Lefebvre, G., Sinclair, C.W., Lebensohn, R.A., Mithieux, J-D., 2012, Accounting for local interactions in the prediction of roping of ferritic stainless steel sheets. Modelling Simulation Material Science Engineering, 20, 024008-1-16.

Lele, S., Anand, L., 2009, A large-deformation strain-gradient theory for isotropic viscoplastic materials. International Journal of Plasticity, 25, 420-453.

Levinson, A., Mishra, R.K., Doherty, R.D., Kalidindi, S.R., 2012, Microstructure evolution during roller hemming of AZ31B Magnesium sheet. Metallurgical and Materials Transactions A, 43A, 3824-3833.

Li, M., Ghosh, S., Rounds, T., Weiland, H., Richmond, O., Hunt, W., 1998, Serial Sectioning Method in the Construction of 3-D Mictrostructures for Particle-Reinforced MMCs. Materials Characterization, 41(2-3), 81-95.

Li, S., Van Houtte, P., Kalidindi, S.R., 2004, A quantitative evaluation of the deformation texture predictions for aluminium alloys from crystal plasticity finite element method. Modelling and Simulation in Materials Science and Engineering, 12, 845-870.

Liao, K.C., Chen, C.L., 2010, Investigation of surface roughness of aluminum alloy sheet based on crystalline plasticity model. Computation Materials Science, 49, S47-S53.

Lienert, U., Li, S.F., Hefferan, C.M., Lind, J., Suter, R.M., Bernier, J.V., Barton, N.R., Brandes, M.C., Mills, M.J., Miller, M.P., Jakobsen, B., Pantleon, W., 2011, High-Energy Diffraction Microscopy at the Advanced Photon Source. JOM, 63(7), 70-77.

Lim, H., Lee, M.G., Kim, J.H., Adams, B.L., Wagoner, R.H., 2011, Simulation of polycrystal deformation with grain and grain boundary effects, International Journal of Plasticity, 27, 1328-1354.

Lin, G., Hu, S., Cai, W., 2009, Evaluation of formability in bending/hemming of aluminum alloys using plane-strain tensile tests. Journal of Manufacturing Science and Engineering, 131, 051009-1-9.

Lloyd, D.J., Evans, D., Pelow, C., Nolan, P., Jain, M., 2002, Bending in aluminium alloys AA 6111 and AA 5754 using the cantilever bend test. Materials Science and Technology, 18, 621-628.

Lucachick, G.A., Sanchez, L.R., 2013, Surface topography changes in aluminum alloy sheet during large plastic straining under cyclic pure bending. Journal of Materials Processing Technology, 213, 300-307.

Mattei, L., Daniel, D., Guiglionda, G., Klöcker, H., Driver, J., 2013a, Strain localization and damage mechanisms during bending of AA6016 sheet. Materials Science and Engineering A, 559, 812-821.

Mattei, L., Daniel, D., Guiglionda, G., Moulin, N., Klöcker, H., Driver, J., 2013b, Grain scale modeling of the bendability of AA6xxx Al alloy sheet. Materials Science and Engineering A, 583, 96-104.

Matteson, T.L., Schwarz, S.W., Houge, E.C., Kempshall, B.W., Giannuzzi, L.A., 2002, Electron Backscattering Diffraction Investigation of Fucused Ion Beam Surfaces. Journal of Electronic Materials, 31 (1), 33-39.

Mohammadi, A., Vanhove, H., Van Bael, A., Duflou, J.R., 2012, Bending properties of locally laser heat treated AA2024-T3 aluminum alloy. Physics Procedia, 39, 257-264.

Mompiou, F., Caillard, D., Legros, M., 2009, Grain boundary shear-migration coupling-I. In situ TEM straining experiments in Al polycrystals. Acta Materialia, 57, 2198-2209.

Muderrisoglu, A., Murata, M., Ahmetoglu, M.A., Kinzel, G., Altan, T., 1996, Bending, flanging, and hemming of aluminum sheet-an experimental study. Journal of Materials Processing Technology, 59, 10-17.

Nakamachi, E., Tam, N.N., Morimoto, H., 2007. Multi-scale finite element analyses of sheet metals by using SEM-EBSD measure crystallographic RVE models. International Journal of Plasticity 23, 450-489.

Nygårds, M., Gudmundson, P., 2004, Numerical investigation of the effect of non-local plasticity on surface roughening in metals. European Journal of Mechanics A, 23, 753-762.

Onck, P., van der Giessen, E., 1999, Growth of an initially sharp crack by grain boundary cavitation. Mechanics and Physics of Solids, 47, 99-139.

Peirce, D., Asaro, R.J., Needleman, A., 1982. An analysis of nonuniform and localized deformation in ductile single crystals. Acra Metallurgica 30, 1087-1119.

Potirniche, G.P., Hearndon, J.L., Horstemeyer, M.F., Ling, X.W., 2006. Lattice orientation effects on void growth and coalescence in fcc single crystals. International Journal of Plasticity 22, 921.

Raabe, D., Sachtleber, M., Weiland, H., Scheele, G., Zhao, Z., 2003. Grain-scale micromechanics of polycrystal surfaces during plastic straining. Acta Materialia, 51, 1539-1560.

Raphanel, J.L., Ravichandran, G., Leroy, Y.M., 2004, Three-dimensional rate-dependent crystal plasticity based on Runge-Kutta algorithms for update and consistent linearization. International Journal of Solids and Structures 41, 5995-6021.

Rossiter, J., Brahme, A., Simha, H., Inal, K., Mishra, R. 2010. A new Crystal Plasticity Scheme for Explicit Time Integration Codes to Simulate Deformation in 3D Microstructures: Effects of Strain Path, Strain Rate and Thermal Softening on Localized Deformation in the Aluminum Alloy 5754 During Simple Shear. International Journal of Plasticity, 26(12), 1702-1725.

Rossiter, J., Brahme, A., Inal, K., Mishra, R.K., 2011, Distribution of Stress Triaxiality in FCC Polycrystals Under Equibiaxial Loading. Scripta Materialia, 65 (3), 183-185.

Rossiter, J., Brahme, A., Inal, K., Mishra, R.K., 2013, Numerical analyses of surface roughness during bending of FCC single crystals and polycrystals. International Journal of Plasticity, 46, 82-93.

Sachs, G., 1928. On the derivation of a condition of flowing. Zeitschrift des Vereines Deutscher Ingenieure, 72, 734-736.

Sarkar, J., Kutty, T.R.G., Conlon, K.T., Wilkinson, D.S., Embury, J.D., Lloyd, D.J., 2001, Tensile and bending properties of AA5754 aluminum alloys. Materials Science and Engineering A, 316, 52-59.

Sarkar, J., Kutty, T.R.G., Wilkinson, D.S., Embury, J.D., Lloyd, D.J., 2004, Tensile properties and bendability of T4 treated AA6111 aluminum alloys. Materials Science and Engineering A, 369, 258-266.

Saylor, D., Fridy, J., El-Dasher, B., Jung, K., Rollett, A., 2004, Statistically representative three-dimensional microstructures based on orthogonal observation sections, Metallurgical and Materials Transactions A, 35, 1969-1979.

Schleich, R., Sindel, M., Liewald, M., 2009, Investigation on the effect of curvature on forming limit prediction for aluminum sheet alloys. International Journal of Material Formability, 2, 69-74.

Schmid, E., 1924, Remarks on the vivid deformation of crystals. Zeitschrift fur physic 22, 328-333.

Schouterden, K., Lairson, B.M., 1996, Optimal filtering of scanning probe microscope images for wear analysis of smooth surfaces. Journal of Vacuum Science and Technology B, 14, 3445-3451.

Sfantos, G.K., Aliabadi, M.H., 2006, A boundary cohesive grain element formulation for modelling intergranular microfracture in polycrystalline brittle materials. International Journal for Numerical Methods in Engineering, 69, 1590-1626.

Shkatulyak, N.M., Pravednaya, N.P., 2013, Effect of alternating bending on the texture, structure and mechanical properties of aluminum sheets. Metal Science and Heat Treatment, 54, 472-476.

Siamoto, S., personal communication, February 18, 2011, Queen's University, Kingston, On.

Singh, K.K., Sangal, S., Murty, G.S., 2002, Hall-Petch behaviour of 316L austenitic strainless steel at room temperature. Materials Science and Technology, 18, 165-172.

Story, J.M., Jarvis, G.W., Zonker, H.R., Murtha, S.J., 1993, Issues and trends in automotive aluminum sheet forming. SAE 930277, p1-25.

Taylor, G.I., 1938, Plastic Strain in Metals. Journal of the Institute of Metals 62, 307-324.

Thuillier, S., Le Maoût, N., Manach, P.Y., 2010, Bending limit prediction of an aluminum thin sheet. International Journal of Material Forming, 3, 223-226.

Thuillier, S., Le Maoût, N., Manach, P.Y., 2011, Influence of ductile damage on the bending behaviour of aluminium alloy thin sheets. Materials and Design, 32, 2049-2057.

Turner, T.J., Miller, M.P., 2007. Modeling the Influence of Material Structure on Deformation Induced Surface Roughening in AA7050 Thick Plate. Journal of Engineering Materials and Technology, 129, 367-379.

US Bureau of Transportation Statistics website, http://www.rita.dot.gov/bts/sites/rita.dot.gov.bts/files/publications/national_transportation_statistics/index.html

Watanabe, I., Terada, K., Akiyama, M., 2005. Two-scale analysis for deformation-induced anisotropy of polycrystalline metals. Computation Materials Science 32, 240-250.

Weiss, M., Rolfe, B., Hodgson, P.D., Yang, C., 212, Effect of residual stress on the bending of aluminium. Journal of Materials Processing Technology, 212, 877-883.

Wheeler, M.J., Sheasby, P.G., Kewley, D., 1987, Aluminum structured vehicle technology – A comprehensive approach to vehicle design and manufacturing in aluminum. SAE 870146, p1-11.

Williams, J., 2005. Engineering Tribology. Cambridge University Press.

Wittridge, N.J., Knutsen, R.D., 1999. A microtexture based analysis of the surface roughening behaviour of metallic sheets during stretch forming. Materials Science and Engineering: A , 269, 205-216.

Wolff, N.P., 1978, Interrelation between part and die design for aluminum auto body panels. SAE 780392, p1-6.

Wright, S., Nowell, M., Bingert, J., 2007, A comparison of textures measured using X-ray and electron backscatter diffraction. Metallurgical and Materials Transactions A, 38, 1845-1855.

Wu, P., Neale, K.W., Van Der Giessen, E., Jain, M., Makinde, A., MacEwen, S.T., 1998, Crystal Plasticity Forming Limit Diagram Analysis of Rolled Aluminum Sheets, Metallurgical and

Materials Transactions A, 29, 527-535.

Xu, X.P., Needleman, A., 1993, Void nucleation by inclusion debonding in a crystal matrix. Modelling Simulation Material Science Engineering, 1, 111-132.

Yerra, S.K., Tekoglu, C., Scheyvaerts, F., Delannay, L., Van Houtte, P., Pardoen, T., 2010, Void growth and coalescence in single crystals. International Journal of Solids and Structures 47,1016-1029.

Yue, Z.F., 2005. Surface roughness evolution under constant amplitude fatigue loading using crystal plasticity. Engineering Fracture Mechanics, 72, 749-757.

Zhang, G., Wu, X., Hu, S.J., 2001. A Study on Fundamental Mechanisms of Warp and Recoil in Hemming. Transactions of the ASME, 123, 436-441.

Zhu, G., Xiaohua, H., Kang, J., Mishra, R., Wilkinson, D., 2011. Deformation inhomogeneity in large-grained AA5754 sheets. Materials Science and Engineering A 528, 4187-4198.